amU
Aix Marseille Université

NNT : 2024AIXM0001

THÈSE DE DOCTORAT

Soutenue à AMU — Aix-Marseille Université
le 18 Decembre 2024 par

Sisira SURESH

Impulsive stimulated Raman scattering imaging using ultra-fast acoustic-optic delay lines

Discipline
Physique et Sciences de la Matière

Spécialité
Optique, photonique et traitement d'image

École doctorale
Ecole Doctorale Physique et Sciences de la Matière ED352

Laboratoire/Partenaires de recherche
Institut Fresnel

CRIMSON: Coherent Raman Imaging for the Molecular Study of the Origin of Diseases

CNRS: Centre national de la recherche scientifique

Composition du jury

Manuel JOFFRE Professeur, Ecole Polytechnique Paris	Rapporteur
Arnaud MUSSOT Professeur, Université de Lille	Rapporteur
Nicolas FORGET Directeur de research, Institut de Physique de Nice	Examinateur
Sophie BRASSELET Directrice de recherche, Institut Fresnel	Présidente du jury
Hervé RIGNEAULT Directeur de research, Institut Fresnel	Directeur de thèse
Samuel MÉTAIS Maître de conférences, Institut Fresnel	Co-encadrant de thèse

INSTITUT FRESNEL MARSEILLE

CRIMSON

cnrs

Affidavit

I, undersigned, Sisira Suresh, hereby declare that the work presented in this manuscript is my own work, carried out under the scientific supervision of Dr. Hervé Rigneault in accordance with the principles of honesty, integrity and responsibility inherent to the research mission. The research work and the writing of this manuscript have been carried out in compliance with both the french national charter for Research Integrity and the Aix-Marseille University charter on the fight against plagiarism.

This work has not been submitted previously either in this country or in another country in the same or in a similar version to any other examination body.

Marseille, October 21,2024



This work is licensed under Creative Commons Attribution-NonCommercial-NoDerivatives 4.0 International Public License

List of publications and participation in conferences

List of publications:

1. **Suresh, Sisira**, Ines Martin, Samuel Metais, Chrysa Vourdaki, Sébastien Coudreau, Randy Bartels, Nicolas Forget, and Hervé Rigneault. "Agile acousto-optic delay line for fast impulsive stimulated Raman imaging." Optics Letters 50, no. 2 (2025): 379-382.

2. **Suresh, Sisira**, Ines Martin, Samuel Métais, Siddarth Shivkumar, Nicolas Forget, Randy Bartels, and Herve Rigneault. "Impulsive stimulated Raman scattering imaging using an ultra-fast acoustic-optics delay line." In Advanced Chemical Microscopy for Life Science and Translational Medicine 2024, vol. 12855, pp. 31-36. SPIE, 2024.

3. Metais, Samuel, **Sisira Suresh**, Paulo Diniz, Chrysa Vourdaki, Ines Martin, Siddarth Shivkumar, Randy Bartels, Nicolas Forget, and Hervé Rigneault. "Hyperspectral acquisition with ScanImage at the single pixel level: application to time domain coherent Raman imaging." Optics Express 32, no. 22 (2024): 38849-38863.

4. Shivkumar, Siddarth, Dekel Ranann, Samuel Metais, **Sisira Suresh**, Nicolas Forget, Randy Bartels, Dan Oron, and Hervé Rigneault. "Selective detection in impulsive low-frequency Raman imaging using shaped probe pulses." Physical Review Applied 19, no. 5 (2023): 054075.

Participation in conferences and Summer schools:

1. Summer School SMART-X secondement, Fatlite, Antibe, March 2022

2. Poster presentation on 'Ultrafast Low Frequency Coherent Raman microscopy' at International conference: French-Israel Symposium on Non-Linear and Quantum optics January 2023, Ein-Gedi, Israel

3. Poster presentation on 'Impulsive stimulated Raman Imaging using acousto optic delay lines' at '10ème Conférence Plénière du GDR Ondes' December 2023, Marseille

4. Talk at International conference 'Photonics West' on 'Impulsive stimulated Raman Imaging using acousto optic delay lines' January 2024, San Francisco, USA.

Résumé

Le domaine de l'imagerie a connu des progrès remarquables, grâce aux avancées en matière de manipulation et de détection de la lumière. La microscopie moderne offre une résolution et une spécificité chimique sans précédent, permettant une observation détaillée des spécimens grâce à divers mécanismes de contraste. Ces méthodes, qui comprennent des techniques optiques et non optiques, ont évolué pour permettre l'imagerie de cellules vivantes sans qu'il soit nécessaire de les colorer, alors que la sensibilité chimique reste un facteur clé pour l'identification de la composition d'un échantillon.

Parmi les techniques qui sont apparues pour améliorer la sensibilité chimique, la spectroscopie infrarouge a été une des premières innovations. Toutefois, ses limites - notamment en ce qui concerne l'absorption d'eau - ont conduit à rechercher d'autres méthodes. La découverte de la diffusion Raman, qui est passée d'un simple outil spectroscopique à une technique d'imagerie avancée, a constitué une évolution importante. La diffusion Raman cohérente (CRS) a amélioré les limites de la diffusion Raman spontanée en utilisant des processus d'excitation vibrationnelle plus efficaces. Cependant, la CRS est limitée par son incapacité à détecter les vibrations dans certaines gammes de basses fréquences et par son inefficacité à exciter de multiples modes vibrationnels, ce qui incite à explorer de nouvelles techniques pour surmonter ces défis.

Cette thèse se concentre sur la diffusion Raman stimulée par impulsion (ISRS), une technique pompe-sonde qui surmonte les limitations de la CRS. En utilisant une approche dans le domaine temporel, nous démontrerons comment l'ISRS excite les vibrations moléculaires avec de courtes impulsions de pompe, ce qui permet de recueillir plus d'informations dans le domaine spectral en une seule acquisition. Pour ce faire, on étudie tous les modes excités par la largeur de bande de l'impulsion de pompe, ce qui produit un indice de réfraction transitoire qui peut ensuite être analysé à l'aide d'une impulsion de sonde qui est modulée lorsqu'elle se déplace dans le milieu. Une simple transformée de Fourier de cette modulation permet d'obtenir des spectres à large bande.

En utilisant des dispositifs acousto-optiques, en particulier des filtres dispersifs programmables acousto-optiques (AOPDF) et une ligne à retard agile (ADL) pour la mise en forme de l'impulsion et le contrôle du retard, ce travail permet d'obtenir une imagerie hyperspectrale à une fréquence de 7 Hz, avec un temps d'arrêt des pixels de 25 μs selon la ligne à retard utilisée. Nous démontrerons comment nous avons amélioré la vitesse d'imagerie en passant à un système d'imagerie " Scanimage " construit à la maison. En outre, nous avons amélioré la limite de détection en incorporant une source laser à large bande avec un meilleur contrôle des impulsions et

une meilleure résolution spectrale grâce à des balayages à retardement plus longs. Le dispositif expérimental combine des lasers à large bande, des lignes à retard acousto-optiques et une acquisition rapide des données, optimisant l'ISRS pour les régions Raman à haute et basse fréquence. L'imagerie d'échantillons pharmaceutiques et liquides démontre une vitesse et une résolution améliorées.

Dans cette thèse, nous présenterons également un mode de " détection sélective " des échantillons en contrôlant le délai d'échantillonnage de la sonde. Ceci est rendu possible par l'utilisation de l'ADL, qui offre la flexibilité d'échantillonner à un délai spécifique.

Ces avancées dans le domaine de l'ISRS permettent une imagerie chimique précise et en temps réel, avec des applications dans des domaines tels que les produits pharmaceutiques et la biomédecine. Cette recherche repousse les limites de la spectroscopie Raman et ouvre la voie aux développements futurs de l'imagerie hyperspectrale.

Abstract

The field of imaging has seen remarkable progress, driven by advances in light manipulation and detection. Modern microscopy offers unprecedented resolution and chemical specificity, enabling detailed observation of specimens through various contrast mechanisms. These methods, including both optical and non-optical techniques, have evolved to allow for imaging of live cells without the need for staining, while chemical sensitivity remains a key factor in identifying the composition of a sample.

Among the techniques that have emerged to enhance chemical sensitivity, infrared spectroscopy was an early innovation. However, its limitations—particularly regarding water absorption—prompted the search for alternative methods. A significant development came with the discovery of Raman scattering, which has been adapted from a simple spectroscopic tool to an advanced imaging technique. Coherent Raman Scattering (CRS) improved upon the limitations of spontaneous Raman scattering by employing more efficient vibrational excitation processes. However, CRS is constrained by its inability to detect vibrations in certain low-frequency ranges and its inefficiency in exciting multiple vibrational modes, prompting the exploration of new techniques to overcome these challenges.

This thesis focuses on Impulsive Stimulated Raman Scattering (ISRS), a pump-probe technique that overcomes the limitations of CRS. By using a time-domain approach, we will demonstrate how ISRS excites molecular vibrations with short pump pulses, allowing for more information to be gathered in the spectral domain in a single acquisition. This is achieved by studying all the modes excited by the bandwidth of the pump pulse, resulting in a transient refractive index that can then be analyzed with a probe pulse that gets modulated as it travels through the medium. A simple Fourier transform of this modulation yields broadband spectra.

By employing acousto-optic devices, particularly Acousto-Optic Programmable Dispersive Filters (AOPDF) and an Agile Delay Line (ADL) for pulse shaping and delay control, this work achieves video-rate hyperspectral imaging at a rate of 7 Hz, with a pixel dwell time of 25 μs depending on the delay line used. We will demonstrate how we improved imaging speed by transitioning to a homebuilt 'Scanimage' imaging system. Additionally, we enhanced the detection limit by incorporating a broadband laser source with better pulse control and improved spectral resolution through longer delay scans. The experimental setup combines broadband lasers, acousto-optic delay lines, and fast data acquisition, optimizing ISRS for both high- and low-frequency Raman regions. Imaging pharmaceutical and liquid samples demonstrates improved speed and resolution.

We will also report a mode of 'selective detection' of samples in this thesis by controlling the delay of the probe sampling. This is made possible by using the ADL, which

provides the flexibility to sample at a specific delay.

These advancements in ISRS enable precise, real-time chemical imaging, with applications in fields such as pharmaceuticals and biomedicine. This research pushes the limits of Raman spectroscopy, setting the stage for future developments in hyperspectral imaging.

Résumé étendu en français

Les technologies d'imagerie ont connu des avancées significatives grâce aux améliorations dans la manipulation et la détection de la lumière. La microscopie moderne offre une résolution sans précédent et une spécificité chimique élevée, permettant l'observation détaillée des échantillons à travers divers mécanismes de contraste. Ces méthodes, incluant des techniques optiques et non optiques, ont évolué pour permettre l'imagerie des cellules vivantes sans nécessiter de coloration, tandis que la sensibilité chimique reste un facteur clé pour identifier la composition d'un échantillon.

Lors de l'utilisation des techniques optiques de contraste en microscopie, on peut dire de manière générale que le rayon électromagnétique utilisé pour étudier l'échantillon d'intérêt est soit absorbé, soit diffusé par celui-ci. L'absorption se produit lorsque la fréquence de l'onde électromagnétique incidente correspond à la fréquence de vibration de la molécule, souvent dans les états d'énergie vibrationnelle. Un exemple de cela est l'absorption infrarouge, où la longueur d'onde du faisceau interagissant se situe dans la gamme des microns aux millimètres. En ce qui concerne la diffusion, la longueur d'onde de l'onde électromagnétique interagissant avec la molécule est bien plus grande que la taille de la molécule. Il en résulte une interaction du faisceau incident avec l'ensemble de la molécule, et le processus de diffusion prédomine. Cette diffusion peut être élastique, appelée diffusion de Rayleigh, auquel cas le faisceau est diffusé à la même fréquence. Cependant, une partie peut également être diffusée de manière inélastique, ce qui entraîne une diffusion Raman à une fréquence différente de celle du faisceau incident. Cette onde diffusée peut être soit à une fréquence plus basse, soit à une fréquence plus élevée que l'onde incidente. Lorsqu'elle est diffusée à une fréquence plus élevée, elle est appelée faisceau diffusé anti-Stokes, et le faisceau diffusé à une fréquence plus basse est le faisceau Stokes. La Fig.1 montre les diagrammes des niveaux d'énergie de ces techniques pour comparaison. Il est clair à partir de la figure que le phénomène d'absorption utilise des faisceaux incidents de faible fréquence et de grande longueur d'onde, par rapport au phénomène de diffusion, qui implique des états virtuels à plus haute énergie.

Parmi les techniques qui ont émergé pour améliorer la sensibilité chimique, la spectroscopie infrarouge a été une innovation précoce, mais ses limites, en particulier dans le contexte de l'absorption de l'eau, ont incité à la recherche de méthodes alternatives. Un développement significatif est survenu avec la découverte de la diffusion Raman, qui a été adaptée d'un simple outil spectroscopique à une technique d'imagerie avancée. La spectroscopie Raman présente plusieurs avantages par rapport à la spectroscopie infrarouge, tels qu'une résolution spatiale améliorée grâce à une longueur d'onde plus courte, une faible absorption de l'eau et la disponibilité d'objectifs

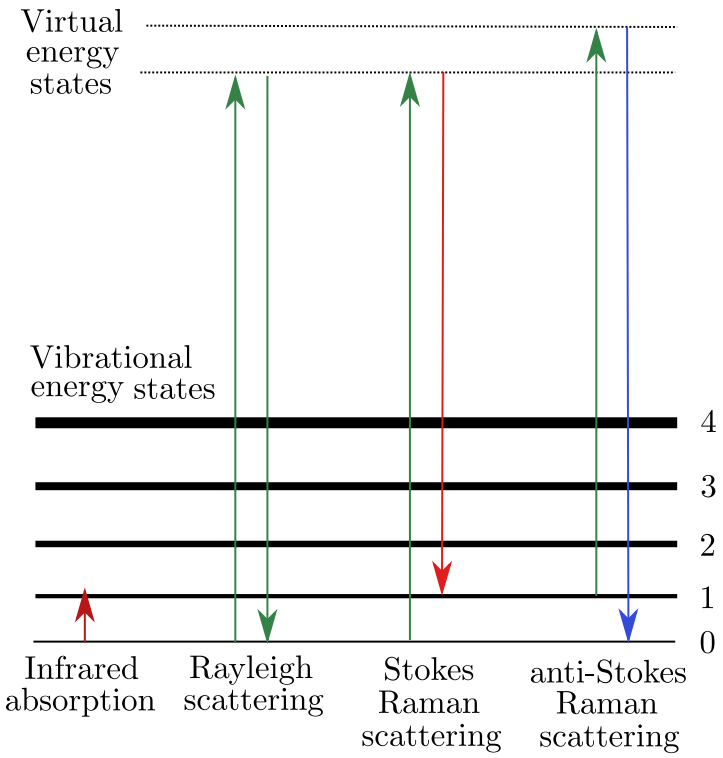

FIGURE 1 : Les diagrammes des niveaux d'énergie des différents mécanismes de diffusion sont présentés. L'absorption infrarouge, où un photon infrarouge excite un électron de l'état fondamental au premier niveau d'excitation vibrationnelle. Dans la diffusion de Rayleigh, le photon incident est diffusé de manière élastique à la même fréquence, tandis que la diffusion Raman implique une diffusion inélastique, avec un photon réémis dont l'énergie est soit plus faible (décalage de Stokes), soit plus élevée (décalage d'Anti-Stokes).

dans cette plage de longueurs d'onde. Cependant, l'effet Raman présente une faible section efficace d'absorption par rapport à l'infrarouge.

La diffusion Raman cohérente (CRS) a amélioré cette limitation de la diffusion Raman spontanée en utilisant des processus d'excitation vibratoire plus efficaces. Cela a été réalisé en introduisant un schéma d'excitation résonante d'une vibration d'intérêt en utilisant un faisceau « pompe » et un faisceau « Stokes », dont les différences de fréquence correspondent à la fréquence vibratoire qui nous intéresse. Il existe deux principales méthodes pour cela : nous pouvons observer le faisceau diffusé anti-Stokes à haute énergie, appelé diffusion Raman anti-Stokes cohérente (CARS), ou la diffusion Raman stimulée (SRS), où l'on peut soit observer la perte du faisceau de pompe (SRL), soit le gain en intensité du faisceau de Stokes (SRG). Les diagrammes des niveaux d'énergie de ces techniques sont présentés (Fig.2).

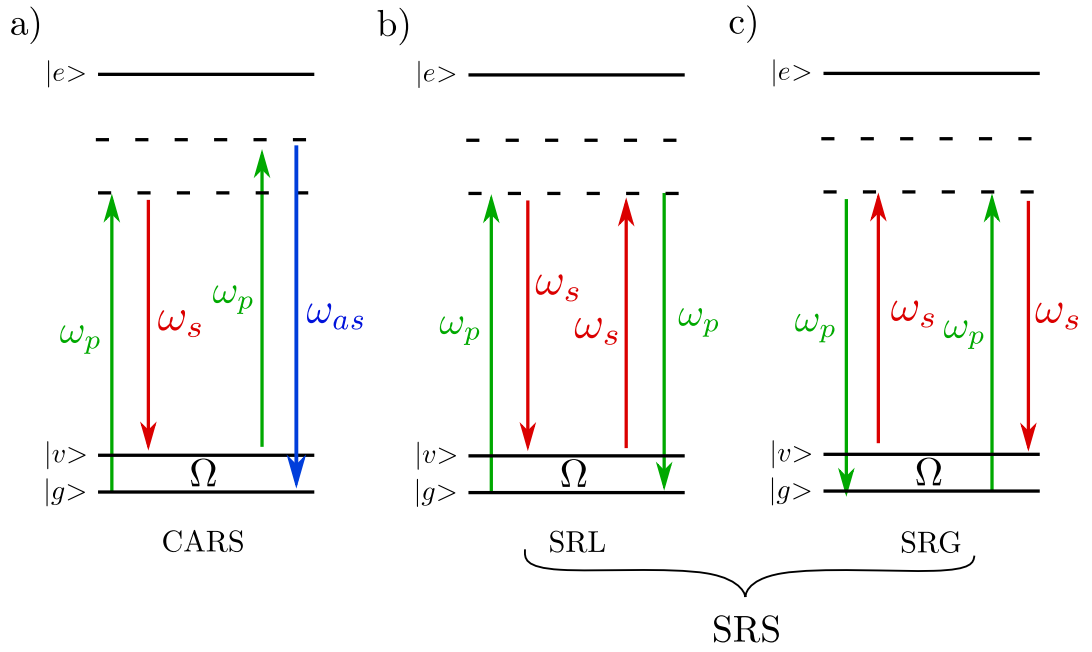

FIGURE 2 : a) montre le diagramme des niveaux d'énergie de la CARS, où deux pompes et un Stokes interagissent dans un phénomène de mélange à quatre ondes pour émettre un faisceau 'anti-Stokes' à haute énergie. b) et c) montrent le phénomène de SRS sous les formes SRL et SRG, respectivement.

Depuis sa découverte, la diffusion Raman cohérente (CRS) a été largement utilisée pour l'imagerie d'une variété d'échantillons, y compris les lipides, les protéines, les structures de l'ADN et de l'ARN, ainsi que dans la pharmacologie pour détecter la distribution des médicaments dans les tissus. Ces échantillons présentent généralement des fréquences vibratoires supérieures à 200 cm^{-1}. La CRS est principalement appliquée dans la région d'empreinte (500–1800 cm^{-1}), qui contient des signatures vibratoires caractéristiques de nombreuses liaisons moléculaires. Cependant, pour

obtenir des informations structurales globales sur une molécule, il est nécessaire d'étudier les vibrations à des fréquences beaucoup plus basses, inférieures à 200 cm^{-1}. La Fig.3 présente un spectre typique de la molécule de carbamazépine et de son dimère, illustrant le défi de mesurer efficacement les spectres dans la plage de fréquences vibratoires inférieures à 200 cm^{-1}.

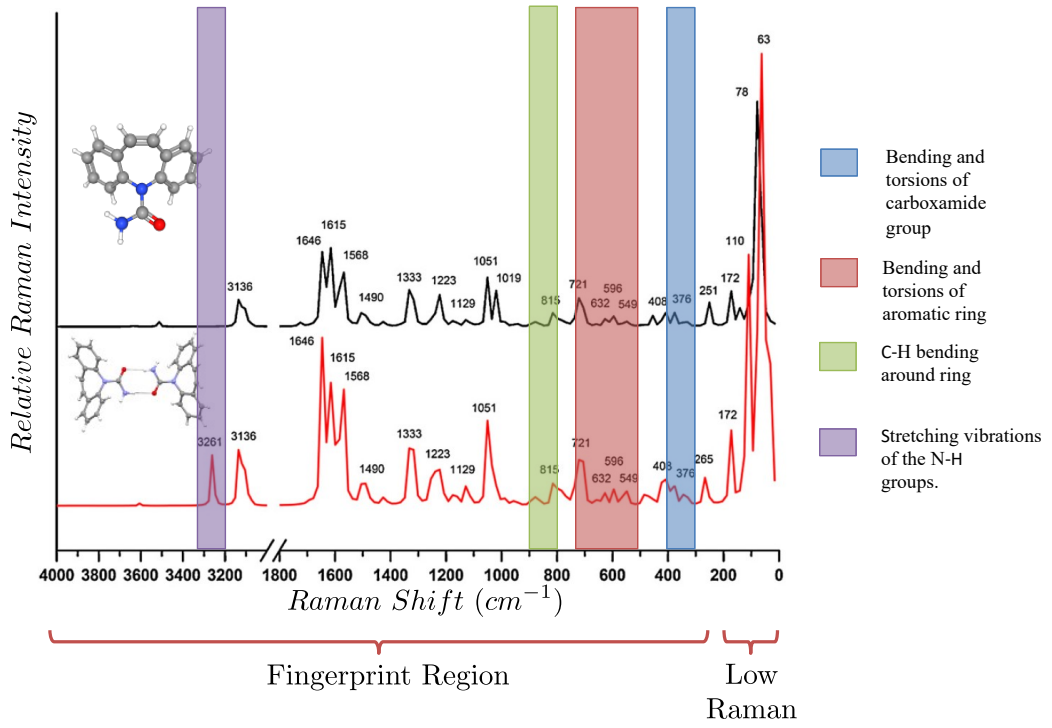

FIGURE 3 : La figure illustre les spectres de la carbamazépine (en rouge) et de son dimère (en noir) obtenus par diffusion Raman anti-Stokes cohérente (CARS). Les régions ombrées mettent en évidence quels pics correspondent à des types spécifiques de vibrations moléculaires. Il est évident que les pics dans la région de basse fréquence Raman sont moins bien définis, illustrant le défi de capturer des informations spectrales claires dans cette plage.

C'est parce que la CRS est contrainte par son incapacité à détecter des vibrations dans certaines plages de basse fréquence. Traditionnellement, ces méthodes utilisent des filtres optiques pour isoler le faisceau d'intérêt. Dans le cas de la CARS, on isolera la fréquence diffusée anti-Stokes, et pour la SRS, dans le cas du SRL, nous isolons la pompe, ou pour le SRG, nous isolons le Stokes. Lorsque la fréquence d'intérêt est basse, la pompe et le Stokes ont une différence de fréquence qui est également très faible, ce qui entraîne une interférence à travers les filtres. Cela est illustré dans la Fig.4. Pour cette raison, nous sommes amenés à explorer de nouvelles techniques pour surmonter ces défis.

Le cœur de cette recherche porte sur la diffusion Raman stimulée impulsionelle

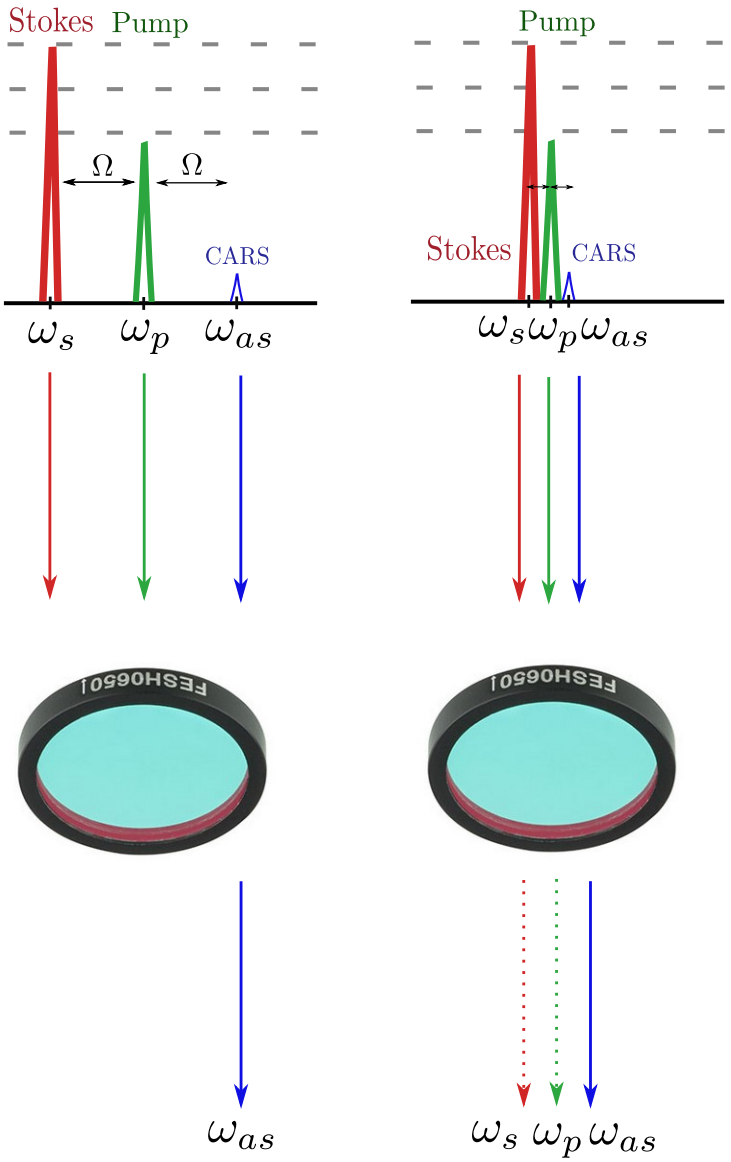

FIGURE 4 : La figure montre deux cas de la spectroscopie CARS où les faisceaux de pompe, de Stokes et d'anti-Stokes générés sont présentés à la fois pour les hauts et les bas nombres d'ondes, à gauche et à droite respectivement. Nous isolons le signal d'intérêt—dans ce cas, la longueur d'onde de l'anti-Stokes diffusé—à l'aide d'un filtre passe-bas à 650 nm. Dans le cas des hautes fréquences, les fréquences de Stokes (ω_s), de pompe (ω_p) et d'anti-Stokes (ω_{as}) sont suffisamment éloignées pour qu'un filtre puisse isoler le signal requis, l'anti-Stokes. Cependant, lorsque nous passons aux basses fréquences, nous constatons que les trois faisceaux deviennent beaucoup plus proches en fréquence, ce qui entraîne le passage de certains faisceaux de pompe et de Stokes à travers le filtre.

(ISRS), une technique pompe-sonde développée pour surmonter les limites des méthodes antérieures. L'ISRS permet d'exciter des vibrations moléculaires à l'aide d'un laser pompe dont l'impulsion est de coute durée, tandis qu'un faisceau sonde dans le temps la variation d'indice transitoire resultant de l'excitation de la pomp. Cette thèse décrit la mise en œuvre de l'ISRS pour l'imagerie en temps réel, offrant une voie vers l'imagerie hyperspectrale, même dans les régions difficiles des basses fréquences Raman. La Fig.5 illustre l'essence de la technique, où une impulsion courte dans le temps, large en fréquence, excite tous les modes dans la largeur de bande de l'impulsion. Cela crée une variation transitoire de l'indice de réfraction qui dure quelques picosecondes et qui est sondé dans le temps par une impulsion sonde.

Le faisceau sonde subit une large gamme de changements dans ses propriétés, tels que la diffraction, le profil spatial, la polarisation, l'accumulation de décalage de phase, et le décalage spectral que nous utilisons dans cette these. Le décalage spectral résulte de l'interférence entre les bandes latérales et le faisceau sonde, entraînant un décalage de l'intensité du faisceau soit vers le bleu, soit vers le rouge, en fonction de si celui-ci rencontre un indice de réfraction en baisse ou en hausse. Ainsi, en plaçant un filtre passe haut au centre du spectre du faisceau sonde, on peut conv'ertir la variation de l'indice de réfraction en une variation d'intensité. La transformation de Fourier de cette variation de l'indice de refraction donne le spectre vibrationnel. Une représentation est montrée dans la Fig.6.

L'implémentation expérimentale de l'ISRS, ciblant à la fois les régions Raman haute et basse, démontre comment l'intégration de lasers à large bande, de lignes de retard avancées et de systèmes d'acquisition de données rapides améliore les capacités de la technique. Nous verrons comment l'ISRS, bien qu'initialement développé en se concentrant sur la détection des vibrations à basse fréquence, peut être utilisé pour l'imagerie CRS à large bande. Le contrôle précis des impulsions laser, en particulier en ce qui concerne la forme des impulsions et le retard, est identifié comme un facteur critique pour le succès de l'ISRS dans cette gamme. Cette étude utilise des dispositifs acousto-optiques, tels que des filtres dispersifs programmables acousto-optiques et des déflecteurs acousto-optiques, pour optimiser le contrôle des impulsions pour une imagerie efficace à la vitesse vidéo. L'application de systèmes avancés de mise en forme et de retard des impulsions, y compris des déflecteurs acousto-optiques et des filtres dispersifs programmables, permet la détection efficace des vibrations moléculaires sur une large gamme spectrale.

Pour créer des images hyperspectrales, nous utilisons des délais ultrarapides générés par des dispositifs acousto-optiques, combinés à des miroirs de balayage galvanométriques et à des systèmes d'acquisition de données rapides, afin de rassembler précisément des informations sur un champ de vue (FOV) plus large. Cette approche nous permet de capturer des traces temporelles pour chaque pixel, ce qui donne lieu à un cube de données hyperspectrales. En appliquant une transformation de Fourier à la trace temporelle de chaque pixel, nous pouvons extraire des informations détaillées sur la présence d'échantillons spécifiques à cet emplacement. Ce processus est illustré dans la Fig. 7. Cette méthode permet une imagerie en temps réel avec des temps de séjour des pixels aussi courts que 25 à 30 μs, selon le type de filtre dispersif

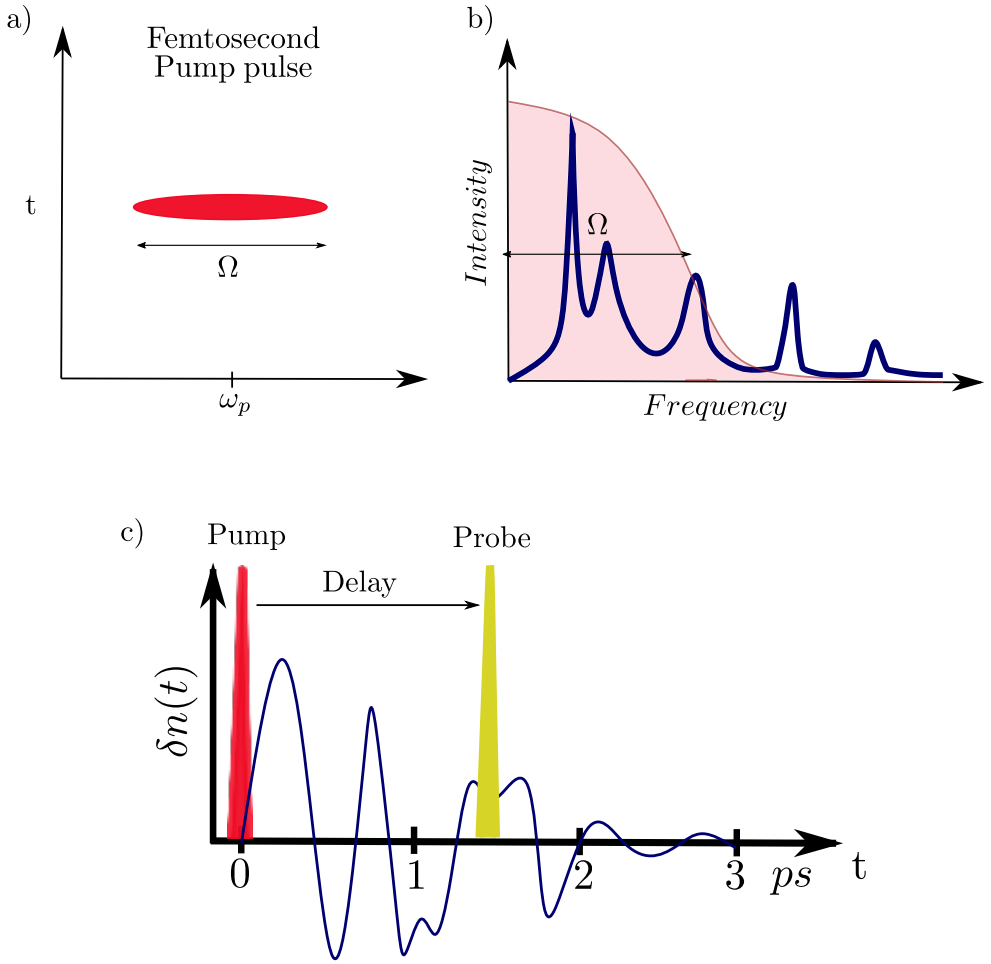

FIGURE 5 : a) montre le diagramme fréquence/temps d'une impulsion pompe femtoseconde, montrant une impulsion courte dans le temps et large en fréquence ; b) montre le spectre réel de la molécule d'intérêt et la largeur de bande d'excitation de l'impulsion femtoseconde, représentée en rouge. Le faisceau pompe ne peut exciter que les modes qui se trouvent dans cette largeur de bande ; c) montre l'indice de réfraction transitoire généré par excitation impulsionnelle à l'aide de la pompe, et le faisceau sonde est retardé dans le temps pour sonder ce phénomène.

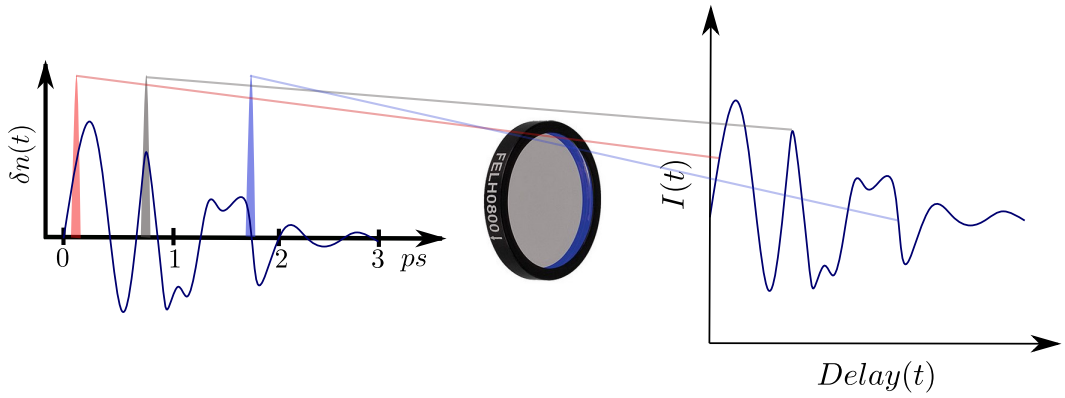

FIGURE 6 : La figure montre la variation transitoire de l'indice de réfraction $\delta(n)$ et le faisceau sonde à divers instants. Lorsqu'il rencontre un indice de réfraction croissant ou décroissant, il est décalé vers le rouge ou le bleu, et lorsqu'il atteint un pic ou un creux, le spectre n'est pas dècalè. Placer un filtre passe bas (800 LP pour une sonde de 800 nm) permet de traduire cette variation transitoire de l'indice de réfraction en une variation d'intensité.

programmable acousto-optique (AOPDF) utilisé.

Ces développements dans le contrôle des impulsions, pour l'imagerie hyperspectrale sont démontrés dans cette these à travers l'imagerie d'échantillons pharmaceutiques et en phase liquide, montrant des améliorations significatives tant dans la vitesse d'imagerie que dans la résolution spectrale atteignable. La thèse discutera également de la manière dont l'utilisation d'une "ligne de retard agile" conçue avec un déflecteur acousto-optique permet une détection sélective avec des informations disponibles sur la trace temporelle d'échantillons d'intérêt. De plus, des améliorations supplémentaires au système ISRS étendent sa largeur de bande de détection, permettant l'observation des vibrations moléculaires jusqu'à 550 cm^{-1}, une amélioration substantielle par rapport aux capacités précédentes d'imagerie. La recherche souligne l'importance de l'utilisation de lasers à large bande et de techniques sophistiquées de mise en forme des impulsions pour repousser les limites de ce qui peut être détecté.

En conclusion, cette recherche démontre la faisabilité de l'imagerie hyperspectrale à cadence vidéo utilisant l'ISRS, améliorant significativement la largeur de bande de détection, la résolution et la vitesse d'imagerie. L'intégration soignée de mécanismes avancés de contrôle des impulsions et de lasers à large bande a permis de capturer des informations chimiques détaillées sur une large gamme spectrale, ouvrant la voie à des applications plus larges dans le domaine de l'imagerie.

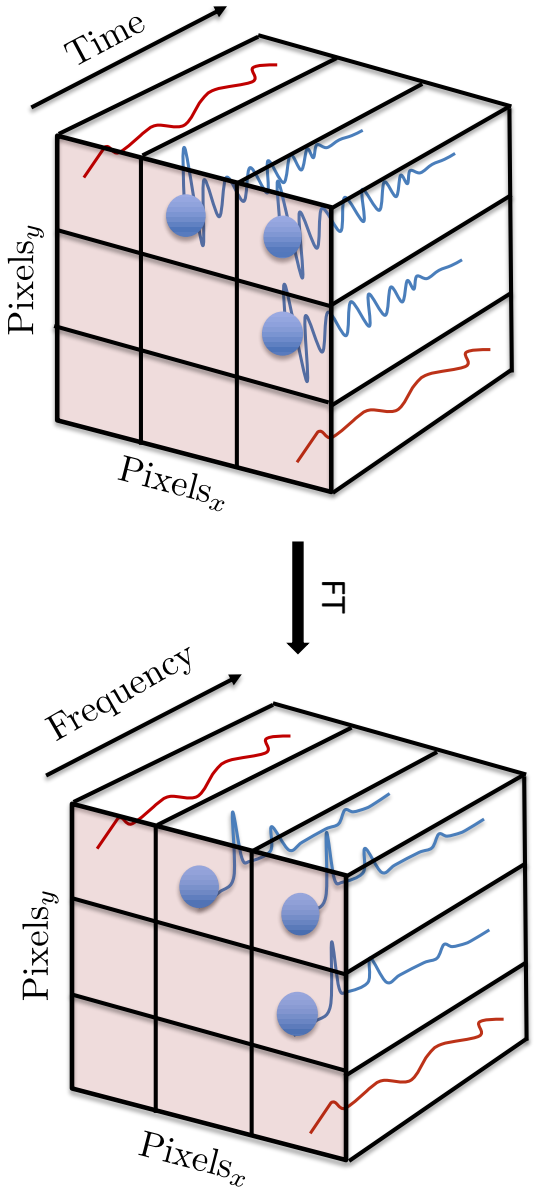

FIGURE 7 : La figure montre une représentation des données hyperspectrales récupérées pour une image de 3 × 3 pixels. Le miroir de balayage galvanométrique reste sur un pixel particulier jusqu'à ce que l'acquisition des données temporelles soit complétée pour ce pixel spécifique (typiquement 25 μs). Seule la présence d'un composé Raman-actif dans le pixel donne lieu à la creation d'une variation de l'indic optique transitoire. La transformation de Fourier de ce signal transitoire produit un spectre, permettant une imagerie hyperspectrale pour chaque pixel.

Table of Contents

Affidavit 2

List of publications and participation in conferences 3

Résumé 5

Abstract 7

Résumé étendu en français 9

Table of Contents 18

List of Figures 21

List of Tables 23

Introduction 24

1 Theory of CRS and simulation of ISRS 26
- 1.1 Outline of the chapter . . . 26
- 1.2 Theory of Raman scattering : A classical approach . . . 27
  - 1.2.1 Spontaneous Raman . . . 27
  - 1.2.2 Coherent Raman . . . 29
- 1.3 Coherent Raman scattering in microscopy . . . 32
- 1.4 Towards Impulsive stimulated Raman scattering . . . 34
- 1.5 Logic of simulating spectral shift . . . 38
  - 1.5.1 Driving term and the creation of the transient refractive index . . . 38
  - 1.5.2 Spectral Shift on the Probe Beam . . . 39
  - 1.5.3 Interference with the sidebands in frequency domain . . . 41
- 1.6 Results from simulation . . . 41
- 1.7 Conclusion . . . 46

2 Acousto optics for imaging 47
- 2.1 Introduction . . . 47
- 2.2 Acousto-Optic Programmable Dispersive Filters : The Dazzler . . . 48
  - 2.2.1 Inside the AOPDF . . . 48
  - 2.2.2 Pulse shaping with the AOPDF . . . 50
  - 2.2.3 Delay with AOPDF . . . 51
  - 2.2.4 Comparison of HR and WB Dazzlers . . . 52

2.2.5 Conclusion of the various parameters of the HR and WB dazzler 55
2.3 Acousto optic deflector as a delay line . . . 55
2.3.1 Architecture and principle . . . 56
2.3.2 Theory of ADL . . . 57
2.3.3 Comparison of features with dazzler . . . 60
2.4 Conclusion . . . 60

3 Implementation of ISRS for Low Raman 62
3.1 Outline of the chapter . . . 63
3.2 Experimental setup . . . 63
3.2.1 Laser source . . . 64
3.2.2 Pump arm . . . 64
3.2.3 Probe arm . . . 64
3.2.4 Recombination and imaging unit . . . 64
3.2.5 Detection unit and aquisition . . . 65
3.3 Data acquisition with ScanImage using Dazzler as fast delay line . . . 65
3.3.1 Hyperspectral imaging with Scanimage at single pixel level . . . 66
3.3.2 Data Acquisition and synchronization of electronics . . . 67
3.3.3 Data processing . . . 69
3.3.4 Experimental results . . . 69
3.3.5 Limitations and conclusion of ISRS implementation with the Dazzler . . . 75
3.4 ISRS with Agile Delay Line(ADL) as fast delay line . . . 75
3.4.1 Characterization . . . 76
3.4.2 Synchronisation of driver and acquisition with Scanimage . . . 78
3.4.3 ADL for ISRS . . . 78
3.4.4 Conclusion on ADL for ISRS . . . 83

4 Extending the detection range through ISRS 84
4.1 Outline of the Chapter . . . 84
4.2 Experimental Setup . . . 85
4.2.1 Laser source . . . 85
4.2.2 Pump Arm . . . 85
4.2.3 Probe Arm . . . 85
4.2.4 Recombination and imaging Unit . . . 85
4.2.5 Detection Unit and acquisition . . . 87
4.3 Characterization of the pulses . . . 87
4.3.1 Splitting into the pump and probe . . . 87
4.3.2 Pulse Shaping the pump . . . 87
4.3.3 Pulse Shaping the probe . . . 90
4.3.4 Summary of the important parameters of the pump and probe . 90
4.4 Imaging using the extended detection range . . . 94
4.4.1 Calibration crystals imaging . . . 94
4.4.2 Pharmaceutical compounds . . . 96

4.4.3 Solvents 96
4.5 Conclusion 99

5 Conclusions and Future perspectives **101**
5.1 Conclusion 101
5.2 Possible improvements 102
5.2.1 Excitation range 102
5.2.2 Detection range 104
5.2.3 Sensitivity and SNR 106
5.3 Future perspectives 107

Bibliographie **109**

List of Figures

1 Diagramme des niveaux d'énergie des différents mécanismes de diffusion 10
2 Diagramme des niveaux d'énergie de la CARS et de la SRS 11
3 Spectres typiques d'une molécule de carbamazépine 12
4 Fuite du filtre pour les basses fréquences Raman 13
5 Logique de l'ISRS 15
6 Détection de l'ISRS 16
7 Imagerie hyperspectrale 17

1.1 Classical view of a diatomic molecule 27
1.2 Energy level diagrams of the different scattering phenomena 29
1.3 Energy level diagrams for the different coherent scattering phenomena 32
1.4 Comparison of scattered frequencies between low and high vibrational resonances. 34
1.5 Schematic of the impulsive excitation and detection 35
1.6 Schematic of the spectral shift effect 37
1.7 Excitation bandwidth for different pump pulse durations (τ_p) 39
1.8 Logic of the numerical model 40
1.9 Simulation of interference of sidebands for probe pulse duration 3 ps . 43
1.10 Simulation of interference of sidebands for probe pulse duration 300 fs 44
1.11 Simulation of interference of sidebands for probe pulse duration 300 fs 45

2.1 Working principle of the AOPDF 50
2.2 Delay with the AOPDF 54
2.3 Schematic of the ADL 56
2.4 Schematic of the delay line for calculating group delay 58

3.1 Schematic of the experimental setup for ISRS 63
3.2 Schematic of the scanning process over a field of view containing a smiley face. 67
3.3 Electronic layout of the experiment 68
3.4 Raw data obtained from ScanImage for the transmission channel . . . 70
3.5 Raw data obtained from ScanImage for the Raman channel 71
3.6 Plots of the three channels acquired with the DAQ 71
3.7 Hyperspectral imaging with calibration crystal 72
3.8 Imaging of acetaminophen and anthracene 74
3.9 Measured ADL delay with RF frequency 76
3.10 Pulse duration measured at the output of the ADL and at the sample plane 77
3.11 Beam profile before and after the ADL 77

3.12 ISRS signal from BGO with the ADL 79
3.13 Effect of chirping of probe beam 80
3.14 Selective detection of Antharcene and Acetaminophen with the ADL . 81
3.15 Fourier retrieved Raman spectra of a mixture of anthracene and acetaminophen, showing results when the ADL samples different numbers of points. 82

4.1 Schematic of the experimental setup for ISRS. 86
4.2 Spectra of pump and probe with the preset of laser used 88
4.3 Cutting of spectra by FSPC with prism displacement 89
4.4 Dazzler windows for different conditions of input pulse width and dispersion compensation 91
4.5 Comparison of spectra at sample plane 92
4.6 Autocorrelator measurement of pulse width 93
4.7 Images with calibration crystal : BGO and KTP 95
4.8 Images with anthracene and acetaminophen 97
4.9 Spectra of different solvents 98
4.10 Hyperspectral images of chloroform 100

5.1 Summary of improvements in ISRS technique 103
5.2 Scaling factor of the Dazzler 105
5.3 Time trace and Raman spectra of BGO with the 'double-dazzler' setup 106
5.4 4-ML CdSe nanoplatelet structure 107
5.5 Images taken of CdSe nanoplatelets with a thiol ligand with a 5-carbon chain 108

List of Tables

2.1 Comparison of properties between WB and HR Dazzlers 52

4.1 Comparison of pump and probe properties 93

Introduction

Ever since Anton van Leeuwenhoek developed the first microscopes in the 1600s, significant advancements have been made in the field of imaging. These improvements stem from a better understanding and manipulation of light, leading to enhanced control over imaging processes. Compared to those early images, modern microscopy offers vastly superior resolution, sensitivity, and chemical specificity. Indeed, the manner in which we image a specimen can be fundamentally altered by changing the illumination type, detection method, or the microscope itself.

At its core, the process of creating an image relies on the generation of contrast. This contrast can be achieved through various means. Leeuwenhoek's initial microscope enhanced magnification to observe light transmission. In general, contrast mechanisms in microscopy can be categorized into optical and non-optical techniques. Non-optical techniques involve the use of dyes and stains, which greatly enhance image specificity and quality, though they require labeling of samples. Optical techniques, such as phase contrast and differential interference contrast microscopy, allow for the observation of live, unstained cells in tissue culture.

What has been lacking in our discussion so far is chemical sensitivity in imaging, which is crucial for identifying the nature of the sample. The chemical composition of a substance is often a defining characteristic, making it an ideal form of contrast. The very first chemical sensitivity technique was infrared (IR) spectroscopy. Since the discovery of infrared radiation by Sir William Herschel in the 1800s, this technique has been extensively developed for clinical and biomedical analyses. Its applications range from the clinical analysis of biofluids [1], diagnostic applications in breast cancer [2-4], to noninvasive in vivo monitoring of blood, tissue, and muscle as explained in the review article [5]. However, infrared spectroscopy has limitations in sample preparation, and the strong absorption of water at the excitation wavelength poses additional challenges.

In 1928, a significant breakthrough occurred with the discovery of inelastic scattering of light by Raman, a form of contrast specific to the vibrational motion of molecules. This groundbreaking discovery earned Raman the Nobel Prize in Physics in 1930. Initially recognized as a spectroscopic technique, Raman scattering was quickly adapted for imaging in a span of just 60 years. However, because the spontaneous Raman process was very inefficient, coherent Raman scattering (CRS) was employed. This technique involves using a pump and a Stokes beam to excite the vibration of interest by tuning their wavelength difference to match the vibrational mode of the molecule.

However, two issues are associated with this technique : it efficiently detects only a single vibrational frequency, and it cannot detect vibrations lower than 200 cm^{-1}.

To address these limitations, a broadband coherent anti-Stokes Raman scattering (CARS) approach was needed. When it comes to detecting low vibrational frequencies, Brillouin scattering has proven to be effective for phonon vibrations below 10 cm^{-1}. Spontaneous Raman scattering is sensitive to low-frequency Raman vibrations ($> 10\ cm^{-1}$) but is ultimately too slow for imaging applications. Although recent advancements have enabled hyperspectral imaging in the fingerprint region using coherent Raman techniques, the ultimate solution involved transitioning to a time-domain approach. This led to the development of impulsive stimulated Raman scattering (ISRS), a pump-probe technique.

This thesis is dedicated to the implementation of ISRS in video-rate imaging. The chapters are organized to provide a comprehensive introduction to Raman imaging. Chapter 1 begins with the theory of Raman scattering, presenting the classical model of a molecule as a harmonic oscillator. The discussion then transitions to the ISRS technique, with a focus on the spectral shift technique for detection mechanism. Important parameters for effective ISRS are examined through simulations of pump excitation and probe detection. Additionally, the significance of precise pulse control is discussed.

The second chapter will focus on pulse control for enabling video-rate imaging through ISRS. Three different acousto-optic devices were employed for this purpose. Two of these are Acousto-Optic Programmable Dispersive Filter (AOPDF) delay lines, known as the 'Wide-band' (WB) and 'High resolution' (HR) Dazzlers. These devices facilitate pulse shaping and the introduction of delay between the pump and probe. Additionally, an Agile delay line (ADL) based on an acousto optic deflector, capable of randomly selecting delays within its range, will be introduced.

The third chapter will focus on the experimental implementation of ISRS in the low Raman region. This will involve using the WB Dazzler and the ADL for video-rate imaging of pharmaceutical samples. The data acquisition technique for hyperspectral imaging will also be explained in detail, utilizing ScanImage, a MATLAB based software.

The fourth and final chapter will focus on extending the detection range of the setup. This involves a modified setup with a higher bandwidth laser, additional pulse shaping mechanisms, and the use of the HR Dazzler. The chapter will describe how pulse control becomes more challenging with higher bandwidth and how these challenges are addressed. It will also showcase some of the images captured with this enhanced setup.

The conclusion will highlight the improvements made in speed, resolution, and detection bandwidth of a low Raman setup. This thesis demonstrates that hyperspectral imaging at videorate would be feasible even in the fingerprint region, given a large enough bandwidth and proper pulse control.

1 Theory of CRS and simulation of ISRS

Summary

1.1 Outline of the chapter . . . 26
1.2 Theory of Raman scattering : A classical approach . . . 27
1.2.1 Spontaneous Raman . . . 27
1.2.2 Coherent Raman . . . 29
1.3 Coherent Raman scattering in microscopy . . . 32
1.4 Towards Impulsive stimulated Raman scattering . . . 34
1.5 Logic of simulating spectral shift . . . 38
1.5.1 Driving term and the creation of the transient refractive index . . . 38
1.5.2 Spectral Shift on the Probe Beam . . . 39
1.5.3 Interference with the sidebands in frequency domain . . . 41
1.6 Results from simulation . . . 41
1.7 Conclusion . . . 46

1.1 Outline of the chapter

This chapter provides an introduction to the field of Raman scattering microscopy. It begins with a classical approach to Raman scattering, including the derivation of polarization components for both spontaneous and stimulated Raman effects. Following this, the chapter discusses the latest advancements in chemically sensitive imaging using both spontaneous and Coherent Raman Scattering (CRS) techniques. The limitations of CRS, particularly in the context of broadband spectroscopy and imaging, as well as its diminished sensitivity at lower wavenumbers, are also examined. This sets the stage for introducing the main focus of this thesis : the technique of Impulsive Stimulated Raman Scattering (ISRS). While the chapter does not delve deeply into the theoretical aspects of ISRS, it provides a concise explanation of the various detection mechanisms associated with the technique, with particular emphasis on the spectral shift method for retrieving the spectrum. To clarify the working principles, simulations are employed to demonstrate the detection of molecular vibrations. These simulations begin with picosecond pulses for CRS techniques and gradually transition to time-domain methods by reducing the pulse width of the pump and probe lasers into the femtoseconds, highlighting the shift from frequency to time-domain analysis.

1.2 Theory of Raman scattering : A classical approach

The Raman effect is the inelastic scattering of light by a molecule, wherein the molecule absorbs some energy from the incoming beam, resulting in a shift in the frequency of the scattered light. However, only a very small fraction of the incident light (approximately 1 in 10^7) is scattered at a different frequency. This scattering is chemically specific because each molecule has a unique vibrational signature retrieved directly from the scattered light spectrum. Due to the weak scattering coefficient, several techniques have been developed to enhance the efficiency of Raman scattering. The following section explains the theory behind Raman scattering. We follow the classical approach of considering the molecule as a harmonic oscillator with a fundamental frequency of vibration Ω. We will focus on deriving the polarisation components of the scattered radiation for both the spontaneous and stimulated Raman scattering phenomena.

1.2.1 Spontaneous Raman

We begin with the classical description of matter and field through the spontaneous Raman effect, as detailed in the work of Potma et al. [6]. To grasp this concept, it is essential to first introduce linear and nonlinear optical processes. These processes stem from the interaction between the electric field component of light and the charged particles within a molecule. The electric fields used to excite the sample are in the visible and infrared range ($\sim 10^3 THz$). At these frequencies, only electrons—being lighter than nuclei—are compelled to oscillate. The frequencies of the nuclear vibrations being much lower ($1-100THz$), cannot be driven adiabatically. As a result, optical resonances within this frequency range primarily arise from the motion of electrons in the material. For simplicity, we consider a diatomic molecule modeled as a spring oscillator, as depicted in the schematic Fig. 1.1.

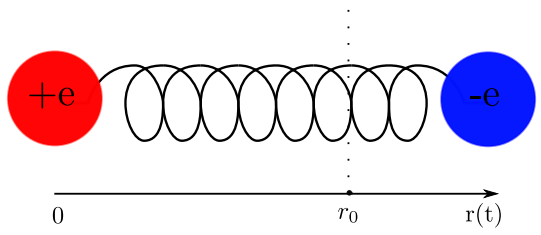

FIGURE 1.1 : Classical representation of a diatomic molecule with one nucleus with partial charge '+e' and the other with partial charge '-e' which is displaced relative to its rest position at r_0 by $r(t)$

This electron displacement from their equilibrium positions induces a dipole mo-

ment.

$$\mu(t) = -e.r(t) \tag{1.1}$$

where e is the charge of the electron and $r(t)$ is the displacement of the electron. Close to the nuclei, the electron binding potential is approximated as a harmonic potential. This is the case of having a weak field interacting with the molecule.
The macroscopic polarization is obtained by adding up all the individual dipole moments N, in a unit volume

$$P(t) = N\mu(t) \tag{1.2}$$

For a weak field, one could also assume that the displacement is directly proportional to the electric field. This makes the polarization

$$P(t) = \epsilon_0 \chi E(t) \tag{1.3}$$

where ϵ_0 is the electric permitivity in vaccum, and χ is the susceptibility of the material. This is the origin of all linear optical phenomena. It is called linear because the polarization varies linearly with the applied electric field.

In the presence of a strong radiation field, the electron is displaced further from its equilibrium position, and the electron binding potential exhibits anharmonic effects. This implies that the relationship between the driving field and the induced polarization is no longer strictly linear. When the anharmonic contributions are small, the polarization can be expressed as a power series of the field to account for the nonlinear electron motions.

$$P(t) = \epsilon_0 [\chi_1 E(t) + \chi_2 E(t)^2 + \chi_3 E(t)^3 + ...] = P^1(t) + P^2(t) + P^3(t) + ... \tag{1.4}$$

where χ^n is the nth order susceptibility, and P^n is the nth order contribution to the polarization.

In most of the coherent or spontaneous Raman processes the electronic polarizability is also perturbed by the nuclear modes. To describe the effect of nuclear motions, we need to connect the electric dipole moment to the polarizability $\alpha(t)$ under the assumption that the driving frequency is far from the electronic resonance of the system

$$\mu(t) = \alpha(t) E(t) \tag{1.5}$$

In the absence of nuclear modes, the polarizability can be approximated as a constant α_0. However, in its presence, the electronic polarizability can be written in terms of its nuclear coordinate to be expanded in a Taylor series as

$$\alpha(t) = \alpha_0 + \left(\frac{\delta\alpha}{\delta R}\right)_0 R(t) + ... \tag{1.6}$$

We can assume the nuclear motion along R to be that of a classical harmonic oscillator

$$R(t) = 2\,R_0\,cos(\Omega t + \phi) = R_0\,[e^{i\Omega t + i\phi} + e^{-i\Omega t - i\phi}] \tag{1.7}$$

where R_0 is the amplitude of the nuclear motion, Ω is the nuclear resonance frequency, ϕ is the phase of the vibration.
The incoming radiation can be written as

$$E(t) = Ae^{-i\omega_1 t} + c.c \tag{1.8}$$

giving us the dipole moment from Equation 1.5

$$\mu(t) = \alpha_0 Ae^{-i\omega_1 t} + A\left(\frac{\delta\alpha}{\delta R}\right)_0 R_0\{e^{i\Omega t + i\phi} + e^{-i\Omega t - i\phi}\}e^{-i\omega_1 t} + c.c \tag{1.9}$$

Equation 1.9 demonstrates that the dipole moment oscillates at several frequencies. The first term represents Rayleigh scattering, where light is scattered elastically at the same frequency as the incident radiation. The majority of incident radiation undergoes this process. The second and third terms correspond to the inelastically scattered Raman-shifted frequencies at $\omega_1 - \Omega$ and $\omega_1 + \Omega$, which are the Stokes and anti-Stokes contributions, respectively. Only a small fraction of light is scattered in this manner. Fig. 1.2 illustrates the different contributions : the ground state is denoted by $|g\rangle$, the first excited state by $|v\rangle$, dotted lines represent the virtual states, and $|e\rangle$ indicates the electronic levels.

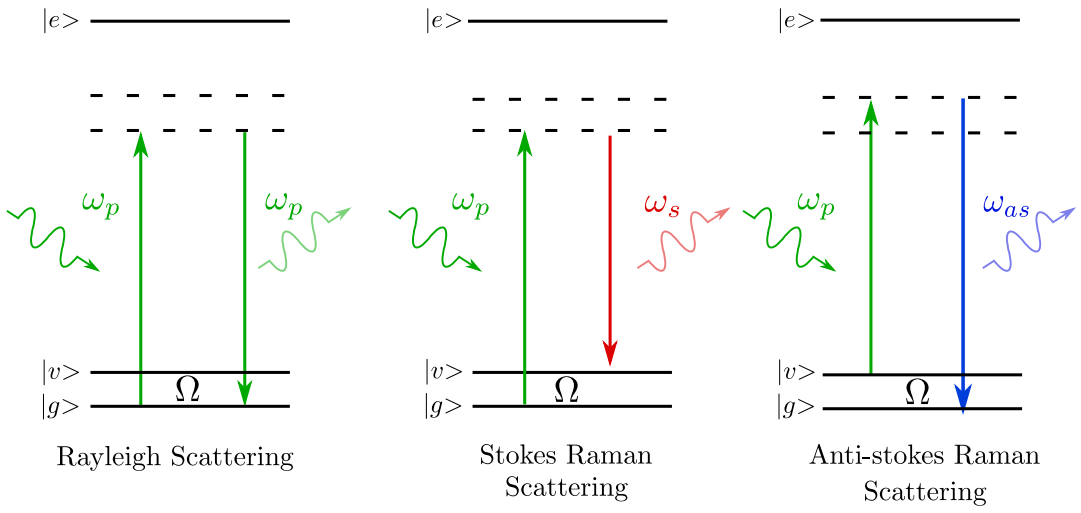

FIGURE 1.2 : Energy level diagrams for the different scattering phenomena : Rayleigh scattering, Stokes Raman scattering, Anti-stokes Raman scattering respectively

1.2.2 Coherent Raman

Now, we consider coherent Raman scattering as an actively driven nuclear oscillator with a resonance frequency Ω, driven along its internuclear axis R. In this scenario,

two light waves are incident on the oscillator, modeled as plane waves :

$$E_i(t) = A_i e^{-i\omega_i t} + \text{c.c.} \tag{1.10}$$

for $i = \{1,2\}$. Here, ω_1 and ω_2 represent the frequencies of the incident waves, with the assumption that both are higher than the resonance frequency, and $\omega_1 > \omega_2$. In this context, $E_1(t)$ is referred to as the pump, while $E_2(t)$ is known as the Stokes wave. When these fields are sufficiently intense, a range of nonlinear interactions can occur at the combination frequency $\omega_\nu = \omega_1 - \omega_2$.

The interaction of these fields with the molecular electronic cloud induces a force $F(t)$ on the nuclear mode at the difference frequency ω_ν. The nuclear displacement $R(t)$ then follows the motion of a driven oscillator, governed by the equation :

$$\frac{d^2R(t)}{dt^2} + 2\gamma\frac{dR(t)}{dt} + \Omega^2 R(t) = \frac{F(t)}{m} \tag{1.11}$$

where γ is the damping constant, and m is the reduced mass of the nuclear oscillator. The general solution to this equation can be expressed as :

$$R(t) = R(\omega_\nu)e^{-i\omega_\nu t} + \text{c.c.} \tag{1.12}$$

Substituting this solution back into the equation gives the expression for the amplitude of oscillation at the resonance frequency ω_ν :

$$R(\Omega) = \frac{1}{m}\left(\frac{\delta\alpha}{\delta R}\right)_0 \frac{A_1 A_2^*}{\Omega^2 - \omega_\nu^2 - 2i\omega_\nu\gamma} \tag{1.13}$$

This equation reveals that the magnitude of the nuclear oscillation depends on the amplitude of the incident light beams and the coupling coefficient between the nuclear coordinate and the electronic polarizability. The vibration amplitude is significantly enhanced when the difference between the frequencies ω_1 and ω_2 matches the fundamental vibrational frequency of the molecule Ω, a condition known as resonance. Under this condition, the combined optical field exerts a force on the vibrational oscillator given by :

$$F(t) = \left(\frac{\delta\alpha}{\delta R}\right)_0 A_1 A_2^* e^{-i\omega_\nu t} + \text{c.c.} \tag{1.14}$$

This equation shows that the electronic motions are coupled to the nuclear motion through the factor $\left(\frac{\delta\alpha}{\delta R}\right)_0$.

Next, the impact of this driven nuclear motion on the optical properties is considered, particularly its role in generating sidebands. Using equations 1.2, 1.5, and 1.6, the polarization can be expressed as :

$$P(t) = N\left[\alpha_0 + \left(\frac{\delta\alpha}{\delta R}\right)_0 R(t)\right]\{E_1(t) + E_2(t)\} \tag{1.15}$$

The terms proportional to α_0 correspond to the linear polarization of the material,

whereas the terms proportional to $\left(\frac{\delta\alpha}{\delta R}\right)_0$ describe the contribution to the third-order polarization due to the driven Raman mode. This nonlinear polarization can be expanded into different frequency combinations as :

$$P_{NL}(t) = P(\omega_{cs})e^{-i\omega_{cs}t} + P(\omega_2)e^{-i\omega_2 t} + P(\omega_1)e^{-i\omega_1 t} + P(\omega_{as})e^{-i\omega_{as}t} + \text{c.c.} \tag{1.16}$$

where $\omega_{cs} = 2\omega_2 - \omega_1$ is the coherent Stokes frequency and $\omega_{as} = 2\omega_1 - \omega_2$ is the anti-Stokes frequency. This nonlinear polarization contains contributions that oscillate at fundamental frequencies ω_1 and ω_2 as well as contributions at new frequencies ω_{cs} and ω_{as}.

The amplitude of polarization for the different frequency components is given by :

$$P(\omega_{as}) = 6\epsilon_0\chi^*_{NL}(\Omega)A_1^2A_2^* \tag{1.17}$$

$$P(\omega_{cs}) = 6\epsilon_0\chi^*_{NL}(\Omega)A_2^2A_1^* \tag{1.18}$$

$$P(\omega_1) = 6\epsilon_0\chi^*_{NL}(\Omega)|A_2|^2A_1^* \tag{1.19}$$

$$P(\omega_2) = 6\epsilon_0\chi^*_{NL}(\Omega)|A_1|^2A_2 \tag{1.20}$$

where the nonlinear susceptibility is defined as :

$$\chi_{NL}(\Omega) = \frac{N}{6m\epsilon_0}\left(\frac{\delta\alpha}{\delta R}\right)_0^2 \frac{1}{\Omega^2 - \omega_v^2 - 2i\omega_v\gamma} \tag{1.21}$$

The nonlinear susceptibility is a material-specific quantity that describes the frequency-dependent response of the material to the incoming radiation. As evident from the equation, the material is more responsive when the frequency difference coincides with the resonance frequency of vibration.

These nonlinear polarizations describe the four lowest-order coherent Raman effects illustrated in Figure 1.3. They are :

- Coherent anti-Stokes Raman scattering (CARS)
- Coherent Stokes Raman scattering (CSRS)
- Stimulated Raman loss (SRL)
- Stimulated Raman gain (SRG)

Among these processes, Coherent Stokes Raman Scattering (CSRS) is less commonly utilized because its emission falls within the infrared (IR) region, where detectors are often less effective due to higher noise levels. In contrast, CARS and SRS are widely employed in clinical imaging, owing to their stringent phase-matching conditions, which ensure that the generated signals are coherent and propagate in well-defined,

predictable directions [7]. The following section provides a comprehensive overview of the current advancements in imaging using both spontaneous Raman scattering and CRS techniques.

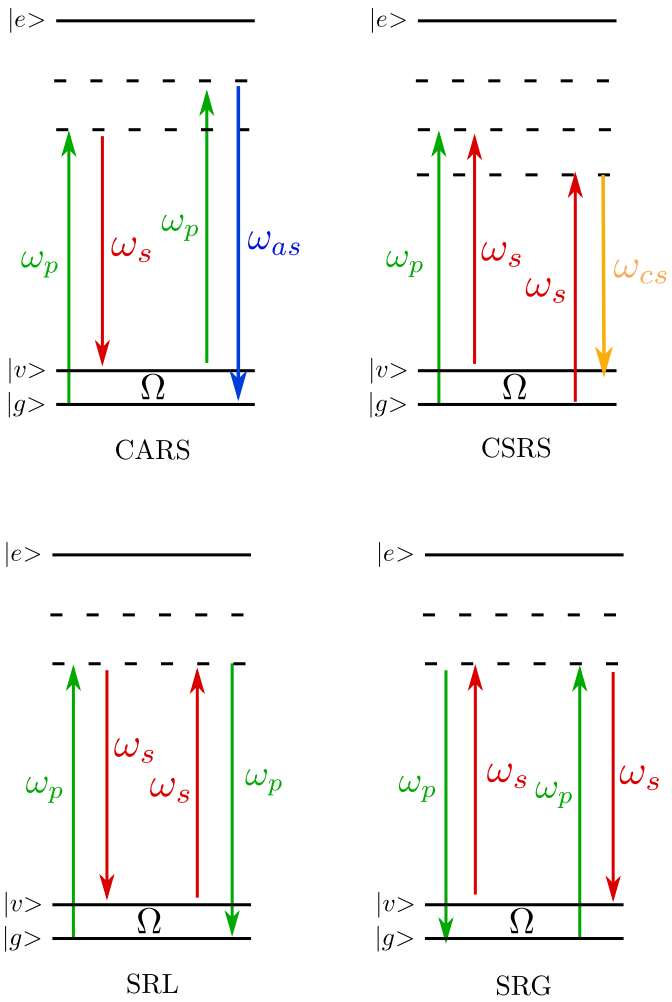

FIGURE 1.3 : Energy level diagrams for the different coherent scattering phenomena. They are Coherent Antistokes Raman (CARS), Coherent Stokes Raman (CSRS), Stimulated Raman Loss (SRL), and Stimulated Raman Gain (SRG) respectively.

1.3 Coherent Raman scattering in microscopy

Having described the theory of Raman scattering, we now move on to its application in imaging. Although spontaneous Raman scattering is a well-established phenomenon, it has a very weak scattering coefficient, making it impractical for imaging. This weakness stems from the difficulty in separating the inelastically scattered spontaneous Raman signal from the broad baseline resulting from sample fluorescence. The weak

signal also poses challenges in obtaining spectra from diluted samples in solution. Even with long integration times, acquiring a spectrum can take several minutes, making it less than ideal for live imaging purposes. However, several methods can enhance spontaneous Raman scattering for imaging applications, typically by combining it with other imaging techniques to improve speed. For example, light sheet microscopy has been used to image live fish [8], and heart tissue was imaged with a split scanning apparatus [9] using spontaneous Raman.

However, many of the limitations mentioned above are addressed by coherent Raman scattering (CRS) techniques. As discussed earlier, CRS employs two light pulses whose frequency difference matches the vibrational frequency of interest. The most widely used CRS techniques are Coherent Anti-Stokes Raman Scattering (CARS) and Stimulated Raman Scattering (SRS). The stimulated Raman effect was initially discovered accidentally in organic liquids using the emission from a ruby laser in 1962 by Eckhardt [10]. CARS was subsequently discovered in 1965 by Maker and Terhune, who reported the four-wave mixing process that could be resonantly tuned to the vibrational frequencies of molecules [11]. Since its discovery, CARS has been extensively used in imaging due to its ability to produce video-rate images [12-14]. In addition to providing high-speed imaging, CARS offers 3D sectioning capability, high penetration depth with near-infrared excitation, and reduced photobleaching and damage [14]. The technique has seen significant advancements over the years, thanks to recent developments in lasers, detectors, and electronics.

However, all the aforementioned CRS methods were limited to providing video-rate imaging for a single frequency, unlike spontaneous Raman scattering, which, despite its slower speed, can yield a full vibrational spectrum. Recently, there has been growing interest in addressing this limitation with broadband CARS techniques. A review paper highlights various approaches to achieve this [15]. These techniques can be broadly categorized as follows :

- **Hyperspectral CARS :** This method involves exciting a single vibrational frequency at a time while tuning one of the beams, typically the Stokes beam, to scan across a spectrum [16-18].
- **Multiplex CARS :** This technique utilizes a narrowband pump and a broadband stokes to capture the CARS spectrum [19-21].
- **Single beam CARS :** The technique employs a single ultrashort pulse to generate vibrational coherence [22, 23].
- **Time-domain techniques :** These methods include time-resolved CARS, where a delayed probe beam measures the vibrational resonance induced by the pump and Stokes beams [24, 25].

Similarly, SRS could also be used as a basis for these broadband techniques. While all these techniques, particularly the frequency domain methods, perform well in the higher frequency region, they each have their own limitations when it comes to low frequency detection.

1.4 Towards Impulsive stimulated Raman scattering

With the advent of CRS, imaging samples with molecular vibrations above 200 cm^{-1} has become possible. However, a significant challenge arises when imaging slower vibrations. This concept is illustrated in the schematic Fig.1.4.

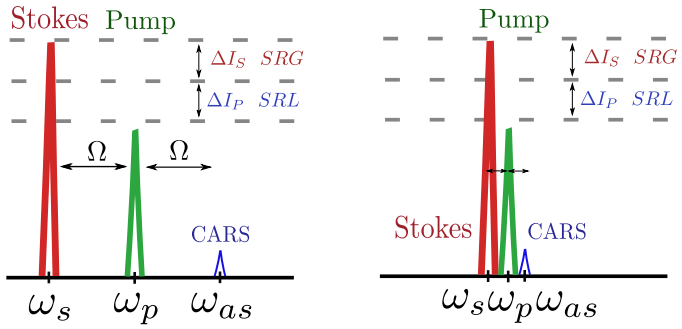

FIGURE 1.4 : The schematic of scattered CARS field, with Pump and stokes frequency for high frequency and low frequency vibrational resonance respectively

To excite low-frequency vibrations, the pump and Stokes beams need to be very close in frequency. This proximity can cause bleed-through issues with the filters used to remove the pump in CARS and SRS setups, where optical filters are employed to eliminate the pump in CARS and either the pump or Stokes beams in SRL or SRG, respectively. This filtering step is crucial because a lock-in amplifier is typically used to detect the signal generated from the modulated pump, and it is essential to completely extinguish the pump signal before it reaches the photodiode. This is a common problem for all frequency domain techniques. Recently low frequency Raman studies have been done on rotational transitions, although only through spectroscopy and not imaging [26]. Thus, the most practical solution was to move to time domain techniques.

Time domain techniques, in addition to being more practical for low-frequency Raman detection, offer several other advantages. They effectively remove the non-resonant background radiation, which has long been a problem in frequency domain CARS, by introducing a third probe beam to monitor the vibrational coherence that persists on the picosecond scale [27]. Initially, picosecond narrowband pulses were used for this technique. However, these pulses had the disadvantage that the time-delayed probe pulse interacted with vibrational coherence, which decays over time, thus reducing the useful CARS signal.

With technological advancements in lasers and the introduction of shorter pulses, a technique called Impulsive Stimulated Raman Scattering (ISRS) was developed. ISRS was first developed by Nelson et al. in the 1980s [28]. This technique is similar to a pump-probe approach, where a broadband femtosecond pulse acts as both the pump

and Stokes beams, simultaneously exciting all the vibrational frequencies within its bandwidth. ISRS was initially demonstrated in the Brillouin range and referred to as Impulsive Stimulated Brillouin Scattering (ISBS). In this context, picosecond pulses were used to study acoustic vibrational modes in liquids and solids [29, 30]. The temporal duration of picosecond pulses was sufficient to impulsively excite these low phonon frequencies of less than 10 GHz. However, the Raman vibrations of interest lie in the range of thousands of GHz, necessitating the use of femtosecond pulses.

In the femtosecond regime, for instance, at 170 fs, a pulse at the Fourier transform limit exhibits a bandwidth of approximately 10 nm. When such a short pulse interacts with a molecule, impulsive excitation occurs, where all vibrational modes within the bandwidth of the pump pulse are excited simultaneously. The vibrational coherences start at the same time and in the same phase [31]. This imprints a macroscopic polarization into the bulk sample resulting in a transient refractive index change that persists for a few picoseconds. To detect this transient refractive index, a delayed probe pulse is introduced to observe its effect. This is shown in Fig. 1.5. The probe undergoes a change in its spatial profile, spectrum, and polarisation or gets diffracted.

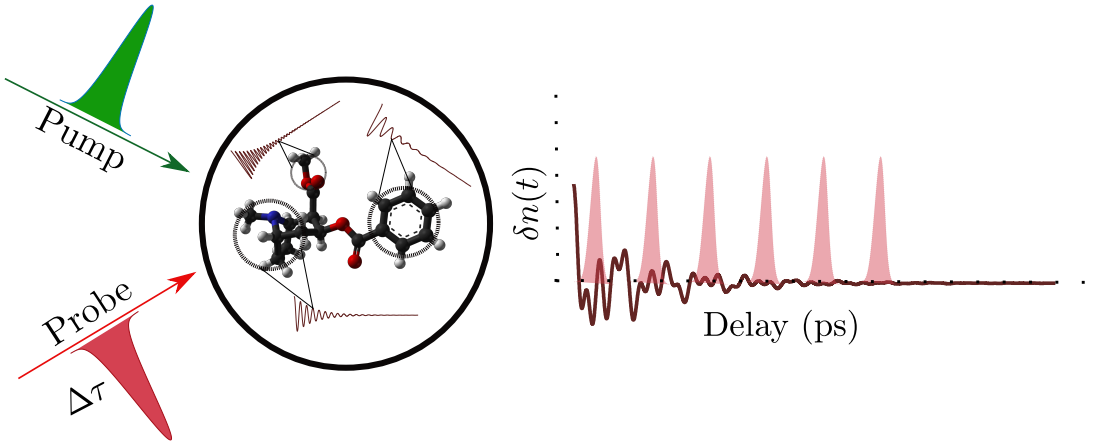

FIGURE 1.5 : Schematic of the impulsive excitation. The pump (green) excites all the modes in the sample that lie within its bandwidth. This results in a transient refractive. The probe beam (red) is sent at different delays $\Delta\tau$ effectively probing it at different points in time.

A variety of methods have been developed for implementing ISRS in both spectroscopy and microscopy, particularly in terms of introducing the delayed probe. Historically, the technique was more suited to spectroscopy rather than imaging, primarily because, in the early days, the delay between the pump and probe was introduced using a mechanical delay line with stepper motors, which significantly slowed down data acquisition [32]. Michelson interferometers were also employed to create time-delayed replicas of pulses [33], where images of polystyrene beads in 2-propanol were captured, although the imaging process was slow, taking 10 minutes

to image a 1500 cm^{-1} bandwidth. The speed of this technique, utilizing the Michelson interferometer, was later improved by employing a rapid scan retroreflective optical path length scanner [34] and further accelerated with high-frequency galvo mirrors [35]. Dual-comb CARS (Coherent Anti-Stokes Raman Scattering) was introduced to enhance the speed of spectrum retrieval, where two ultrashort pulses were used to generate frequency combs at slightly different frequencies [36-38]. Most of these methods were applied for point-by-point detection, with the Raman spectrum being recorded for each pixel and scanning through the sample's region of interest by translating the sample or using slow beam scanning [34, 38, 39]. This was later expedited by introducing rapid beam scanning and wide-field detection using fast galvo mirrors and a camera for detection [40].

The next step is to examine how the probe pulse changes its properties as it traverses the transient refractive index. Several effects can occur on the probe beam, as outlined below :

- **Diffraction :** The earliest implementation of ISRS relied on observing the diffraction of the probe beam from coherent scattering resulting from the standing wave created by impulsive excitation [41-43].
- **Spatial profile :** Also known as Kerr lensing, this involves monitoring changes in the spatial profile of the probe beam when a pump beam imprints its distribution onto the vibrational amplitude of the molecules. The induced refractive index difference acts like a lens, focusing or defocusing the beam. By placing an iris at the Fourier plane, the variation in intensity can be measured [44].
- **Polarization :** The vibrational excitation can be detected through the depolarization of the probe beam [45, 46].
- **Accumulation of phase shift :** The phase shift accumulated by a time-delayed probe pulse is measured interferometrically by mixing it with a time-delayed reference pulse and analyzing the result with a spectrometer [47, 48].
- **Spectral Shift :** As the probe beam passes through the region of the transient refractive index, it experiences a spectral shift. This shift can be converted into an intensity variation using an appropriate filter, allowing for monitoring of the refractive index changes. The frequency shift in the probe beam resembles the generation of anti-Stokes and Stokes frequencies for blue- and red-shifted components, respectively [49-51].

In this work, the spectral shift technique was primarily used to implement ISRS. The schematic in Fig. 1.6 illustrates the working principle for impulsive excitation and detection via spectral shift. This schematic assumes that the probe pulse is much shorter than all the molecular vibrational frequencies.

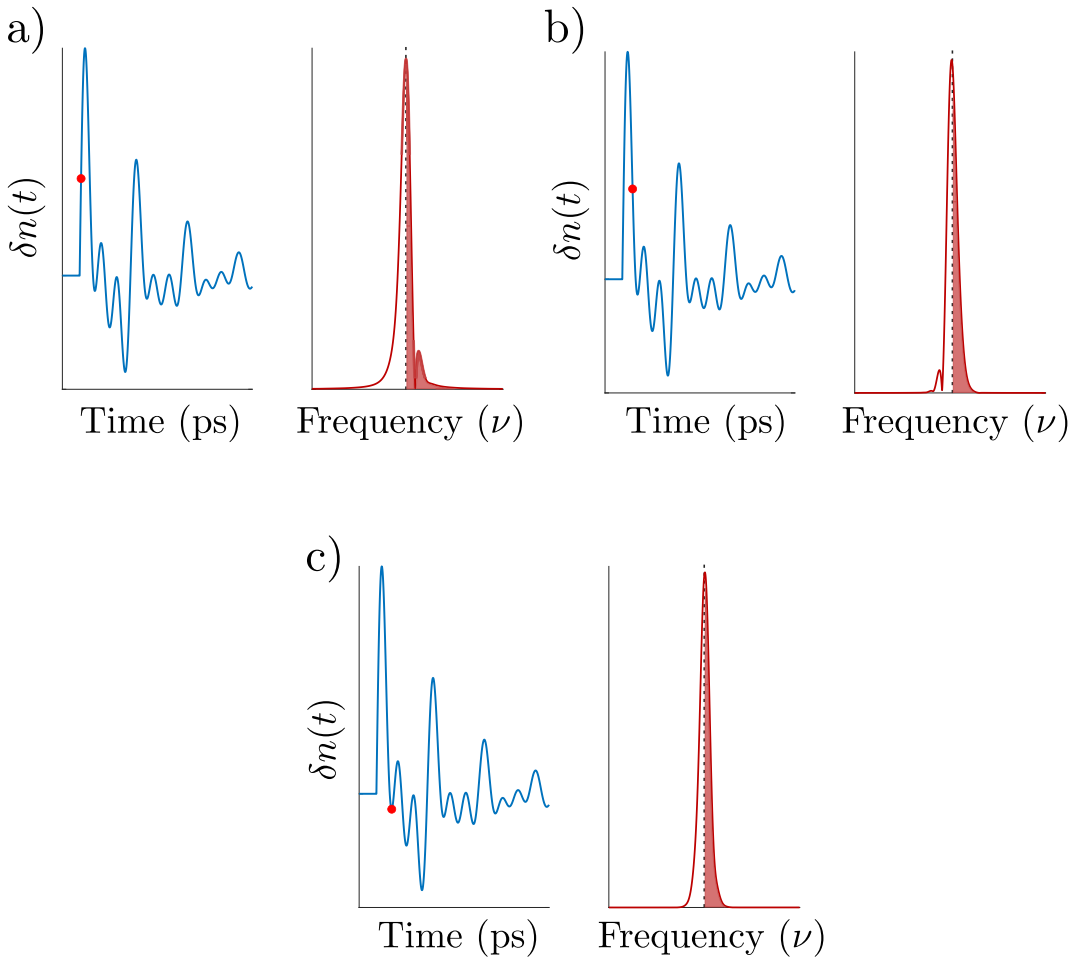

FIGURE 1.6 : Schematic of the spectral shift effect. The red dot indicates the probe beam's position, while the blue curve shows the transient refractive index change, and the red curve represents the probe pulse spectrum. The dotted lines mark a longpass filter, allowing only the unshaded portion of the probe spectrum to pass. (a) The probe encounters a rising refractive index, leading to a redshift and higher intensity through the filter. (b) The probe encounters a falling refractive index, causing a blueshift and lower intensity. (c) A constant refractive index results in no spectral shift of the probe.

When the probe encounters an increasing refractive index, it experiences a red shift due to interference with the Stokes-shifted radiation. Conversely, when it encounters a decreasing refractive index, it undergoes a blue shift due to interaction with the anti-Stokes-shifted beam. At the plateau, where there is no change in refractive index, the probe does not interfere with any sideband. By placing a long-pass filter at the center of the probe beam, the spectral shift can be converted into an intensity

modulation that follows the transient refractive index. The Fourier transform of this modulation yields the Raman spectrum. This time-domain technique, in comparison to frequency-domain methods, has the advantage of being inherently free from non-resonant background radiation, a common issue encountered in (CARS) imaging. This is because we remove the overlap of the pump and probe beam which has the non-resonant background, and are only interested in the modulation that follows after.

The following section will explore the logic behind the spectral shift simulation, modeling the impulsive excitation of the modes in a sample and examining how the probe pulse interacts with the generated sidebands depending on its pulse duration.

1.5 Logic of simulating spectral shift

To simulate the effect of spectral shift and observe how the probe pulse experiences the spectral shift, the theory of low-frequency Raman scattering, as described by Randy Bartels [52], is utilized. This paper models the refractive index variation as an impulsive response.

1.5.1 Driving term and the creation of the transient refractive index

The pump pulse, responsible for inducing the refractive index change, is modeled as a Gaussian pulse with a Fourier Transform Limit (FTL) pulse width τ_p. The electric field of the pulse is given by :

$$E(t) = E_0 e^{-\left(\frac{t}{\tau_p}\right)^2} \tag{1.22}$$

where E_0 is the peak electric field amplitude and τ_p is the pulse duration. We use the definition of the pulse duration τ_p as mentioned in [52] which is related to the RMS and FWHM definitions as $\tau_{\text{FWHM}} \approx 1.665\tau_{\text{RMS}} = 1.177\tau_p$. The excitation strength at a particular mode is defined by :

$$D(\omega) = \frac{1}{T_n} \int_{-\infty}^{\infty} |E(t)|^2 \, e^{-i\omega t} \, dt \tag{1.23}$$

where T_n is the mean pulse duration, calculated as :

$$T_n = \int |E(t)|^2 \, dt \tag{1.24}$$

Evaluating the integral yields the driving term for each frequency ω :

$$D(\omega) = e^{-\frac{1}{2}\left(\frac{\tau_p \omega}{2}\right)^2} \tag{1.25}$$

This expression indicates the bandwidth of excitation achievable for a given pump pulse width. Fig.1.7 illustrates how varying the pump pulse width alters the excitation bandwidth.

The impulsive excitation results in the creation of a transient refractive index due to the modes it can excite. The vibrating modes of interest, f_{signal}, are simulated with a certain width, denoted by γ. The transient refractive index, which follows the product of the driving term and the vibrational modes can be expressed as :

$$\delta n(t) = CD(\omega) \cdot \sin\left(2\pi f_{\text{signal}} t\right) e^{-\gamma t} \tag{1.26}$$

where C is a material specific prefactor that accounts for the material's response and $\omega = 2\pi f_{signal}$.

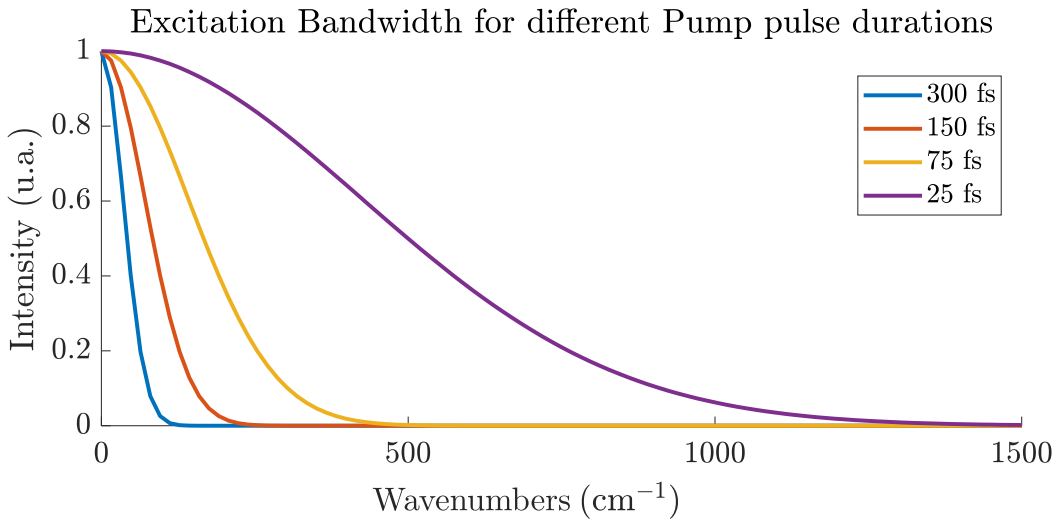

FIGURE 1.7 : Excitation bandwidth for different pump pulse durations (τ_p)

1.5.2 Spectral Shift on the Probe Beam

The next step involves modeling the probe beam as it passes through the perturbed medium. For simplicity, it is assumed that the beam is chirp-free. The probe pulse width τ_{probe} is related to the R.M.S. width σ by :

$$\sigma_{pr} = \frac{\tau_{probe}}{2\sqrt{2\ln 2}} \tag{1.27}$$

The electric field of the Gaussian probe pulse is then described by :

$$E(t) = \frac{1}{\sqrt{2\pi}\sigma_{pr}} e^{-\frac{t^2}{2\sigma_{pr}^2}} \tag{1.28}$$

As the probe traverses the excited sample, it encounters the varying refractive index, which imparts an additional phase depending on the time of arrival. Under the hypothesis of no loss and perfect transmission, the phase factor Φ can be expressed as :

$$e^{\Phi(t)} = e^{i\delta n(t)L} \tag{1.29}$$

where the transient refractive index $\delta n(t)$ is defined in Eq.1.26 and L is the thickness of the sample. Note the positive sign in the exponential that comes from the negative time convention. To determine the spectral shift on the probe, the probe beam amplitude for each delay τ, $E(t,\tau)$ is multiplied by the additional phase for each probed delay, $\Phi(t)$. We move to the frequency domain to define a long-pass edge filter through a function $G(\omega)$. Once the filter is accounted for, an inverse Fourier transform brings us back to the time domain modulated field of the probe $E_{mod}(t)$. The normalized probe pulse frequency shift is then retrieved by computing the differential signal $S(\tau)$. This is summarised in the logic of the model in Fig. 1.8.

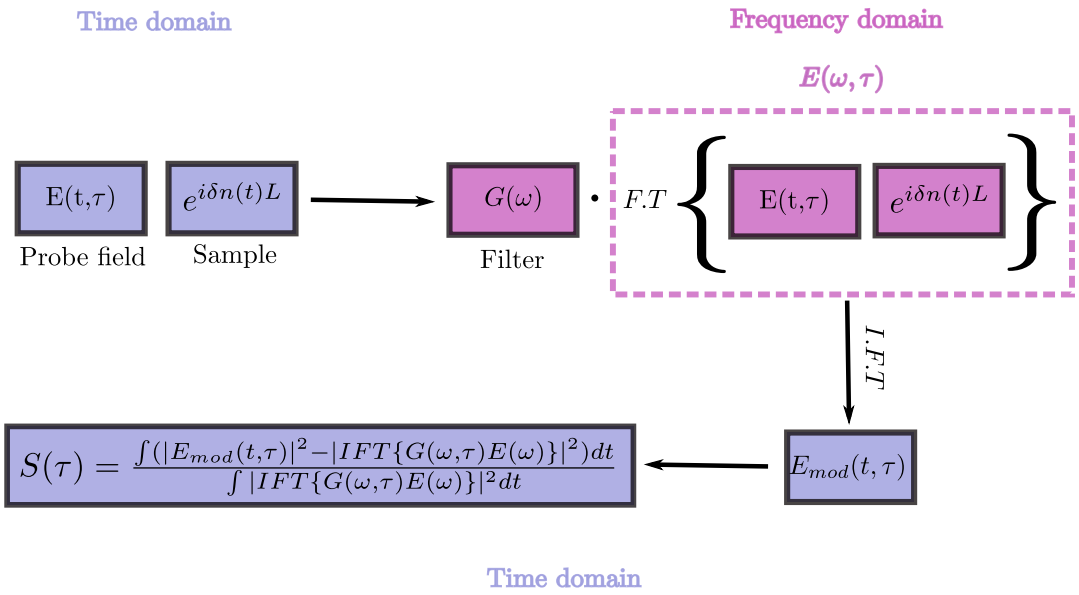

FIGURE 1.8 : Logic of the numerical model : The model begins in the time domain by describing the probe field amplitude and the phase modulation due to Raman oscillations as a result of interaction with the sample. The effect on the probe beam is then estimated by transitioning into the frequency domain, where a long-pass filter is applied through the function $G(\omega)$. The differential signal $S(\tau)$ is obtained by transforming back to the time domain, yielding the temporal signal.

1.5.3 Interference with the sidebands in frequency domain

The spectral shift can be understood as resulting from the interference between the Stokes and anti-Stokes shifted spectral sidebands with the unaffected probe. This interference is influenced by the vibrational phase of the transient refractive index due to the complex nature of the spectra generated by CRS. At different vibrational phases, the anti-Stokes and Stokes scattered spectra can be either both real or both imaginary. When the contribution is real, the sidebands can interfere with the probe beam, producing a spectral center-of-mass shift. An effective way to track this shift is by plotting the FFT-modulated probe field spectra, represented as FFT$\{E_{\mathrm{mod}}(t,\tau)\}$. It is to be noted that for the simulation in the next section, the material prefactor has not been taken into account and hence the shift simulated is greatly exaggerated.

1.6 Results from simulation

Consider a scenario where a pump pulse with a pulse width of 10 fs excites a sample with two vibrational modes at 40 and 400 cm^{-1}. These cases demonstrate how the pulse width of the probe pulse affects the detection of different modes. The results of the simulation are shown for 3 cases of probe duration : 3000 fs, 300 fs and 30 fs.

Probe pulse duration 3 ps : Fig. 1.9 a) : A 3 ps probe pulse, typically used in CRS experiments, is simulated. The slower vibration at 40 cm^{-1} is depicted in red, while the faster vibration at 470 cm^{-1} is shown in orange, with the probe pulse in blue. The probe pulse is too long to be affected by either mode and thus no spectral shift occurs. Fig. 1.9 b) shows the probe pulse and the scattered Stokes and anti-Stokes frequency sidebands, with the two modes visible at their respective frequencies of 40 cm^{-1} and 470 cm^{-1}. As the bandwidths do not overlap, the vibrational modes do not interfere, resulting in no oscillations. Fig. (1.9) c) illustrates how the detector perceives the change in probe beam intensity through the filter while its delay is changed with the pump pulse arriving at $t = 0$. For the 3 ps probe, the vibrations are averaged, preventing the resolution of the individual vibrations and not following the sample's vibrational modes.

Probe pulse duration 300 fs : When the probe pulse duration is reduced to 300 fs, Fig. 1.10 a) shows that the pulse width is short enough to capture the rise and fall of the transient refractive index for the low-frequency mode at 40 cm^{-1}. The bandwidth of the probe pulse is close enough to the Stokes and anti-Stokes sidebands corresponding to this mode, resulting in interference between them, as demonstrated by the modulation in the probe beam in Fig. 1.10 b). Fig. 1.10 c), with spectral shift, indicates that it is possible to follow the transient refractive index of the 40 cm^{-1} mode, whereas the 470 cm^{-1} mode does not interfere with the probe, leading to its oscillations being averaged out, and no associated spectral shift is observed.

Probe pulse duration 30 fs : When the probe pulse duration is reduced to 30 fs, Fig. 1.11 a) shows that the pulse width is short enough to capture the rise and fall of the transient refractive index for both modes at 40 cm^{-1} and 400 cm^{-1}. Fig. 1.11 b) shows the probe pulse interfering with the Stokes and anti-Stokes sidebands of both modes,

as the bandwidth overlaps with the sidebands of both vibrational modes due to the short pulse duration. Consequently, Fig. 1.11 c) illustrates how it is possible to follow the transient refractive index of both modes, providing an integrated spectrum that tracks both oscillations.

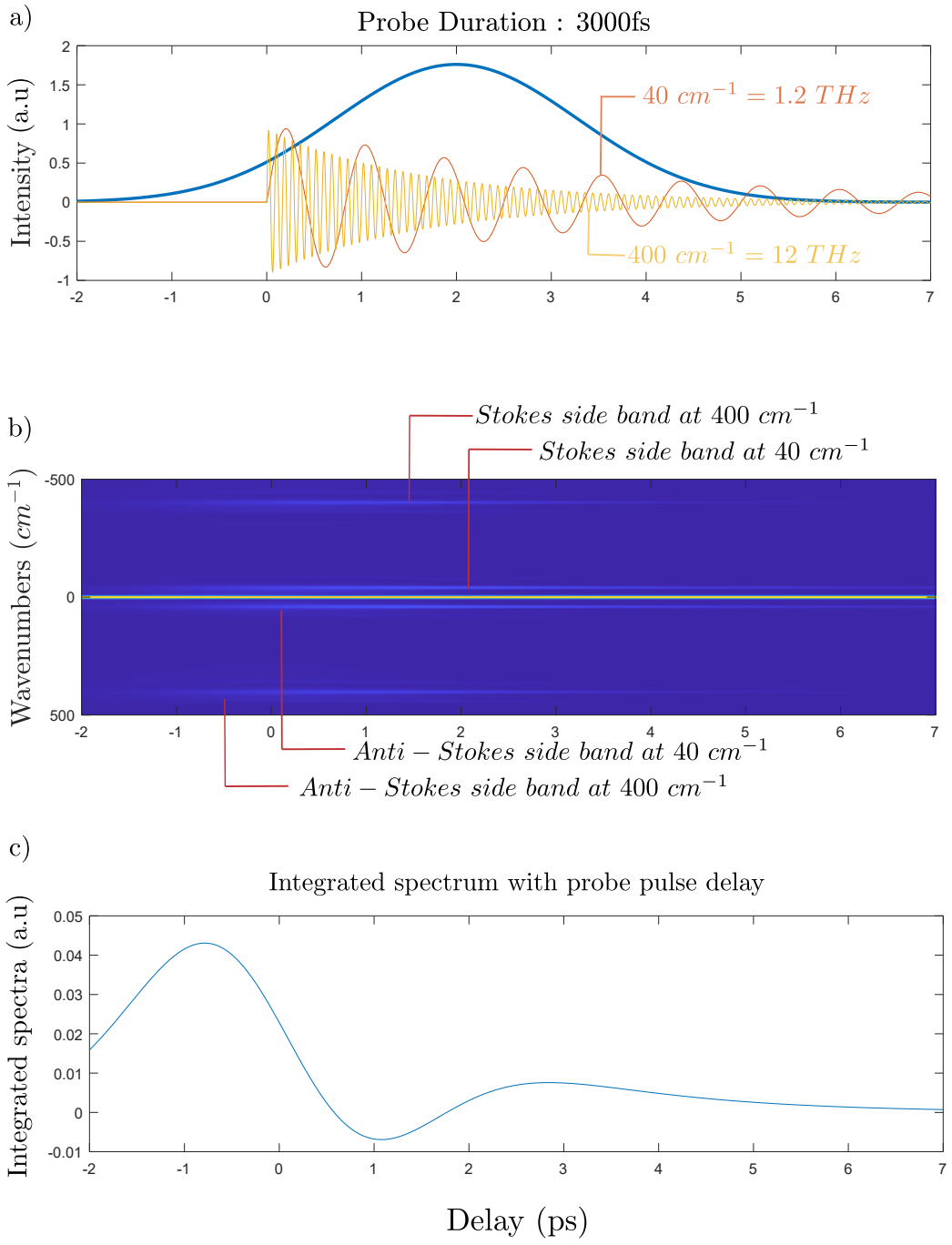

FIGURE 1.9 : a) shows the two vibrational modes at 40 cm^{-1} and 470 cm^{-1}, along with the probe pulse in time. b) shows the Stokes and anti-Stokes sidebands generated from the molecular vibrations at 40 cm^{-1} and 470 cm^{-1}. The probe beam, having low bandwidth, cannot interfere with these sidebands, and as a result, there is no spectral shift. c) shows the integrated spectrum over the range of $[0, 500]$ cm^{-1}. Since there is no spectral shift, it cannot follow the vibration of any mode of oscillation.

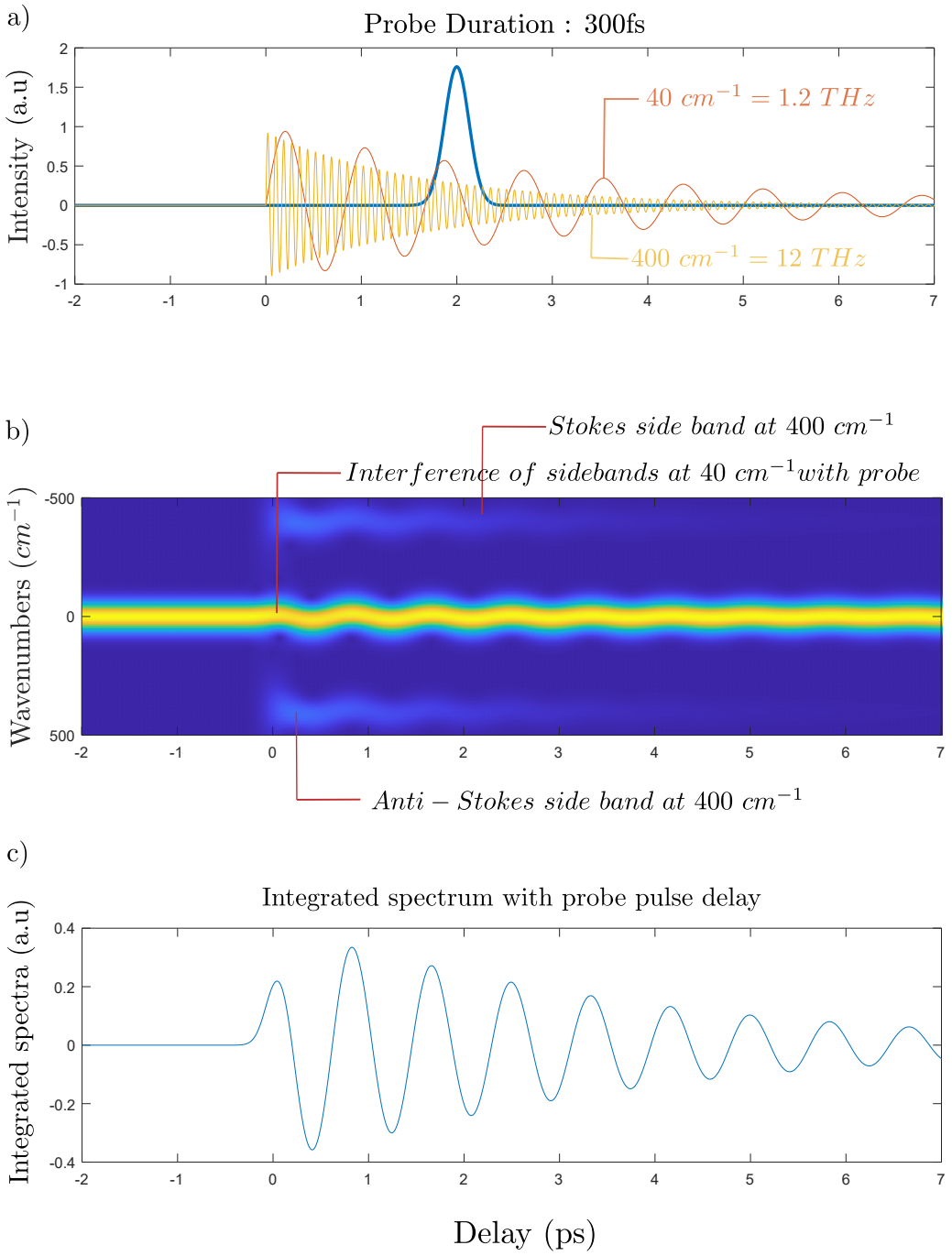

FIGURE 1.10 : a) shows the two vibrational modes at 40 cm^{-1} and 470 cm^{-1}, along with the probe pulse in time. It is interesting to note how the probe beam can observe the individual vibrations of the mode at 40 cm^{-1}. b) shows the Stokes and anti-Stokes sidebands generated from the molecular vibrations at 40 cm^{-1} and 470 cm^{-1}. The probe beam's bandwidth overlaps with the sidebands of the low-frequency mode, interfering with it. c) shows the integrated spectrum over the range of $[0, 500]$ cm^{-1}. Since there is a spectral shift due to the low-frequency mode, we only retrieve that vibrational mode.

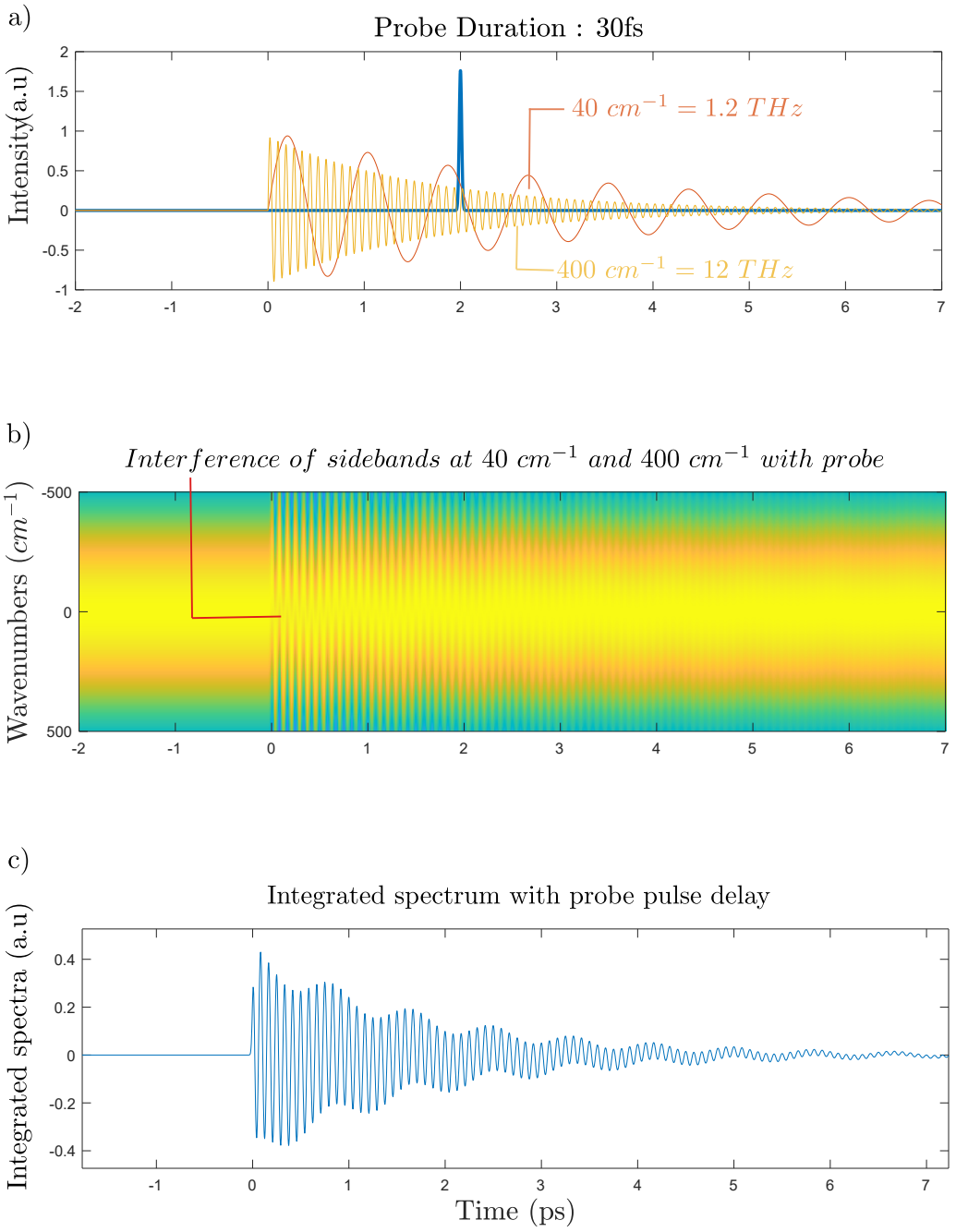

FIGURE 1.11 : a) shows the two vibrational modes at 40 cm^{-1} and 470 cm^{-1}, along with the probe pulse in time. It is interesting to note how the probe beam can now observe the individual vibrations of the modes at 40 cm^{-1} and 470 cm^{-1}. b) shows the Stokes and anti-Stokes sidebands generated from the molecular vibrations at 40 cm^{-1} and 470 cm^{-1}. The probe beam's bandwidth overlaps with the sidebands of both modes, interfering with them. c) shows the integrated spectrum over the range of $[0,500]$ cm^{-1}. Since there is a spectral shift due to both modes, we can retrieve the vibrational frequencies of both modes.

1.7 Conclusion

This chapter began with an exploration of the theory behind Raman scattering, addressing both spontaneous and stimulated processes. We examined the state of the art in Coherent Raman Scattering (CRS) for imaging applications, focusing on its advantages and limitations, particularly regarding broadband spectral imaging and low-frequency detection. The potential of a time-domain approach, specifically impulsive excitation, was discussed as a means to overcome these challenges. The core scheme of this thesis, Impulsive Stimulated Raman Scattering (ISRS), was introduced and its underlying theory was elucidated through simulations focused on spectral shift detection.

A key point to note is the phenomenon of chirping, where laser pulses undergo dispersion as they pass through optical elements, leading to an increase in pulse duration. This effect is especially significant for shorter pulses, which are crucial for exciting the entire vibrational bandwidth, making precise temporal control of the pulse essential. Additionally, as ISRS is a pump-probe technique, efficiently introducing a delay between the pump and probe pulses is critical. The following chapter will delve into the use of acousto-optic devices to effectively manage both chirp control and delay introduction.

2 Acousto optics for imaging

Summary

2.1 Introduction 47
2.2 Acousto-Optic Programmable Dispersive Filters : The Dazzler 48
2.2.1 Inside the AOPDF 48
2.2.2 Pulse shaping with the AOPDF 50
2.2.3 Delay with AOPDF 51
2.2.4 Comparison of HR and WB Dazzlers 52
2.2.5 Conclusion of the various parameters of the HR and WB dazzler 55
2.3 Acousto optic deflector as a delay line 55
2.3.1 Architecture and principle 56
2.3.2 Theory of ADL 57
2.3.3 Comparison of features with dazzler 60
2.4 Conclusion 60

2.1 Introduction

The previous chapter introduced the concept of pump-probe spectroscopy and microscopy, which relies on precise time control of the probe and pump. From this, it becomes clear that precise control over pulse shape and introducing a delay between the pump and the probe, while maintaining a short pulse duration, are crucial for time domain measurements. Various methods have been employed to introduce this delay.

The earliest pump-probe techniques, introduced by Zewail [53, 54], utilized mirrors on motorized translation stages, allowing for precise control of the temporal separation between the two pulses. However, these techniques proved slow and inefficient for imaging, despite providing high temporal resolution.

Since then, several new techniques have been developed to function as delay lines. In addition to mechanical ones, interferometric, acousto-optic, electro-optic [55], and all-fiber optical delay lines [56] have been developed. Interferometric delay lines often provide very high accuracy but are limited by the accessible delay range [57] although double interferometers have been used to overcome this barrier [58].

Pulse shaping has historically been interesting in ultrafast optics, nonlinear fiber optics, and optical communication networks. Consequently, there have been many innovations in optical pulse shaping, ranging from spatial light modulators (SLMs)[59, 60] and deformable mirrors[61-63] to holographic masks [64]. SLMs using liquid crystal modulator arrays or acousto-optic deflectors are widely used.

When controlling femtosecond pulses using acoustics, acousto-optic deflectors, modulators, acousto-optic tunable filters, and state-of-the-art Acousto-Optic Programmable Dispersive Filters (AOPDF) can be employed.

In this chapter, the pulse shaper and delay line used in our setup will be described, specifically an AOPDF delay line called "Dazzler," and a delay line based on an acousto-optic deflector. The working principles of these elements will also be explored.

2.2 Acousto-Optic Programmable Dispersive Filters : The Dazzler

Acousto-Optic Programmable Dispersive Filters (AOPDFs) were first introduced in 1997 by Pierre Tournois [65] for applications such as pulse compression and shaping [66, 67]. This was achieved by introducing an arbitrary phase and amplitude profile to an ultrashort pulse. Additionally, as a 'side-effect,' it also introduces a delay in time. This section describes the general working of an AOPDF, which is crucial for understanding how the interaction between acoustic and optical waves results in a time delay. Our discussion follows the work presented by Verluise et al. [66].

2.2.1 Inside the AOPDF

The AOPDF is a device that relies on the interaction between a polychromatic acoustic wave and a polychromatic optical wave that co-propagates. As with any phenomenon involving the interaction of different waves, a phase-matching condition is essential for the interaction between the acoustic and optical waves. Generally, for any three-wave mixing process, the phase-matching conditions are met by two criteria :

- **Momentum Conservation :**

$$\vec{k}_{\text{diff}}(\omega_{\text{opt,diff}}) = \vec{k}_{\text{in}}(\omega_{\text{opt,in}}) + \vec{k}_{\text{ac}}(\omega_{\text{ac}}) \tag{2.1}$$

- **Energy Conservation :**

$$\omega_{\text{opt,diff}} = \omega_{\text{opt,in}} + \omega_{\text{ac}} \tag{2.2}$$

where $(\vec{k}_{\text{diff}}, \omega_{\text{opt,diff}})$, $(\vec{k}_{\text{in}}, \omega_{\text{opt,in}})$ and $(\vec{k}_{\text{ac}}, \omega_{\text{ac}})$ stand for the wave-vectors and angular frequencies of the optical diffracted beam, optical input beam, and acoustic beam respectively.

Since the optical frequency is much higher than the acoustic frequency ($\omega_{\text{opt}} \gg \omega_{\text{ac}}$) by 7 orders of magnitude, the diffracted frequency is close to the optical frequency, and energy conservation is maintained. Thus, the only phase-matching condition to consider is wave vector conservation.

A temporal signal initiates an acoustic wave that propagates within a birefringent crystal along its z-axis with a velocity of v. The electromagnetic wave inside would experience two different dielectric coefficients, depending on their polarisation state

in the x and y axes. We consider an optical beam traveling through the crystal's fast axis, referred to as mode 1 directed along the x-axis. Strong acousto-optic interaction occurs only at the Bragg condition for conservation of momentum [68], as depicted in Eq. 2.1. If the incident beam has several frequencies, it only scatters for a particular acoustic frequency, provided the acoustic wave is chirped. Consequently, only one optical frequency is diffracted at position z, where a portion of the energy is diffracted into mode 2. Therefore, a pulse exiting at mode 2 will contain all spectral components that were diffracted at different positions within the crystal.

By modulating the longitudinally propagating acoustic wave in either the time or frequency domain, as well as adjusting its amplitude, the input pulse can be diffracted into a different shape. The diffraction efficiency is controlled by two important factors : the optical input and the electrical signal of the acoustic beam, described by the relation

$$E_{\text{out}}(t) \propto E_{\text{in}}(t) \circledast S\left(\frac{t}{\alpha}\right) \tag{2.3}$$

where the scaling factor

$$\alpha = \frac{\Delta n V}{c} \tag{2.4}$$

is the ratio of sound speed to light speed times the index difference between the ordinary and extraordinary waves. Here, $S(t/\alpha)$ represents the impulsive response of the filter applied to the input pulse for pulse shaping. In the frequency domain, this can be expressed as

$$E_{\text{out}}(\omega) \propto E_{\text{in}}(\omega) \cdot S(\omega\alpha). \tag{2.5}$$

These concepts are illustrated in Fig. 2.1, which depicts the interaction of a negatively chirped beam with an AOPDF. The acoustic wave within the crystal is exaggerated for visual clarity, showing increasing frequencies with varying amplitudes. As the beam passes through, the lower-frequency portion of the spectrum (red part) interacts with the acoustic wave first and becomes polarized along the slow axis. The higher-frequency portion (blue part) interacts later, towards the end of the crystal, allowing the slower components to "catch up" with the faster ones. This process effectively compresses the chirped beam, reducing the negative chirp through the acoustic wave that is generated within the crystal. Thus for the appropriate acoustic wave, one can get an FTL pulse as the output.

Throughout this thesis, two types of Dazzlers have been employed : the Wide-band (WB) and High-Resolution (HR) models. Their performance is compared across several key parameters, including the delay introduced, pulse shaping capabilities, resolution, and speed of operation, which are discussed below. Additionally, the derivation of the delay induced by the AOPDF and the pulse shaping mechanism is examined, as these are the two critical functions essential for our application. We will first examine the general derivation before discussing the specific properties of the WB and HR Dazzlers.

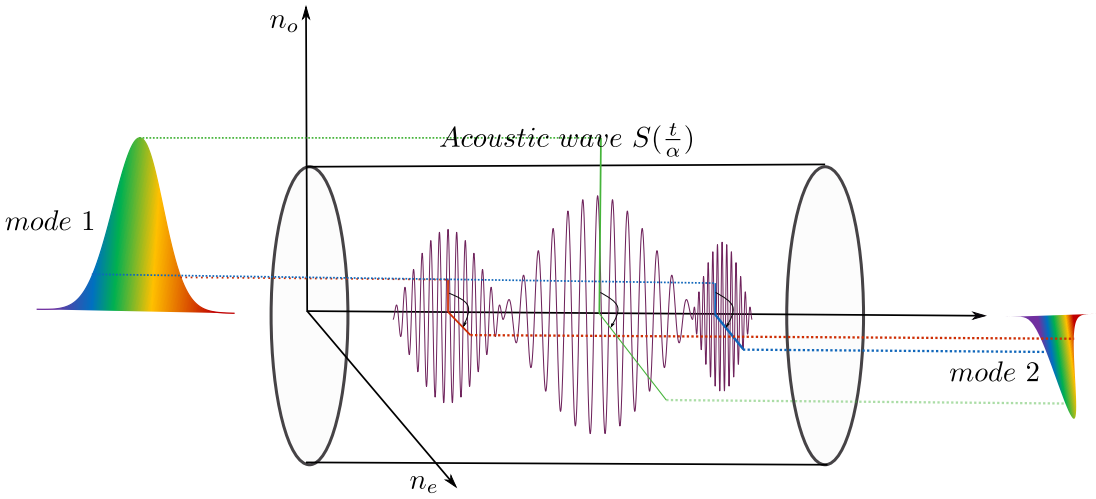

FIGURE 2.1 : **AOPDF working principle :** The figure illustrates a broadband chirped pulse polarized along mode 1, the fast axis, entering the AOPDF. The purple curve represents the acoustic wave within the birefringent crystal, modulated in frequency and amplitude. To correct the chirp, the red part of the spectrum must travel slower than the blue part. The acoustic wave filter $S(\omega\alpha)$ is designed to achieve this, reducing the negative chirp on the pulse at the output in the polarization state of mode 2.

2.2.2 Pulse shaping with the AOPDF

The pulse shaping mechanism in the AOPDF can be understood by examining the control of group delay. First, we define the wave vectors for both the fast and slow axes of the birefringent crystal. Let $k_1(\omega)$ and $k_2(\omega)$ represent the wave vectors along the fast and slow axes, respectively. These are given by the dispersion relation :

$$k_i(\omega) = \sqrt{\mu_0 \epsilon_i}\omega = n_i(\omega)\frac{\omega}{c} \tag{2.6}$$

Here, μ_0 is the permeability of free space, ϵ_i is the permittivity in the i-th axis, $n_i(\omega)$ is the refractive index, and c is the speed of light.

We assume the input wave is linearly polarized along the fast axis (mode 1). As it propagates a distance l_1 along this axis, it accumulates phase, which depends on the frequency ω as :

$$\phi_1(\omega) = k_1(\omega)l_1 \tag{2.7}$$

When the polarization state changes to the slow axis (mode 2) and the pulse propagates for a length l_2, the total phase accumulated by the pulse becomes :

$$\phi(\omega) = k_1(\omega)l_1 + \psi(\omega) + k_2(\omega)l_2 \tag{2.8}$$

where $\psi(\omega)$ is the additional phase acquired when the polarization rotates from mode 1 to mode 2.

For a birefringent crystal of length L, we can assume that the frequency components propagate a distance $z(\omega)$ in mode 1. The total accumulated phase across both modes is then :

$$\phi(\omega) = k_1(\omega)z(\omega) + \psi[z(\omega)] + k_2(\omega)(L - z(\omega)) \tag{2.9}$$

The acousto-optic interaction gives rise to phase matching conditions, ensuring efficient coupling between the optical and acoustic beams. This condition can be written as :

$$K(z) = k_2(\omega) - k_1(\omega) \tag{2.10}$$

where $K(z)$ is the instantaneous spatial frequency of the acoustic wave at position z.

The group delay for each optical frequency ω is determined by differentiating the phase with respect to ω. Using equations 2.9 and 2.10, the group delay $\tau(\omega)$ can be expressed as :

$$\begin{aligned}\tau(\omega) &= \frac{d\phi(\omega)}{d\omega} \\ &= \frac{dz(\omega)}{d\omega}(k_1(\omega) - k_2(\omega) - K(\omega)) \\ &\quad + \frac{dk_1(\omega)}{d\omega}z(\omega) + \frac{dk_2(\omega)}{d\omega}(L - z(\omega)) \\ &= \frac{z(\omega)}{V_{g1}(\omega)} + \frac{L - z(\omega)}{V_{g2}(\omega)}\end{aligned} \tag{2.11}$$

Here, $V_{g1}(\omega)$ and $V_{g2}(\omega)$ represent the group velocities in modes 1 and 2, respectively, which are given by :

$$\frac{1}{V_{g_i}(\omega)} = \frac{dk_i(\omega)}{d\omega} = \frac{n_{g_i}(\omega)}{c} \tag{2.12}$$

Thus, by controlling the position $z(\omega)$ where each optical frequency component is diffracted, we can effectively control the group delay $\tau(\omega)$. Additionally, the amplitude can be controlled by modulating the acoustic power at the position $z(\omega)$. This allows for precise shaping of the optical pulse.

2.2.3 Delay with AOPDF

Although the optical beam travels approximately 10^5 times faster than the acoustic wave, the perturbation induced by the acoustic wave within the crystal propagates at the velocity of the acoustic wave, denoted by V_{ac}. Assuming the crystal is non-dispersive for acoustic waves, the perturbation along the z-axis can be expressed as

$a(z + V_{ac}t)$.

As the acoustic wave propagates, the position of phase-matched diffraction, z_ω, becomes a linearly increasing function of time :

$$z(\omega, t) = z(\omega, t = 0) + V_{ac}t. \tag{2.13}$$

Consequently, the group delay is also affected and varies linearly with time as :

$$\tau_{\omega,t} = \tau(\omega, t = 0) + \alpha t, \tag{2.14}$$

where α has been defined previously as the ratio of sound speed to light speed times the index difference between the ordinary and extraordinary waves. This conversion factor characterizes how the propagation of the acoustic wave influences the optical propagation. It has units of fs/μs, indicating that the acoustic wave introduces an additional group delay of α across all optical frequencies. This ratio determines the speed at which the optical delays are swept. Fig. 2.2 shows a schematic of how the pulses are delayed as they interact with the acoustic wave.

The rate of optical delay sweeping is critical in establishing the time scale necessary for accurate conversion to the corresponding frequency in wavenumbers. Thus, calibrating this value is essential. In Chapter 3, we will examine how calibration is done using crystals with well-defined Raman peaks.

2.2.4 Comparison of HR and WB Dazzlers

In this thesis, we will employ the HR and WB Dazzlers for two distinct implementations of the ISRS scheme. To justify the selection of each Dazzler for specific applications, it is essential to compare their various characteristics. These characteristics are closely related to the properties of the birefringent crystal and the limitations of the RF generator that initiates the acoustic wave. The Dazzlers we utilize are specifically designed for 800 nm Ti :Sapphire laser systems. Below, we will summarize these characteristics in the table.

TABLEAU 2.1 : Comparison of properties between WB and HR Dazzlers

Property	**WB (Wide Bandwidth) DAZZLER**	**HR (High Resolution) DAZZLER**
Maximum delay introduced *Maximum delay that can be introduced to the optical pulse after it travels through the dazzler.*	3.5 ps	8 ps
Acoustic wave propagation time (t_{ac}) *Time taken by the acoustic wave to propagate the length of the crystal.*	25 μs	33 μs

Property	**WB (Wide Bandwidth) DAZZLER**	**HR (High Resolution) DAZZLER**
Acoustic waveform refresh rate *Capability of the RF generator to start a trigger that generates the acoustic wave.*	40 kHz	33 kHz
Scaling factor (α) *Defines how acoustic wave propagation affects optical wave propagation to achieve the delay.*	161 $\frac{fs}{\mu s}$	261 $\frac{fs}{\mu s}$
Diffraction efficiency *The power compared to input beam on the diffracted output of the dazzler that has been delayed and polarised at mode 2.*	70%	25%
Properties in Detection from Lock-in Amplifier Integration Time τ_c = 100 ns		
Sampling points for one window of the dazzler *The number of samples taken within the integration time would be the total time taken by the dazzler to scan the delay divided by the integration time of the LIA* $N = \frac{t_{ac}}{\tau_c}$	250	350
Delay Resolution *The Delay Resolution describes the smallest delay sampled through the LIA. Since the dazzler scans 'α fs every μs, the LIA would sample the scaling factor times the integration time* $\Delta t = \alpha \cdot \tau_c$	17 fs	26 fs
Limit of detection from sampling *The limit of detection range comes from the Nyquist sampling condition which states that the sampling rate must be at least twice the highest frequency present in the signal. As a consequence, since the sampling is determined by the delay resolution* Δ_t*, the condition gives the limit of maximum frequency detection as* $\Delta f = \frac{1}{2\Delta t}$	1034 cm^{-1}	633 cm^{-1}

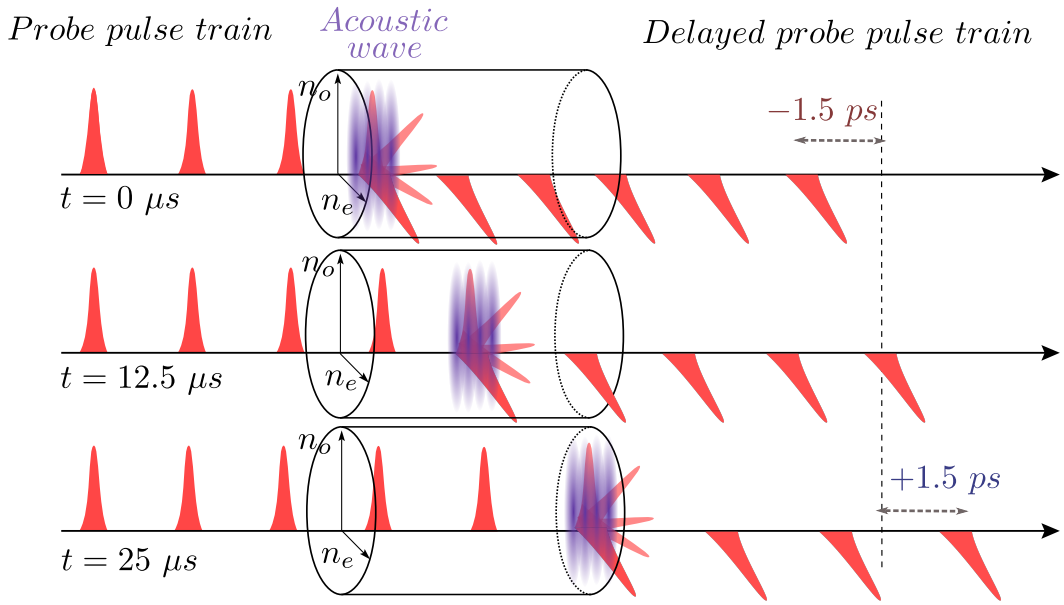

FIGURE 2.2 : The schematic shows how the delay is introduced on the incoming optical pulse polarised along the fast axis of the crystal. When the optical pulse interacts with the acoustic wave, it gets shifted into the other polarisation state which slows the optical pulse. Depending on where it meets the acoustic wave a differential delay is introduced which varies linearly.

2.2.5 Conclusion of the various parameters of the HR and WB dazzler

From the table, it is evident that the two Dazzlers exhibit distinct advantages and disadvantages. For example, the WB Dazzler has higher diffraction efficiency and a faster refresh rate compared to the HR Dazzler. However, this performance comes at the cost of a smaller delay range and limited pulse-shaping capabilities. Among these factors, the capability for pulse shaping is the most critical parameter in determining which Dazzler to use for a specific ISRS implementation. For higher bandwidth pulses, precise control over pulse width is essential, particularly when striving for an impulsive response using the ISRS technique.

The HR Dazzler excels in pulse shaping capabilities, primarily because, as chirp compensation increases, the acoustic wave occupies more of the crystal length. When the acoustic wave completely fills the crystal, the pulses at the edge of the crystal may become poorly shaped, leading to an output wave that does not accurately reflect the intended shape.

Although the HR Dazzler features a lower refresh rate for the acoustic wave, it compensates for this by being able to scan twice the delay range of the WB Dazzler, thereby providing more temporal information in a shorter time frame.

During the detection phase, the integration time of our Lock-In Amplifier (LIA) influences several parameters. The HR Dazzler has a higher number of sampling points and scans a longer delay, resulting in a slightly better delay resolution compared to the WB Dazzler. However, the scaling factor and integration time impose a detection limit based on sampling. The maximum frequency detectable with the HR Dazzler is 633 cm^{-1}. Thus, even if we can shape a sufficiently short pulse with the HR Dazzler, we are still constrained by the integration time. In this scenario, the WB Dazzler emerges as the ideal choice, despite its inferior pulse-shaping capabilities.

Nonetheless, both the WB and HR Dazzlers share a common limitation : they can only scan the delay continuously. Once the acoustic wave begins propagating in the Dazzler, it must traverse the entire length of the crystal, effectively introducing a fixed time delay. While the Dazzlers provide very high resolution, they are constrained by the range of delays they can introduce, which varies from 4.5 to 8 ps, depending on whether the WB or HR Dazzler is used. This limited fast delay range restricts the spectral resolution achievable from the Fourier transform of the time trace.

2.3 Acousto optic deflector as a delay line

The previous section discussed the working principle of an AOPDF, highlighting its various advantages and disadvantages. This discussion emphasizes the necessity for a delay line capable of quickly scanning a longer delay range for imaging purposes while remaining fully electronically tunable, akin to the Dazzler.

To address these requirements, a delay line developed by Fastlite has been employed, which builds upon and extends the pioneering work of Warren et al. [69]. This system,

known as the Agile Delay Line (ADL), operates at frequencies exceeding 50 kHz and features random access capabilities across a delay range of 50 ps. The ADL is based on an acousto-optic deflector (AOD) positioned in the Fourier plane of a zero-dispersion 4-f line. The setup of this system is illustrated in Fig. 2.3.

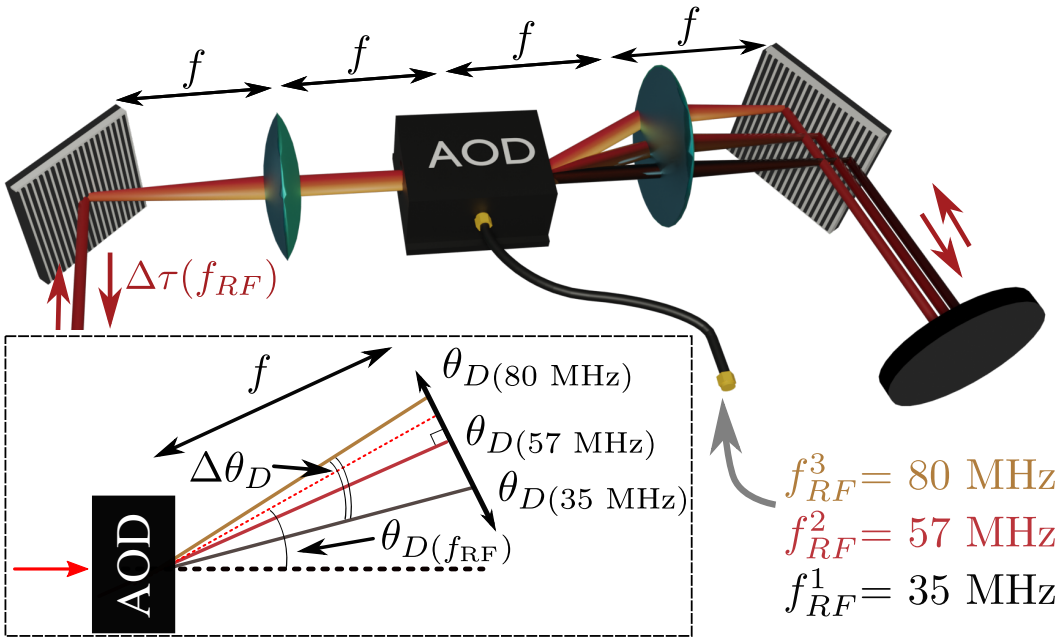

FIGURE 2.3 : Agile acousto-optic delay line (ADL). An acousto-optic deflector (AOD) is placed in the Fourier plane of a zero dispersion line (4f system). The AOD introduces a linear phase in the spectral domain resulting in a time delay. The latter is related to the AOD deflection angle θ_D which is controlled by the drive RF frequency (f_{RF}). The system is double passed with a mirror for improved (x2) delay range $\Delta\tau$ and to avoid beam walk-off with deflection.

2.3.1 Architecture and principle

A 4-f line [70] is a zero-dispersion optical system composed of two identical dispersive elements positioned at the conjugate planes of an imaging system with a magnification of -1. In practice, the system consists of two symmetrical sub-units, each featuring a blazed reflective diffraction grating and a pair of achromatic lenses with focal length f, positioned at a distance f from the gratings to form the imaging system. The input laser beam is first focused onto the grating of the initial sub-unit, which disperses the spectral components into the diffraction plane. These dispersed components are then collimated by the lens in the first sub-unit, directing them along a common propagation path.

The second sub-unit performs the inverse operation : the lens refocuses the spectral components onto the grating, effectively reconstructing the original wave structure.

By placing an acousto-optic deflector (AOD) between the two sub-units at a distance f from each lens (in a 4-f configuration), the beam can be deflected by an angle determined by the frequency of the quasi-continuous RF wave driving the AOD. This deflection results in a spatial displacement of the output beam in the conjugate plane. Due to the non-linear relationship between the diffraction angle and wavelength (unlike the Snell-Descartes law), this displacement introduces a net optical group delay proportional to the applied RF frequency [69].

For practical applications, this displacement can be compensated by using a double-pass configuration, which not only corrects the beam path but also doubles the achievable delay range. The output beam is separated from the input beam using a Faraday rotator and a polarizing beam splitter which is not shown in the figure.

The fast change in delay is done with an RF Driver designed for the ADL. The driver feeds a particular RF frequency to the AOD which changes the deflection angle linearly with a change in the frequency. The speed at which we can change the delay depends on this driver and how fast it can upload the new frequency to the AOD.

2.3.2 Theory of ADL

The theory behind the Agile Delay Line (ADL) designed by Fastlite is thoroughly detailed in the PhD dissertation of Ines Martin titled 'Low noise tunable parametric source and ultrafast agile delay line for coherent raman spectroscopy and imaging' to be defended in 2025 . This section will draw extensively on her work to provide the reader with a clear understanding of the working principles of the ADL.

The first step is to calculate the group delay introduced to the beam as it passes through the 4-f line of the ADL. This involves tracing the beam's path through the system, as depicted in Fig. 2.4, and deriving the path traversed by a beam diffracted from the grating and deflected by the AOD at an arbitrary angle to a central beam.

There are several approximations to consider in this calculation, such as the use of thin-lens optics which are achromatic. Additionally, the 4-f line is aligned for a beam with a central frequency λ_0, where the deviation $\theta_d(\lambda_0) = 0$, as depicted by the dotted line in the figure. In practice, this alignment is achieved by adjusting the RF frequency of the driver to the middle of its range, which corresponds to the center of the deflection angle range as well.

We calculate the optical delay introduced between the laser beams diffracted, as shown in green and blue. Consider the red beam incident on a grating with groove density σ, at an angle θ_{in}. The first grating diffracts the beam at different angles corresponding to the wavelength λ, denoted as θ_d in Fig. 2.4. Since we are using an achromatic lens, regardless of the path taken by the beam, the lens corrects for the delay introduced. Therefore, up until the acousto-optic deflector (AOD), the beam travels a distance $L_{G1-AOD} = 2f$.

Following the path from the AOD to the second lens (L_{AOD-L2}), we find that the beam at wavelength λ interacts with the AOD at a distance from the optical axis given

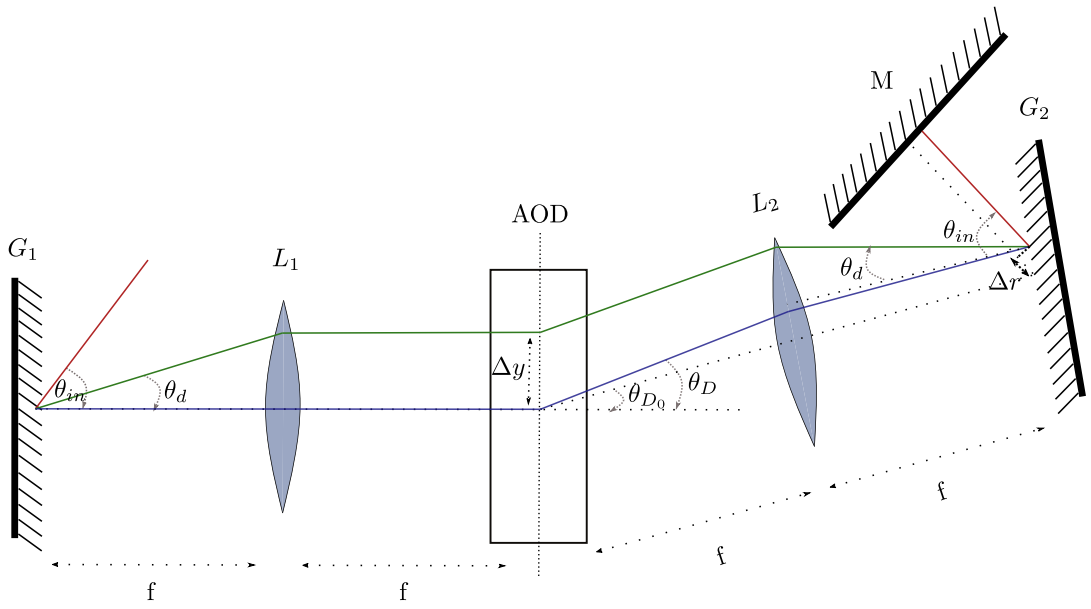

FIGURE 2.4 : An acousto-optic deflector (AOD) is placed in the Fourier plane of a zero dispersion line (4f system) which is the grating and lens pair. We assume a beam incident on grating G_1 at an angle θ_{in}. The AOD and the lenses are aligned for the dotted beam through the lenses L_1 and L_2 into the grating G_2 that is assumed to deflect at an angle θ_{D_0}. The path difference is calculated by considering that the dotted beam is deflected at an arbitrary angle θ_D. The path difference is calculated between this beam and another diffracted beam at arbitrary wavelength λ at an angle θ_d

by :

$$\Delta y = f \tan\left(\theta_d(\lambda) - \theta_d^0\right) \tag{2.15}$$

where $\theta_d(\lambda)$ is the deviation angle of the green beam at an arbitrary wavelength λ, and θ_d^0 is the deviation angle of the center beam which is zero in the 2.4.

Next, we define the angles θ_D and θ_{D_0} as the deflection angles of the AOD for an arbitrary wavelength λ and for the beam aligned with the 4-f system, respectively. Given this, the distance traveled by the green beam is given by :

$$L_{AOD-L2} = \frac{f}{\cos\left(\theta_D - \theta_{D_0}\right)} - f \tan\left(\theta_d(\lambda) - \theta_d^0\right) \sin(\theta_{D0}) \tag{2.16}$$

The path from the second lens to the grating is equivalent to $L_{L2-G2} = f$. The additional path difference, Δ_r, arising from the grating to the mirror (L_{G2-M}) can be derived using the grating equation.

$$\Delta_r = \frac{f \tan\left(\theta_D - \theta_{D_0}\right)}{\cos(\theta_d)} (\sin\theta_d - \sin\theta_i) \tag{2.17}$$

Applying the grating law for reflective gratings, we have :

$$\sin(\theta_i) - \sin(\theta_d) = m\sigma\lambda_0 \tag{2.18}$$

giving us

$$\Delta r = \frac{f \tan\left(\theta_D - \theta_{D_0}\right)}{\cos(\theta_d)} m\sigma\lambda_0 \tag{2.19}$$

and thus the path is given by

$$L_{G2-M} = \frac{f \tan\left(\theta_D - \theta_{D_0}\right)}{\cos(\theta_d)} m\sigma\lambda_0 + C \tag{2.20}$$

Where C is the common path traversed by both beams after they recombine through the second grating G_2 and is a constant. Thus, the total group delay, as a sum of each path, can be written as :

$$c\Delta\tau = 3f + \frac{f}{\cos\left(\theta_D - \theta_D^0\right)} - f \tan\left(\theta_d(\lambda) - \theta_{d_0}\right) \sin\left(\theta_{D_0}\right) + \frac{f \tan\left(\theta_D - \theta_{D_0}\right)}{\cos(\theta_d)} m\sigma\lambda_0 + C \tag{2.21}$$

A simplified expression for the total group delay in the ADL can be derived under the assumption of small deflection angles ($|\theta_D| \ll 1$ and $|\Delta\theta_D| = |\theta_D - \theta_{D_0}| \ll 1$) and a narrow optical bandwidth ($|\Delta\theta_d| \ll 1$). Under these approximations, and assuming thin, dispersion-less optics, the total optical group delay τ of the ADL, to second order in $\Delta\theta_D$ or $\Delta\theta_d$, is expressed as :

$$\frac{c\tau}{2} = 4f - f\Delta\theta_d\theta_{D_0} + f\sigma m\lambda_0 \frac{\Delta\theta_D}{\cos\theta_d} \tag{2.22}$$

where c is the speed of light. The factor of 2 on the left-hand side of Eq. 2.22 accounts for the double pass, while $m = \pm 1$ corresponds to the order of the acousto-optic diffraction.

As expected, the total group delay of the ADL scales linearly with the variation of the acousto-optic deflection angle $\Delta\theta_D$. This result matches that of [69] for $\lambda = \lambda_0$, but deviates for other wavelengths. The total group delay τ varies not only with the RF frequency f_{RF} but also depends on the wavelength. This dependency is twofold : through $f\Delta\theta_d$, and through the angular chromatism of the AOD, given by $\theta_D(\lambda, f_{\mathrm{RF}}) = \frac{\lambda f_{\mathrm{RF}}}{V}$, where V is the acoustic velocity.

Overall, this wavelength dependency introduces a variable group delay dispersion (GDD) on the delayed pulses.

From Eq. 2.22, the GDD can be quantified by computing the derivative of $\Delta\tau = \tau(\lambda, f_{\mathrm{RF}}) - \tau(\lambda_0, f_{\mathrm{RF}})$ with respect to the angular frequency :

$$\left.\frac{\partial\Delta\tau}{\partial\omega}\right|_{\lambda_0} = \frac{f\sigma\lambda_0^2}{\pi c^2\cos\theta_d^0}\left(\theta_D + m\theta_D^0 + \Delta\theta_D\sigma\lambda_0\frac{\tan\theta_d^0}{\cos_d^0}\right) \tag{2.23}$$

which reveals that the GDD of the ADL scales linearly with θ_D and therefore f_{RF}, even at $\theta_d^0 = 0$, a result which contrasts with the conclusion of [69]. By working with $m = -1$ the GDD can be made always negative and used to compensate the optical dispersion of internal (lenses, AOD) or external (microscope objective) optics and the effect of the variation of the GDD with f_{RF} can be mitigated by working with narrow optical bandwidths to limit the effect on the pulse duration.

2.3.3 Comparison of features with dazzler

The Agile delay line designed for our setup can introduce a delay of upto 50 ps with changing RF frequencies. This is almost 10 times more than the WB dazzler and 5 times more than the HR dazzler. We are free to program as many delay points as we want between arbitrary sets of RF frequencies that will determine the spectral resolution that we get. The RF generator needs a minimum of 20 μs delay between changing frequencies so that the beam passing through the crystal sees just one single frequency before seeing the next. This makes it slower than the dazzler that can scan continuously the 3 ps delay in 22μs. However, we will see how our flexibility in choosing delays can be used as a sort of compressed sensing in Chapter 3. We will also characterize its properties with respect to beam walk-off, transmission, beam shape, etc.

2.4 Conclusion

In this chapter, we have discussed how acousto-optics play a crucial role in pulse shaping and delay control in ultrafast optics, particularly in the context of ISRS. We have detailed the principles and operation of two different types of fast delay lines

used in our setup : the Acousto-Optic Programmable Dispersive Filter (AOPDF) and the Agile Delay Line (ADL). We also provided mathematical descriptions of how delay and chirp are controlled in both delay lines.

For the Dazzler, we explored how both the WB and HR models can continuously scan a small timescale of 4–8 ps, with refresh rates as fast as 25–33 μs. This makes them ideal for live imaging in pump-probe experiments where a smaller delay range is sufficient. However, a shorter time range inherently limits the achievable spectral resolution. In cases where better spectral resolution is required, the ADL serves as a more suitable option. Despite having a lower refresh rate, the ADL is capable of scanning a much larger delay range compared to the Dazzler, making it effective for applications requiring a bigger delay range for better spectral resolution.

3 Implementation of ISRS for Low Raman

Summary

3.1 Outline of the chapter . . . 63
3.2 Experimental setup . . . 63
3.2.1 Laser source . . . 64
3.2.2 Pump arm . . . 64
3.2.3 Probe arm . . . 64
3.2.4 Recombination and imaging unit . . . 64
3.2.5 Detection unit and aquisition . . . 65
3.3 Data acquisition with ScanImage using Dazzler as fast delay line . . . 65
3.3.1 Hyperspectral imaging with Scanimage at single pixel level . . . 66
3.3.2 Data Acquisition and synchronization of electronics . . . 67
3.3.3 Data processing . . . 69
3.3.4 Experimental results . . . 69
3.3.4.1 Raw Data . . . 69
3.3.4.2 Processed data and Spectrum . . . 70
3.3.4.3 Hyperspectral Imaging : Chemical detection . . . 73
3.3.5 Limitations and conclusion of ISRS implementation with the Dazzler . . . 75
3.4 ISRS with Agile Delay Line(ADL) as fast delay line . . . 75
3.4.1 Characterization . . . 76
3.4.2 Synchronisation of driver and acquisition with Scanimage . . . 78
3.4.3 ADL for ISRS . . . 78
3.4.3.1 Sequential scanning . . . 78
3.4.3.2 Agile delay scanning . . . 81
3.4.4 Conclusion on ADL for ISRS . . . 83

3.1 Outline of the chapter

In this chapter, the implementation of the ISRS scheme for low-frequency vibration detection is presented. Initially, the schematic will be described, detailing the various components and their respective functions. Subsequently, the applications of the two delay lines employed throughout this research will be discussed : the continuous scanning delay utilizing the Dazzler, and the sequential scanning with the Agile Delay Line (ADL). The use of these delay lines for video-rate imaging, capable of distinguishing chemical species and enabling selective detection, will be explored. This capability is facilitated by the fast data acquisition process for imaging, which was carried out using ScanImage, a MATLAB software designed for laser scanning microscopes. The data processing will also be described in detail.

3.2 Experimental setup

The setup shown here is reminiscent of the one described in Shivkumar et.al [71]. It is depicted in Figure 3.1.

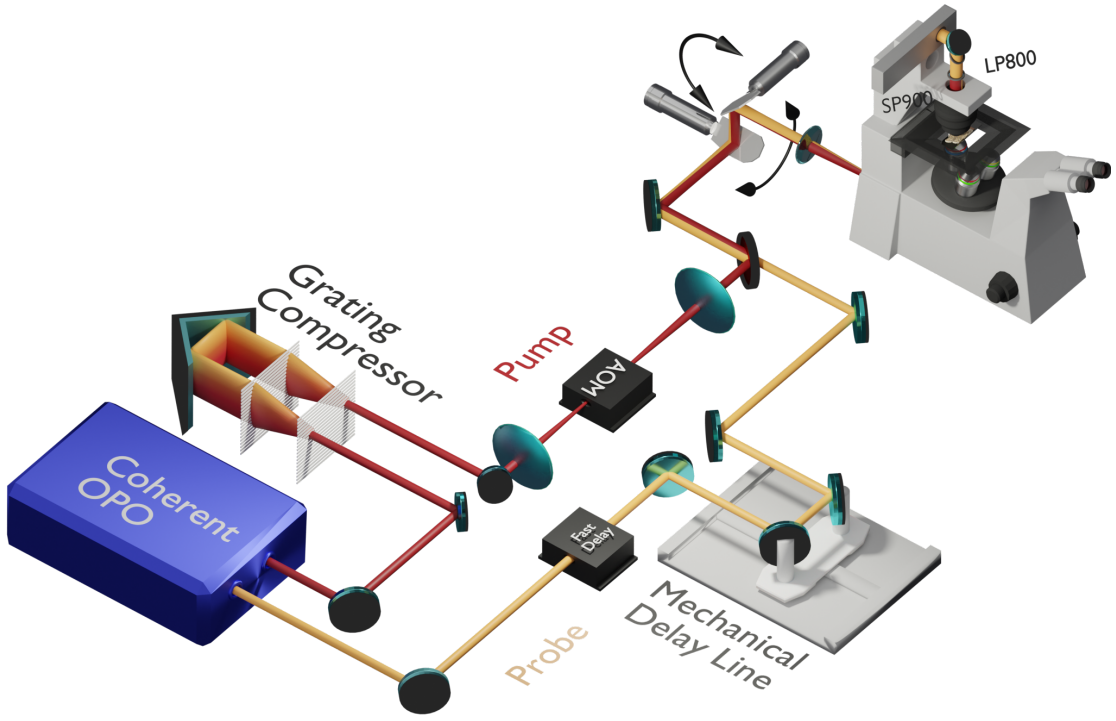

FIGURE 3.1 : Schematic of the experimental setup for ISRS

3.2.1 Laser source

We begin with the Coherent OPO depicted in Fig. 3.1. This OPO is pumped with a Titanium Sapphire (TiSa) laser that delivers a 170 fs laser output at a repetition rate of 80 MHz. The output has a wavelength of 800 nm with approximately 10 nm bandwidth. The OPO can bypass the 800 nm output, which is used as the probe, and generate an additional output tuned to 1045 nm, which is utilized as the pump. Approximately 700 mW is obtained at the output of the OPO for both the pump and the probe.

3.2.2 Pump arm

The path of the pump leads into a home-built grating compressor. This custom-made transmission grating pair, with 600 lines per millimeter (Wasatch Photonics, USA), performs a double-pass. This step is crucial for pre-compensating the chirp introduced by the additional optics through which the pump pulse travels before reaching the sample plane of the microscope. The grating compressor imparts a negative chirp, effectively counteracting the positive chirp added by the optics. Next, the pulse passes through the AOM (MT200-A0.2-1064, AA Opto-Electronic, France), which modulates the pump at 12 MHz for later detection with the lock-in amplifier (LIA). This modulation is achieved using an externally driven function generator (AFG1062, Tektronix, France). Ultimately, around 80% efficiency is achieved after the AOM and 40% efficiency from the grating compressor.

3.2.3 Probe arm

Following the probe pulse, it enters the 'fast delay line', which is either the AOPDF (the Dazzler) or the Agile Delay Line (ADL), whose working principle has been described in Chapter 2. It is important to note that the Dazzler serves two functions : acting as a fast delay line and controlling the chirp. With the ADL, chirp control is absent, but the pulse remains compressed depending on the delay range we scan. This is discussed later in the chapter in Section 3.4. Consequently, a grating compressor is unnecessary for chirp control on the probe arm. Additionally, a mechanical delay line (M 415.2S, Physik Instrumente, Germany) is incorporated into this path for two purposes : first, to determine the temporal overlap of the pump and probe, and second, to extend the scanning window of the WB Dazzler. This extension is necessary because the WB Dazzler's short scanning span of 4.5 ps yields a poor spectral resolution, and longer time windows can be acquired using the mechanical delay line.

3.2.4 Recombination and imaging unit

The pump and the probe are combined using a dichroic. The recombined beam is sent into the microscope (Eclipse Ti-U, Nikon, Japan) using galvanometric scanning mirrors (6215HM60, Cambridge Technology). The scan mirrors are conjugated to the

back focal plane of the microscope with a 3x telescope. The beams are focused and collected with 20x/0.75 NA air objectives (CFI Plan Apo Lambda 20X, Nikon).

3.2.5 Detection unit and aquisition

For the detection, the pump beam is blocked with two sets of optical filters (2 × FES0900, Thorlabs, USA, and 2 × FES1000, Thorlabs, USA). The back focal plane of the collection objective is conjugated onto the active area of two photodiodes. One photodiode detects the Raman response, while the other measures the transmission of the probe through the sample, using a piece of glass as a 90/10 beam splitter.

For measuring the Raman response, we use a commercial silicon photodiode combined with an SRS lock-in (SRS Lock-in Module, APE, Germany), which accepts a modulation frequency between 8 and 20 MHz and a sensitivity of 80% at 800 nm. The LIA receives the reference modulation frequency at 12 MHz from the same channel of the function generator fed into the AOM. An attenuator(10 dB) is used to ensure sufficient voltage for proper modulation through the AOM, without damaging the LIA. The gain is set to 48 dB on the LIA, beyond which we have post amplification. The relative phase between the reference and input signal is adjusted during measurements to optimize signal quality.

The other photodiode (DET100A, 8 MHz bandwidth) monitors the transmission of the probe through the sample, providing the transmission profile of the dazzler to normalize the Raman signal at each pixel.

We use Raman-induced spectral shifting to detect low Raman frequencies. As explained in Chapter 1, we employ an edge filter centered at the probe frequency, specifically a long pass (FELH800, Thorlabs, USA).

The output of the LIA is connected to a waveform digitizer card (Vidrio V-DAQ) with a 125 MHz sampling rate, which records the probe's spectral shift. All components are controlled using a custom-made Matlab application. The importance of well-triggered data acquisition will be discussed in the next section.

3.3 Data acquisition with ScanImage using Dazzler as fast delay line

ScanImage [72] is a MATLAB-based software that enables users to incorporate their scripts for real-time data processing once an image is acquired. While it is straightforward to add simple MATLAB scripts, modifying the core structure of ScanImage, such as altering the scanning sequence organization, is more challenging. Typically, ScanImage acquires an analog signal at each spatial point in the scanned sample, generating an image from the many acquired signals at each sample position, commonly used in confocal fluorescence microscopy. ScanImage also allows for the synchronization of the acquisition data stream with an external clock to define an acquisition window relative to this external signal. In our case for hyperspectral imaging, a multitude of time measurements for each spatial pixel has to be acquired. This section will explain

how we do time spectroscopy in Scanimage. This can work for any time spectroscopy technique and not just ISRS. For simplicity, we consider the case of using the WB dazzler as the fast delay line.

3.3.1 Hyperspectral imaging with Scanimage at single pixel level

For hyperspectral acquisition of data in ISRS, or any time domain techniques, it is necessary to acquire data in a 3-D cube : the spatial pixels in X and Y, and the time spectroscopy data in the third dimension. However, in commercial scan image software, the control of scanning mirrors is limited to a two-dimensional acquisition of data, namely the X and Y dimensions in space.

To do time spectroscopy we introduce a new strategy. At first, we want the galvanometric scanners to place the spatially and temporally overlapping pump and probe beams at one location on the sample (x,y). The next step is to acquire the time trace corresponding to the scanning window of the Dazzler (25μs). For this, we slow down the scan along X direction by a factor of several hundred, but at the same time perform high-speed acquisition of data as the dazzler scans its delay. This leads to the concept of a macro-pixel in the X direction that stores the dazzler delay scan while the Y direction has the size of a point spread function (PSF). The result is the construction of a 2D image of $(N_x \times N_\tau) \times N_y$, where N_τ is the number of acquisition points in time during the delay line scan (270 points), N_x is the number of macro-pixel along the X axis that contains N_τ measurements and N_y is the number of spatial measurement points along the Y axis.

Once the acquisition is done, the scanning mirrors move onto the next spatial pixel to repeat the process. In this way, we wrap the time dimension in the X direction and leave the Y unaltered. This is represented in Fig. 3.2 a) where we pictorially represent the scanning process over a FOV containing a smiley face. The small red bars show the scanning in X direction for a dazzler delay scan τ giving us an elongated macropixel.

This leads to an asymmetric point spread function (PSF) for this 'macro pixel'. This is represented in Fig. 3.2 b) for the case of a 200 μm FOV. The scanning mirror keeps moving during the delay scanned on each pixel, leading to the extended PSF in the X direction. Along the Y axis, the microscope resolution is around 1 µm (limited by the under-filling of the objective back focal plane). Along the X axis, the macro-pixel elongation X_{Daz} is related to the distance scanned during the $\tau = 25\mu s$ of the Dazzler delay scan, which is related to the field of view (FOV). The X mirror scans continuously a region of size FOV in a time of $N_x \times \tau$. This means that during a single Dazzler window, the mirror scans in the X direction a line of length

$$X_{Daz} = \frac{FOV}{N_x} \tag{3.1}$$

This leads to an asymmetric PSF whose aspect ratio is the FOV divided by the number of macropixels N_x. This asymmetric PSF vanishes when the FOV is sampled at the

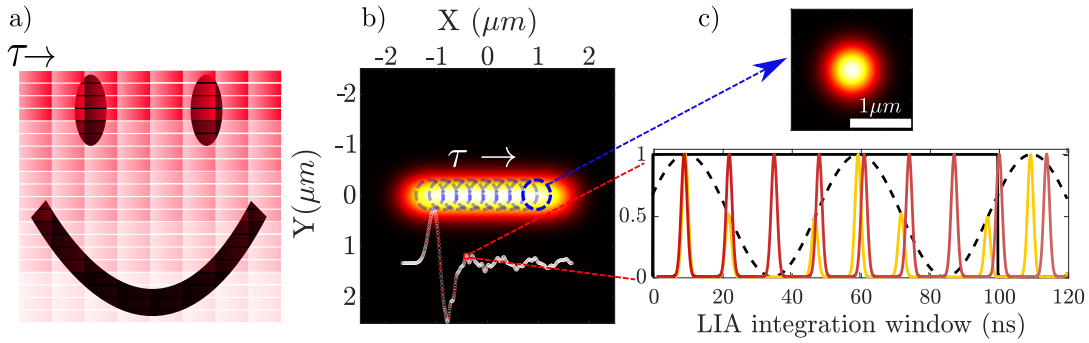

FIGURE 3.2 : a) Schematic description of the scanning process over a field of view containing a smiley face. The 'macro-pixel' PSF is defined by the small red bars where the real PSF (top insert in c)) scans the sample along the X-axis slowly during the time τ. b) The 'macro-pixel' is therefore elongated along the X axis and has a dimension of ~2μm while its dimension along the Y axis is ~ 0.5μm. c) Pictorial representation of time delay points

limit of diffraction with one pixel per micron, as then the distance scanned by the mirror in 25μs is one micron.

During the Dazzler delay scan τ, the DAQ card is sampling $N_\tau = 270$ points which correspond to the number of pump-probe delay samples that are acquired per pixel. One time delay point corresponds to an LIA integration time which in our case is 100ns. This is shown in Fig. 3.2 c) for a time sequence of 120 ns. The pump pulse is in yellow, and the probe in red is delayed in time. The dotted lines follow the modulation of the pump with the AOM. The solid black line shows the integration time of the lockin. For an 80 MHz repetition rate, the LIA would thus average 8 pulses of the probe during its integration time.

The proposed scheme makes ScanImage compatible with hyperspectral imaging, at the single pixel level. It is also easily extendable to any other situation where a time-dependent signal is rapidly acquired at each pixel during the scanning process.

3.3.2 Data Acquisition and synchronization of electronics

Acquiring the time-spectroscopy data requires proper synchronization of all the electronics at play. The different electronics involved are shown in Fig. 3.3

The first step is to synchronize the trigger to the dazzler RF generator (that starts the scan) and the data acquisition (DAQ). For this, we use two identical digital trigger signals generated from the FPGA available with the DAQ cards. The first trigger feeds into the dazzler RF generator box that sends the signal to start scanning the delay (Purple line). The second trigger is fed into the DAQ to pass the information to start acquiring the time delay data (Blue line). This is repeated as we scan across each spatial macro pixel. With this, it is possible to properly synchronize the triggering of

the delay scan and the acquisition of the data.

Another role of the trigger signal is to help solve the jitter that could come from the DAQ clock. This arises because the scanning mirror's flight back time is not necessarily a multiple of the DAQ sampling time. This second trigger helps properly register each macro pixel.

There is a certain ambiguity with the delay between the trigger into the dazzler RF box, and the actual scan of the delay line. However, this value being fixed can be measured with a calibration sample for which we have used a Barium Germanate (BGO) crystal. In practice, the dazzler trigger starts a bit before DAQ trigger so that it accounts for this delay. This is in the range of a few 10s of microseconds.

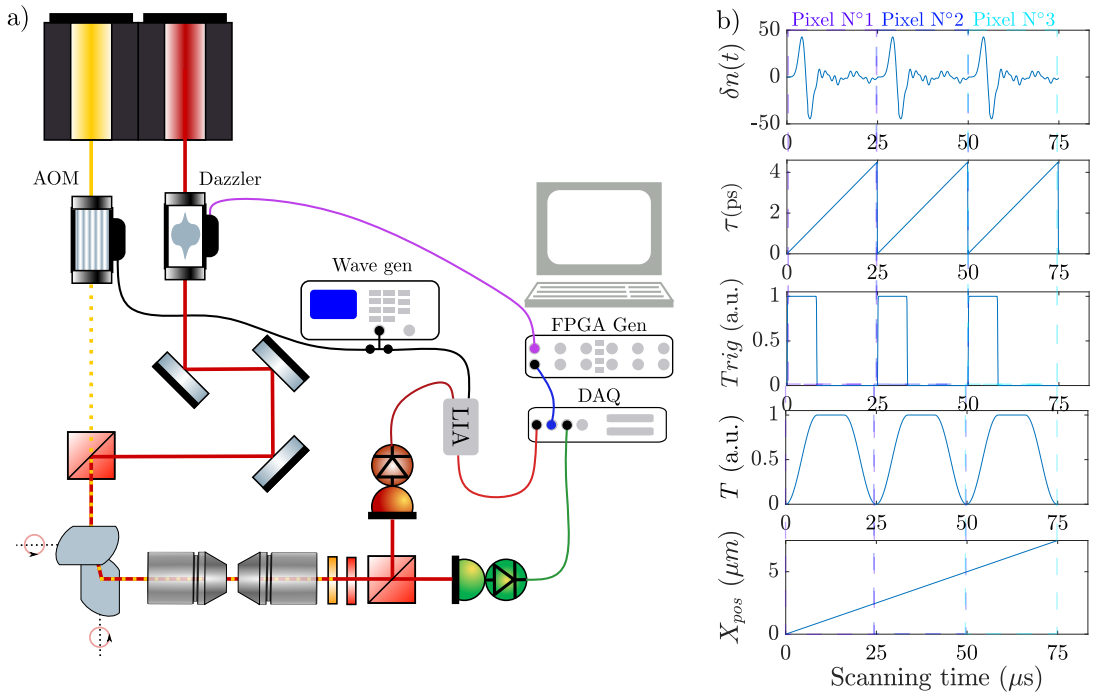

FIGURE 3.3 : a) Electronic layout of the experiment, two trigger signals generated by an FPGA synchronize the delay line (Dazzler) and the data acquisition (DAQ). These are shown as purple and blue lines respectively. The modulation from the wavegenerator that controls the AOM, and provides the reference signal into the LIA is shown in black lines. The red photodiode corresponds to the Raman channel and the green one to the transmission channel. The raw data from both photodiodes are sent into the DAQ, shown as red and green lines respectively. b)Variations of important parameters during scanning

Fig. 3.3 b) summarizes variation in important parameters during acquisition. The first one shows the refractive index change perceived in the LIA on each macro pixel. The second one shows how each pixel is defined by the time taken by the dazzler

to scan its delay. The third is the trigger that tells the dazzler to start the scan and simultaneously to the DAQ to start the acquisition. The fourth one shows the fact that the transmission of the dazzler rises and falls at the ends of the 25 μs scanning window. The fifth graph shows how the Galvo mirror moves while scanning the sample FOV.

3.3.3 Data processing

To generate hyperspectral images we thus need 3 channels in the DAQ :

- **Channel 1 : Raman channel -** LIA data that corresponds to Raman data collected through the APE photodiode.
- **Channel 2 : Transmission Channel -** The transmission of the probe pulse on the second photodiode at each pixel.
- **Channel 3 : Trigger channel -** The synchronization signal to start the Dazzler scan and the simultaneous fast acquisition.

In the end, we obtain three 2D matrices of size $(N_x \times N_\tau) \times N_y$, each corresponding to the three different DAQ fast acquisition channels. With the DAQ channel 3 for trigger, we can remap the 2D data to the corresponding hyperspectral cube. The final result is to get two 3D matrices that have a size of (N_x, N_y, N_τ) that are the Raman and transmission channels.

In case the vibrations of the sample of interest live longer than 4.5 ps, we need to move the mechanical delay line to scan the next window of interest. The transmission channel helps with stitching these multiple windows of the dazzler. Since each time window would have an additional modulation following the transmission of the dazzler, for proper stitching we need to normalize the delay graph with the corresponding transmission curve. This is because as shown in Fig. 3.3 b) the Dazzler transmission is not flat across the whole scan range, but falls at the edges of its scanning window. The recombination of the window is achieved by interpolating the data at the points where the falling transmission curve of window n intersects with the rising transmission curve of window $n+1$. Given that the expected signals are sums of decaying sinusoids, we employ an interpolation algorithm that ensures the continuity of both the signal and its first derivative, thereby minimizing errors in the reconstructed spectrum. This process produces a 3D matrix of dimensions $(N_x \times N_y \times (N_\tau \times N_{\text{window}}))$. To generate the hyperspectral cube, a fast Fourier transform is applied to this time-spectroscopy signal for each spatial pixel.

3.3.4 Experimental results

3.3.4.1 Raw Data

To ensure all the electronics are synchronized, we have tested on a calibration sample of BGO that has a size of 5 × 5 mm. This crystal shows a very narrowband vibrational

resonance around $89cm^{-1}$ which gives long oscillations in the time domain. We image a corner of BGO to get a contrast in the image with (N_x.N_y)=64*63 pixels and 300 μm FOV. We start with the processing of the transmission channel followed by the Raman channel.

Figure 3.4 a) shows the raw data we get from the transmission channel of the probe that scans a delay spanning $N_\tau = 270$ acquired sample points. This high aspect ratio raw image is averaged across each macro pixel to give the final transmission Image shown in 3.4 b). For the Raman channel (Fig. 3.5) we see the raw image similar to that

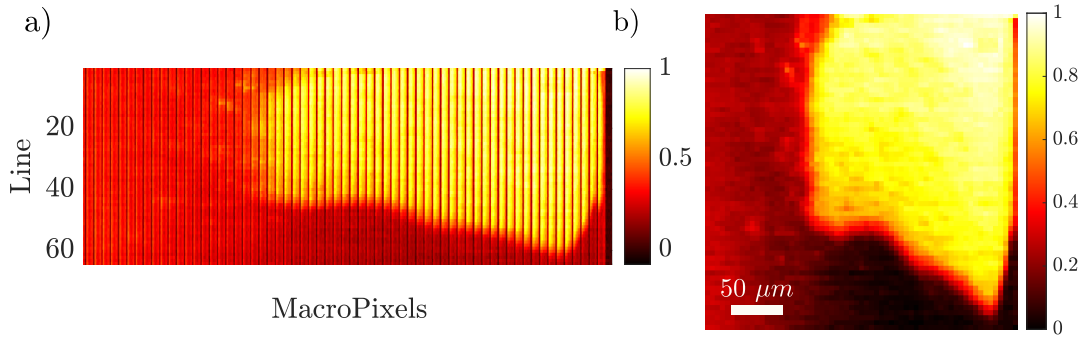

FIGURE 3.4 : a) Raw data obtained from ScanImage for the transmission channel b) Transmission image of a BGO crystal.

of the transmission with the high aspect ratio. Zooming into the first 12 lines in Y and 520 acquisition points on X, we clearly see the variation of probe intensity with the spectral shift. The huge peak in red and blue corresponds to the overlap of the pump and the probe. Following this, we see the transient vibrations that last the length of the acquisition.

Figure 3.6 shows two intensity sections along the X-axis for the refractive index variation (in blue) the Dazzler transmission (in red), and the DAQ trigger (dashed line).

A Dazzler delay scan (25μs) corresponds to $N_\tau = 270$ sample acquisitions to enable the capture of the transient refractive index, at each macro-pixel. In this specific example, the size of the macropixel along the X-axis is 1 μm. The repeatability from one Y line to another is correct but shows the necessity to normalize by the Dazzler transmission intensity for proper acquisition of the refractive index time trace.

3.3.4.2 Processed data and Spectrum

The data processing is performed for each pixel. The Raman data is normalized to the transmission channel's intensity. A Tukey window with a sharp slope is used to remove the pump-probe overlap, which could distort the FFT spectrum. A MATLAB function applies zero-padding to the signal, yielding the vibrational spectrum shown in Fig. 3.7 a). The first curve is a single dazzler window scan, the second shows the multiple

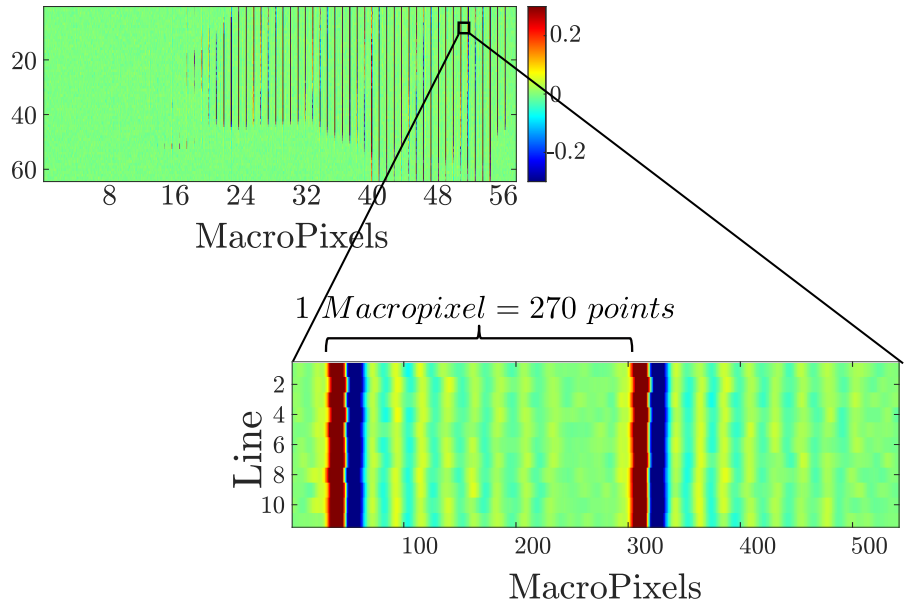

FIGURE 3.5 : a) Raw data obtained from ScanImage for the Raman channel (bottom) and the zoom on two macropixels along the X direction and 12 lines along Y.

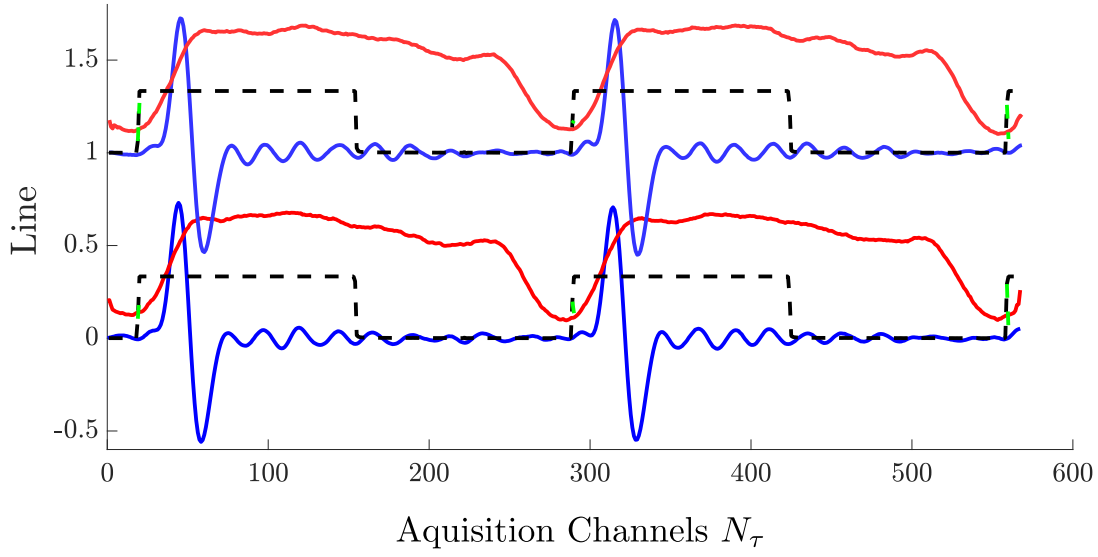

FIGURE 3.6 : Plots of the three channels, vibrational refractive index transient (blue), Dazzler transmission (red), and the DAQ trigger (dashed line).

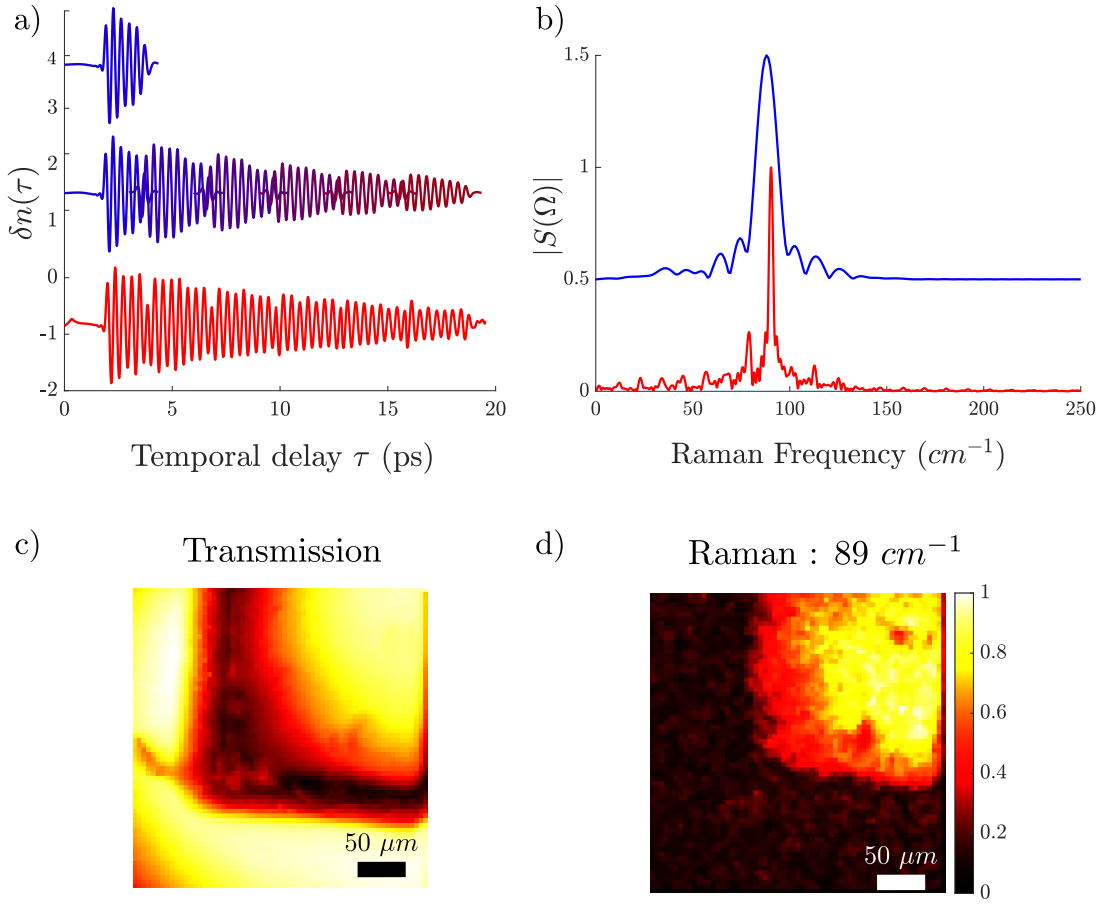

FIGURE 3.7 : a) Time traces obtained for a single window (top,blue), for each position of the mechanical delay line (middle, blue), and the interpolated time trace (red). b) Spectrum obtained from a single Dazzler window (blue) and multiple windows (red) demonstrating the spectral resolution. c) Transmission image (300 μm FOV) of the corner of a BGO crystal d) Hyperspectral image obtained at 89 cm^{-1} showing the chemical contrast .

dazzler windows that are taken by moving the mechanical delay line and the last one shows the interpolated and normalized curves. When the FFT is performed with the time trace acquired within a single scan of the Dazzler window (that corresponds to 4.5ps) the spectral resolution is limited at 10 cm^{-1} FWHM as shown in Fig. 3.7 c (blue curve). When FFT is performed on the interpolated time traces, in this particular case 18 ps, it leads to an increased spectral resolution of 2 cm^{-1} FWHM. However, this slows the imaging speed. Generating a hyperspectral image for a single dazzler window over 64 × 64 μm with a 1 μm resolution as shown in Fig. 3.7 d) takes 130 ms (≈ 8 Hz). The multi-time windowing slows down the imaging process, as moving the mechanical delay line takes 0.15 s, which means that this increased spectral resolution scheme lowers the frame rate to 0.6 Hz.

3.3.4.3 Hyperspectral Imaging : Chemical detection

Having demonstrated the setup on a calibration sample, we check on some pharmaceutical samples. We look at two samples of interest : Anthracene ($C_{14}H_{10}$) and Acetaminophen ($C_8H_9NO_2$). The samples of Anthracene crystals were received thanks to The Weizmann Institute (Rehovot, Israel). The acetaminophen samples are synthesized following the technique in [73]. The crystallization procedure is described below.

Crystallization of Acetaminophen
A supersaturated acetaminophen solution is prepared with 3.02 g of acetaminophen in 10 ml deionized(DI) water. The initial temperature of the solution is kept at 80°C. The solution was left to cool on a petri dish and the solvent was allowed to evaporate completely for a week. Crystals up to a few mm in size were formed with this method.

We combined the anthracene crystals with the smaller pieces of acetaminophen crystals. Both being transparent are not distinguishable through the transmission image (Fig. 3.8 a)). The Fig. 3.8 d) shows the Raman spectra averaged over the whole FOV. This gives 3 peaks corresponding to the different samples in the blue curve. However, when we average the spectrum at different regions of interest (ROI), there is a chemical distinction in the species. We note that the peak at 56 cm^{-1} corresponds to acetaminophen and the one at 37 cm^{-1} is that of anthracene. These are the peaks we see in Fig. 3.8 d) in red and yellow respectively. The hyperspectral images have been filtered in Matlab with a gaussian filter of size 2 × 2. The integrated spectrum of ROI 3 on Fig. 3.8 a) shows no distinctive Raman signature. The 64 × 63 pixels hyperspectral coherent Raman images shown in Fig. 3.8 were acquired at a rate of ≈ 7 frames/second (7 Hz) over a FoV of 500 × 500 μm. The resolution was 8 μm along the X axis and 1 μm along the Y axis.

We have thus demonstrated close to video rate low vibrational frequency chemical imaging. This tool makes low-frequency Raman imaging practical for investigations in pharmaceutical, material, and possibly biology fields.

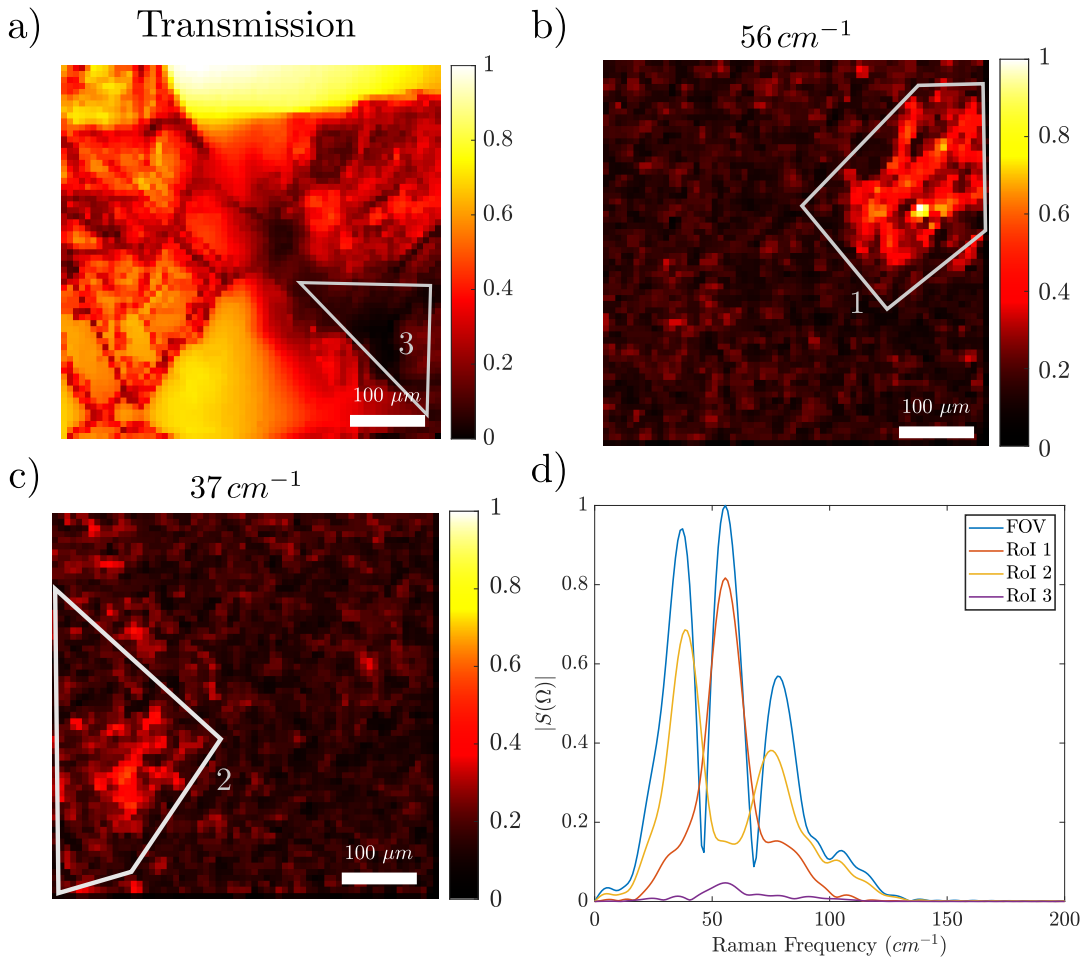

FIGURE 3.8 : a) Transmission image (500 μm FOV) of a sample composed of a mixture of acetaminophen and anthracene crystals; b) Hyperspectral image obtained at 56 cm^{-1} highlighting acetaminophen. c) Hyperspectral image obtained at 37 cm^{-1} highliting anthracene. d) Spectra obtained while averaging on either the whole FOV (blue), on Fig. 3.8 b) ROI 1 (red - acetaminophen), on Fig. 3.8 c) ROI 2 (yellow - anthracene) and Fig. 3.8 a) ROI 3 (purple - void).

3.3.5 Limitations and conclusion of ISRS implementation with the Dazzler

In this section, we have seen how to implement ultrafast hyperspectral chemical Imaging in the low Raman region with less than 200 cm^{-1}. We have demonstrated the possibility of video-rate imaging with this setup. However, a limitation associated with this is that we only consider the 4.5 ps scan window of the Dazzler which limits the spectral resolution.

In terms of the limit of detection, several factors play a role. The first limitation would be the bandwidth of the pump excitation laser as mentioned in Chapter 1. With its limit of 10 nm bandwidth, one can excite Raman peaks up to 160 cm^{-1}. Although this limit can be lifted with a shorter laser pulse, we would still be limited by the integration time of the LIA, as faster vibrations could be averaged if it is too high. To calculate this limitation we take into account the time delay scanning of the Dazzler α=161 fs/μs. Considering that the shortest integration time of the Dazzler is 100 ns limited by our LIA. This corresponds to pump-probe sampling, Δt, of 17 fs. Applying Nyquist theorem, the highest Raman vibration detectable would be

$$f_{max} = 1/(2 * \Delta t) \tag{3.2}$$

For our case it turns out to be 29 THz which corresponds to $\Omega_{max} = 967cm^{-1}$. This means excitation is the strong limiting factor here and not the detection. To access the full vibration bandwidth allowed by the Dazzler delay scaling, one must properly sample the incoming electronic signal, where the use of electronic filters to reduce the noise level must be done carefully, as filtering the electronic signal can reduce the detection bandwidth. In our case, using a 12 MHz modulation, a 1 MHz filter limits the accessible vibrations to 207 cm^{-1}. The detection bandwidth is hence limited by four factors : the pump laser bandwidth, the probe laser bandwidth, the delay scaling of the Dazzler, and the DAQ sampling speed, or electronic filtering.

Additionally, the choice of windowing in Fourier transformations for time-domain SRS methods may affect the frequency-domain line width, and depending on the material response may modify the line shape.

3.4 ISRS with Agile Delay Line(ADL) as fast delay line

Chapter 2 discussed how an acousto-optic deflector can be used as a fast delay line for hyperspectral imaging. We have discussed its design and working along with the theory in detail. This section will examine how we implement it as a delay line for ISRS. The two ways it can be used will be addressed : first, to scan sequentially, and second, to scan at random delays for selective detection. A brief discussion will also be included on the effect of sampling on the loss of information in spectra.

3.4.1 Characterization

When designing a delay line for ISRS, it is crucial to ensure a linear delay with changes in RF frequency, minimize the chirp introduced through the delay line to avoid significant effects on the pulse width, maintain the shape of the pulse after traversal, and prevent any beam walk-off as the delay is scanned. For this, we characterized the ADL with a 170 fs FTL titanium sapphire (TiSa) laser (80 MHz repetition rate - Chameleon, Coherent) with 800 mW output power centered at 800 nm.

Delay intoduced

To measure the ADL delay $\Delta\tau$ with RF frequency, we generated in a BBO crystal (type I, 500 μm length) the sum frequency generation (SFG) at 453 nm between the 800 nm TiSa laser and a 1045 nm OPO. Having found the SFG for a particular delay on the ADL, we shift to the next frequency on the RF box. The mechanical delay line is moved until we get back the temporal overlap generating the SHG again. The distance moved by the mechanical delay line is noted and the process is repeated over the range of the ADL. Thus by changing the optical path length between the TiSa and the OPO, $\Delta\tau$ can be retrieved for different f_{RF}. From Fig. 3.9 we see the ADL can scan 50 ps with a linear dependence of 1.16 ps/MHz.

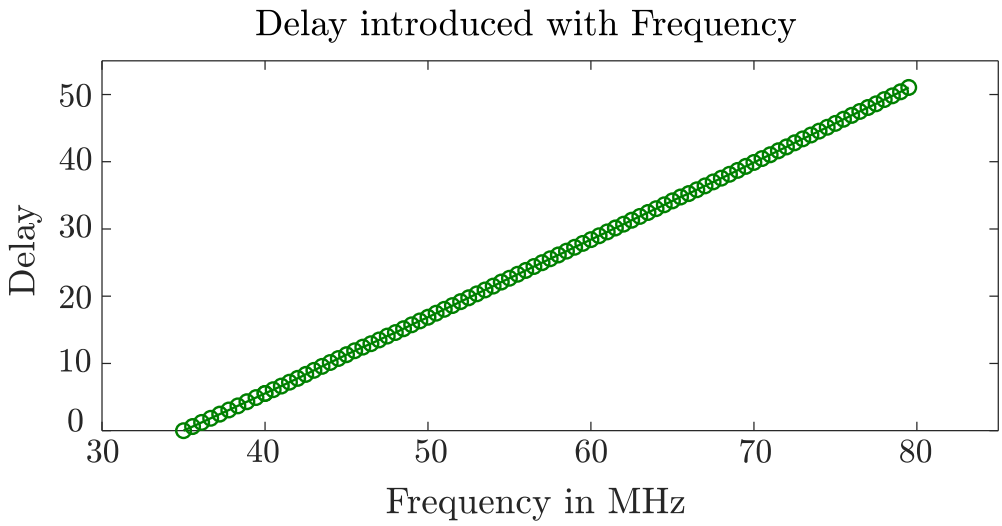

FIGURE 3.9 : Measured ADL delay with RF frequency. The slope is 1.16 ps/MHz

Chirp variation

The ADL introduces a second-order chirp to the beam passing through it. This can be observed by looking at the change in pulse width at the exit of the ADL. For ISRS, the pulses have to be Fourier transform limited to make sure we excite and detect the bandwidth of interest. To characterize this we have measured the pulse width (Fig. 3.10) at the output of the ADL (green) using an autocorrelator (CARPE APE) and

also at the sample plane (yellow). The CARPE autocorrelator is equipped with an external detector that can be integrated into the microscope stage, allowing for direct pulse width measurements at the sample plane. It is observed that it has a quadratic dependence on the f_{RF}. The variation over the delay range is about 140 fs.

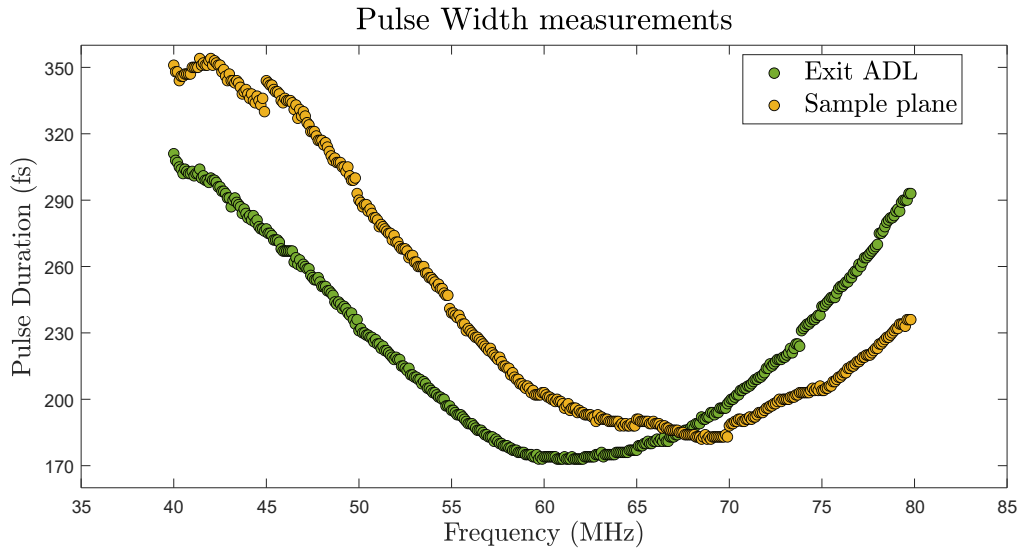

FIGURE 3.10 : Experimental pulse duration at the output of the delay line (green dot) and at the sample plane (yellow dot)

Output beam profile

We use a camera (Basler aca4024-29 μm) to look at the beam shape before and after the ADL. This is shown in Fig. 3.11. The beam size is about 1 mm with a slightly increased ellipticity as compared to the input beam. We attribute this elliptical shape to the folded mirror alignment.

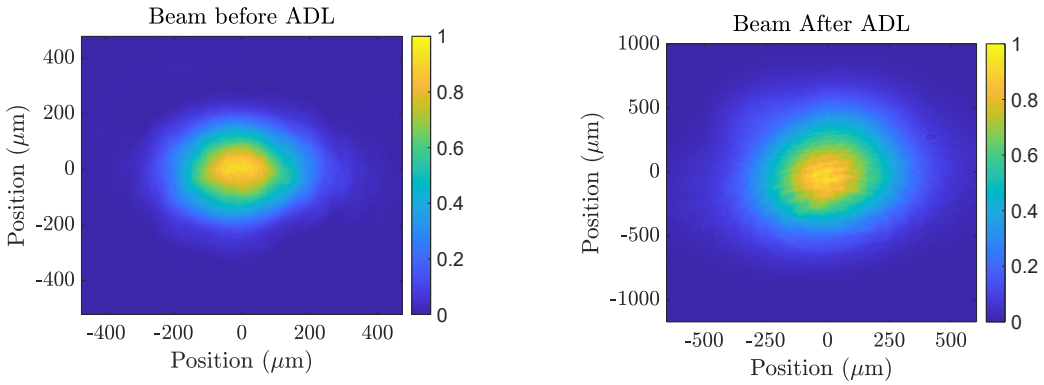

FIGURE 3.11 : Beam profile : a) Beam profile before ADL b) Beam profile after ADL

Beam walk off
To ensure that the output beam remains stationary while scanning across the ADL delay range, a camera was used to monitor the beam displacement. The displacement was found to be negligible.

Speed and Transmission
It takes 20 μs to upload a new delay into the AOD such as the ADL can operate at a maximum frequency of 50kHz. The overall transmission of our ADL is 15% mostly limited by the gratings efficiencies.

3.4.2 Synchronisation of driver and acquisition with Scanimage

Just as with the Dazzler, synchronizing the start of the scan and acquisition with the ADL is crucial. This is achieved using the ADL driver. Similar to the Dazzler, a trigger is used to initiate the ADL delay. The RF driver has a secondary 'scan trigger' that indicates when the RF frequency input changes to adjust the delay. Since the ADL operates slower than the dazzler, the LIA integration time is adjusted from 100 ns to 20 μs.

3.4.3 ADL for ISRS

This section explains the use of the ADL as a fast delay line in the setup. The delay is controlled by adjusting the input frequency to the RF generator of the AOD, allowing for arbitrary adjustments within the deflector's range. This introduces two operational schemes of interest : sequential scanning and agile delay scanning. The results of each scheme are presented in the following subsections.

3.4.3.1 Sequential scanning

We focus first on the 'sequential delay scanning' ability of the ADL over 50 ps. Fig. 3.12 a) shows the ISRS signal across 27 ps when the pump and probe pulses are focused on a bismuth germanate (BGO) crystal. We choose the 27 ps delay range from RF frequencies 60 and 77 MHz, where the pulse width is found to be closer to FTL. The ADL operates across 700 time points regularly spaced between 0 and 27 ps, each of them corresponding to a RF frequency f_{RF} fed to ADL in 20 μs. With these settings this high-resolution time trace is acquired in 14 ms. The LIA time constant is set to 20 μs to obtain the best signal-to-noise ratio (SNR). On Fig. 3.12 a) we see the strong signal at ~2 ps corresponding to the pump/probe overlap and the oscillatory time trace that develops from ~3 ps to 27 ps from the 89 cm^{-1} vibrational mode of BGO. The latter is better shown in the spectral domain (Fig. 3.12 b) where the Fourier transform of the ISRS signal performed across 25 ps (Fig. 3.12 a) is shown. The long-range delay achievable with the developed ADL enables a spectral resolution of 1.5 cm^{-1}, this is x8 better than what we previously achieved using the WB Dazzler in the previous section

using a single window. Performing the ISRS signal acquisition for each spatial point in a sample results in an ISRS image and Fig. 3.12 c) shows a 150x150 μm^2 image of the BGO edge. This high spectral resolution image (700 time points, 40 x 40 pixels) was acquired in 22 s.

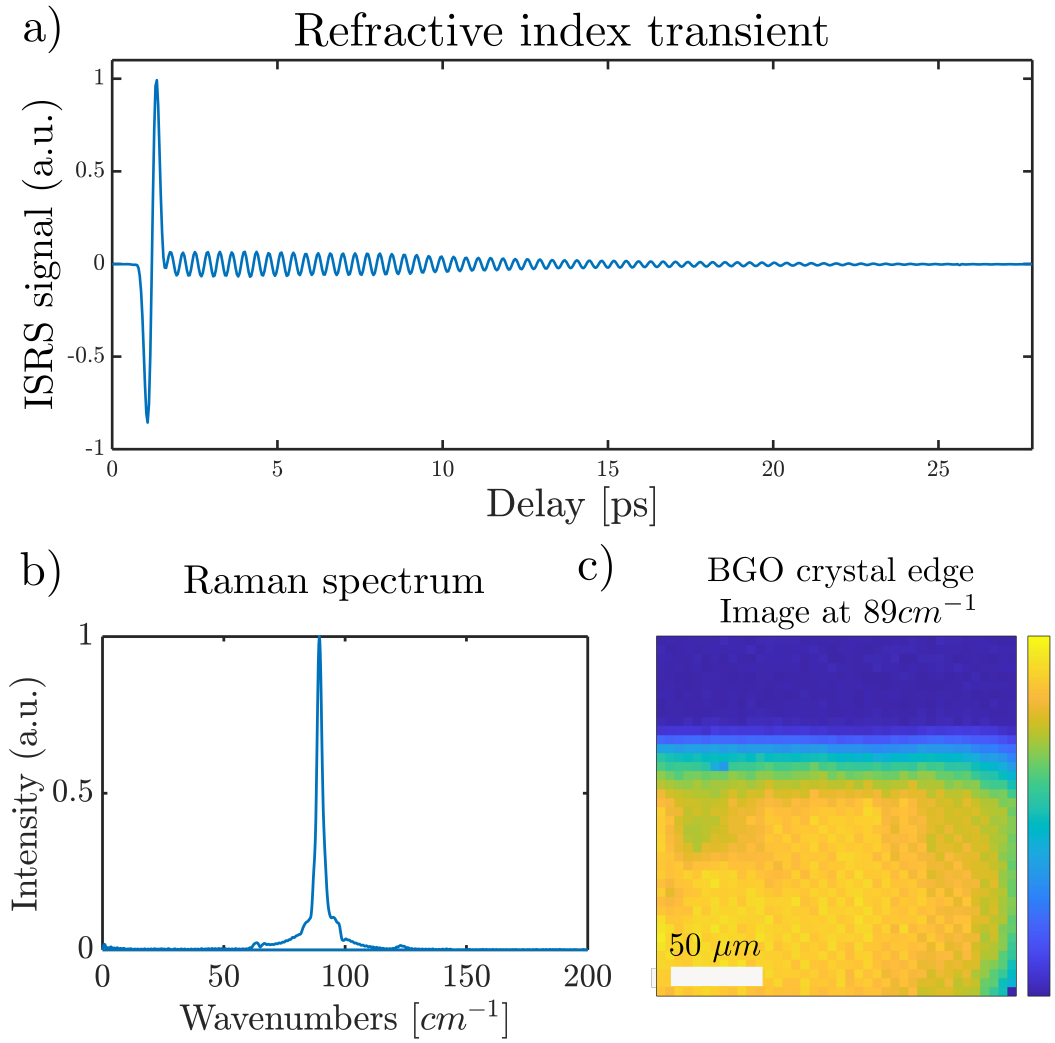

FIGURE 3.12 : (a) ISRS signal from a BGO crystal acquired during 27 ps with the ADL operating in 'sequential delay scanning' mode, (b) Fourier transform of the ISRS signal revealing the 89 cm^{-1}. BGO vibrational mode, (c) Image of the BGO crystal edge at 89 cm^{-1}. The image is taken with 10 mw probe and 38 mW pump on the sample plane.

For these experiments, it was verified that the ADL-induced chirp across the 50 ps delay range (Fig. 3.10) has a negligible effect on the retrieved Raman spectra. This was checked by generating certain peaks corresponding to the sample of interest in a simulation. The low Raman peaks of Carbamazepine (CBZ-DH) at 40, 75, and 111 cm^{-1}

were chosen. By chirping the probe pulse, any variation in the detection efficiency was observed. Considering the initial pulse width as 170 fs, and using the change in pulse duration with delay from Fig. 3.10, Fig. 3.13 shows the detection efficiency as the probe gets chirped. It was found that as the pulse becomes more chirped and the pulse width increases, the detection is less efficient towards the higher wavenumber. However, the peaks below 100 cm^{-1} remain as intense.

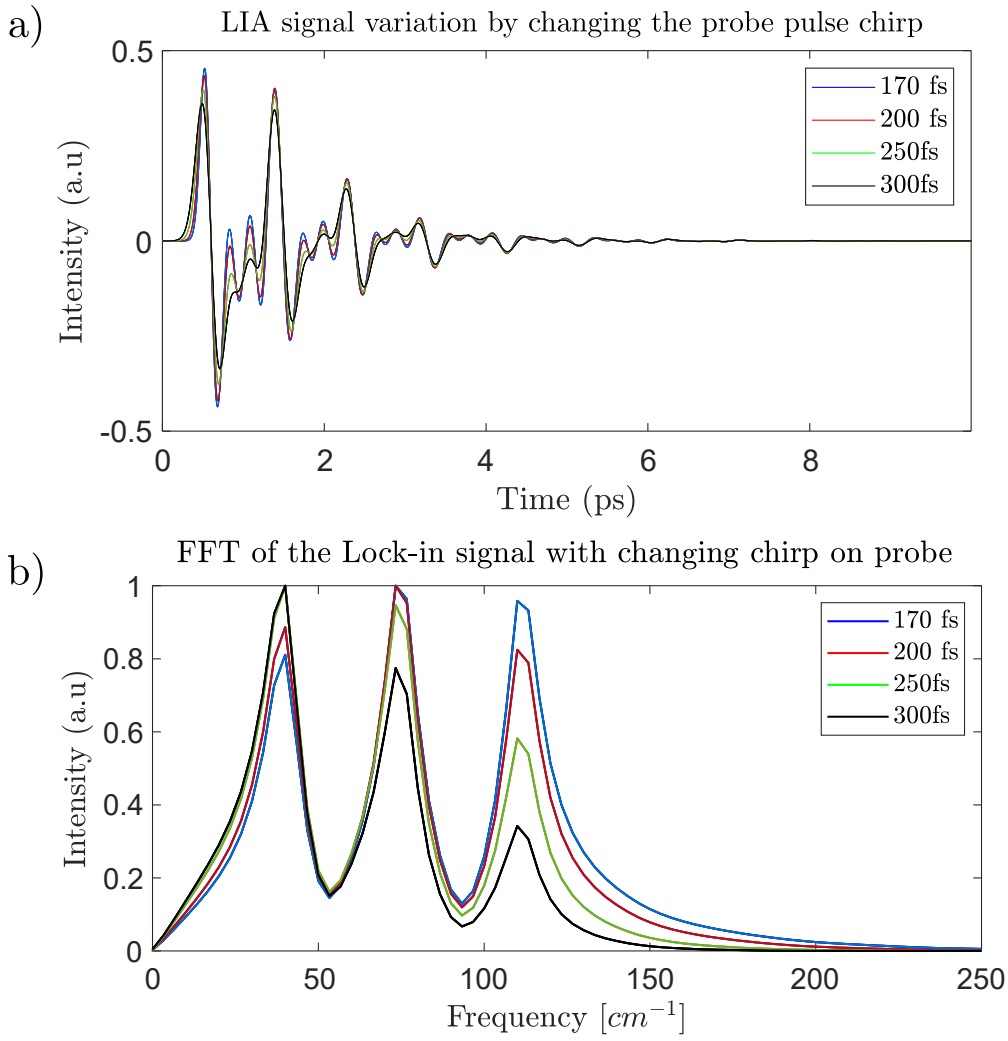

FIGURE 3.13 : (a) Signal from the LIA that corresponds to the time trace. As the probe gets wider it averages over higher frequency vibrations thus decreasing the sensitivity to detect these frequencies (b) Fourier transform of the LIA signal that shows the three peaks of CBZ-DH.

3.4.3.2 Agile delay scanning

The ADL can also operate in the 'agile delay scanning' mode to address different predefined delays arbitrarily arranged in time. A similar operation with any mechanical delay would be limited by inertia. Here we demonstrate how the ADL can be used to selectively detect and image chemical samples with ISRS. Fig. 3.14 a) shows the ISRS time signal of two chemical compounds acetaminophen (blue curve) and anthracene (red curve).

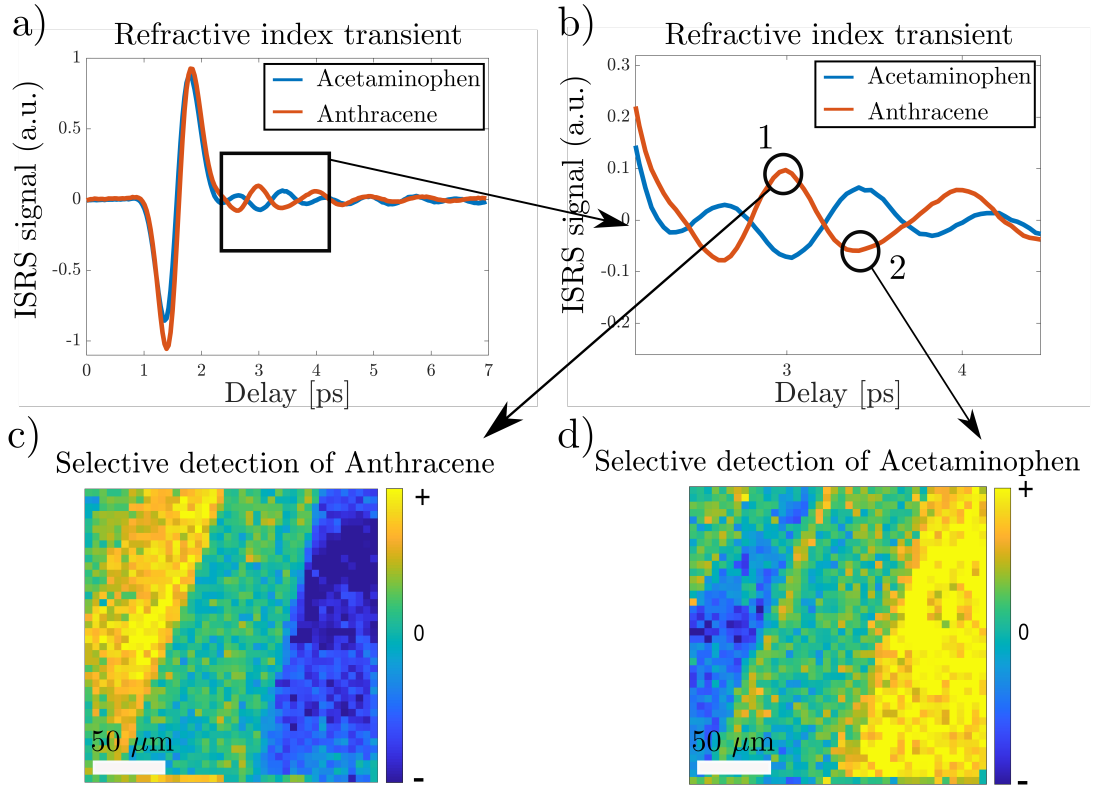

FIGURE 3.14 : a) ISRS time trace of acetaminophen (blue) and anthracene (red). b) Zoom-in from a) showing the two delay points that have opposite phases for the two chemical compounds (c) ISRS image at delay **1** showing the selective detection of anthracene d) ISRS image at delay **2** showing the selective detection of acetaminophen. The image is taken with 10 mw probe and 38 mW pump on the sample plane.

It is found that for two particular delays noted **1** and **2** in Fig. 3.14 b), the time traces are out of phase. At delay **1** (3 ps) the sign of the ISRS signal from anthracene is positive and that of acetaminophen is negative, and conversely at delay **2** (3.4 ps). By comparing the sign of the ISRS signal at delay **1** and **2** it is possible to differentiate between the two chemical species. This can be seen in figures 3.14 (c) and (d) that shows a 150x150 μm^2 image of a mixture between anthracene and acetaminophen

that can be distinguished when performing the ISRS image at delay **1** (anthracene, Fig. 3.14 c) and delay **2** (acetaminophen, Fig. 3.14 d). Considering that it takes 20 μs to jump from each delay scanned and that 10 points were averaged at the same delay to get this image, we have been able to image and distinguish the two chemical species with a pixel dwell time of 200 μs.

Besides providing faster images by the identification of critical delay points, the ADL can be used to perform time domain sub-sampling where it is expected that vibrational frequencies that are above the Nyquist sampling limit would be altered in the final Fourier retrieved spectrum. To explore this, we use the ADL to sub-sample the time domain trace of a mixed sample of acetaminophen and anthracene. The considered ISRS time trace is the spatial average of the ISRS time traces obtained in Fig. 3.14 (delay range of 7 ps). Figure 3.15 shows the retrieved Raman spectra obtained when the ADL explores the [2.5 ps, 7 ps] delay range with 150, 100, 50, and 25 probe delays regularly spaced.

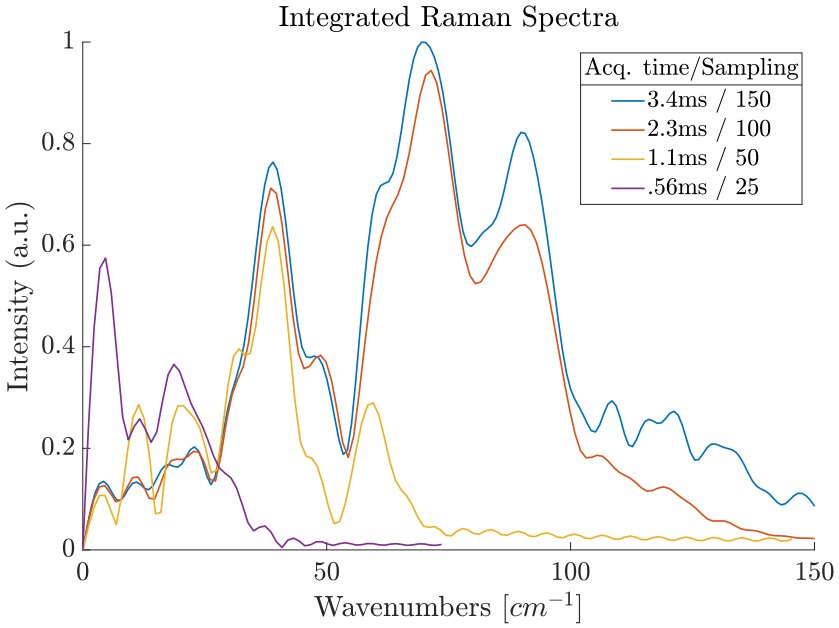

FIGURE 3.15 : Fourier retrieved Raman spectra from a mixture of anthracene and acetaminophen when the ADL samples 150, 100, 50 and 25 probe pulse delays in the [2.5 ps, 7 ps] delay range. The increased scanning speed is accompanied by a gradual loss of information as a consequence of Nyquist sub-sampling.

These ADL delay scan acquisitions are performed in 3.4 ms, 2.3 ms, 1.1 ms, and 0.56 ms, respectively. For 150 sampled delay points, all the anthracene (40 cm^{-1} and 70 cm^{-1}) and acetaminophen (90 cm^{-1}) peaks are well-defined. When the sampled delay points are reduced to 100, the peaks are still well-defined but the ADL scanning time is reduced by 30%. With 50 sampled delay points the ADL scanning time is reduced by 67% but the highest wavenumber peaks (70 cm^{-1} and 90 cm^{-1}) disappear as a

direct consequence of the Nyquist theorem. At 25 sampled delay points all information is lost and only peaks from aliasing remain.

3.4.4 Conclusion on ADL for ISRS

We have thus demonstrated an ADL that can scan 50ps of delay sequentially or in agile scanning delay mode. The agile mode, which allows arbitrary scanning of a set of predefined delays, differs from mechanical delay lines as it has no inertia, making it insensitive to short or long, positive or negative, delay jumps across the 50 ps range. The ADL can scan any set of predefined delays at 50 kHz, and we have demonstrated its usefulness in the context of impulsive stimulated Raman scattering (ISRS) to perform fast spectroscopy and imaging with a limited number of sampled time points. Taking advantage of the known ISRS time traces, we have been able to selectively image two chemical compounds with a pixel dwell time of 200 μs. We have also explored the effect of ISRS time trace sub-sampling to retrieve Raman spectra with increasing speed. The ADL can be improved in several ways. First, its modest throughput (15%) could be enhanced using >90% transmission holographic gratings. Second, a faster operation mode could be explored using chirped acoustic waves, where a few tens of ps delay could be scanned in only 20 μs. This ultra-fast delay scan is reminiscent of the acousto-optic programmable tunable filter (AOPDF) operation (Dazzler, Fastlite) but requires more advanced electronic control. The developed ADL opens also the road to compressive sensing [74] or any other time domain sub-sampling strategies for SNR, speed improvement, and data volume reduction [75].

4 Extending the detection range through ISRS

Summary

4.1 Outline of the Chapter 84
4.2 Experimental Setup 85
4.2.1 Laser source 85
4.2.2 Pump Arm 85
4.2.3 Probe Arm 85
4.2.4 Recombination and imaging Unit 85
4.2.5 Detection Unit and acquisition 87
4.3 Characterization of the pulses 87
4.3.1 Splitting into the pump and probe 87
4.3.2 Pulse Shaping the pump 87
4.3.3 Pulse Shaping the probe 90
4.3.4 Summary of the important parameters of the pump and probe . 90
4.4 Imaging using the extended detection range 94
4.4.1 Calibration crystals imaging 94
4.4.2 Pharmaceutical compounds 96
4.4.3 Solvents 96
4.5 Conclusion 99

4.1 Outline of the Chapter

In the previous chapter, the phenomenon of Impulsive Stimulated Raman Scattering (ISRS) was discussed as a method for detecting low Raman vibrational modes and imaging them. A video-rate imaging scheme sensitive to vibrations up to 160 cm^{-1} was demonstrated using two different types of delay lines : the WB Dazzler and the Agile Delay Line (ADL). Additionally, the increasing research interest in broadband Raman imaging techniques was explored. The ISRS technique described was constrained by the pump and probe pulse widths, limiting the ability to impulsively excite higher modes of interest. This limitation was previously discussed through simulations in Chapter 1. Extending the excitation range might seem achievable by increasing the laser bandwidth; however, higher bandwidths present challenges in shaping the pulse to achieve Fourier-transform-limited (FTL) pulses. This chapter focuses on implementing ISRS techniques capable of detecting beyond the low Raman threshold.

Pulses will be characterized along their path to ensure the shortest possible duration at the sample plane, and the results will be compared across various samples.

4.2 Experimental Setup

The Fig. 4.1 shows the experimental setup for ISRS with an extended detection range :

4.2.1 Laser source

The experimental setup begins with the Coherent VITARA laser, a broadband laser with an 80 MHz repetition rate and 1 W output power. The bandwidth of the VITARA can be tuned up to 100 nm, with a tunable central wavelength. For this experiment, a 90 nm bandwidth is utilized, centered at 790 nm, in contrast to the 10 nm bandwidth of the Ti :Saphire laser. The laser source is spectrally split into two parts, one serving as the pump and the other as the probe. A dichroic beam splitter (Multiphoton-LP-Beamsplitter HC 775 LP) is used for this purpose, with the red part of the spectrum acting as the probe and the blue part serving as the pump.

4.2.2 Pump Arm

The pump arm, depicted in red in the schematic, is reflected by the 775 LP dichroic beam-splitter and directed into a commercial pulse compressor from Thorlabs, known as the Femtosecond Pulse Compressor (FSPC). This device compensates for pulse broadening by pre-compensating with negative dispersion. It functions similarly to a prism compressor and, at 790 nm, can add negative dispersion of up to $-12,500$ fs^2, with a transmission efficiency of 85%. The FSPC serves as the pulse shaper in this setup. After shaping, the pump arm is focused onto an acousto-optic modulator (AOM) modulated at 12 MHz, re-collimated by a second lens, and passed onto the recombination beam splitter.

4.2.3 Probe Arm

The probe beam, shown in yellow in the schematic, is transmitted through the dichroic beam-splitter to the fast delay line and pulse shaper, the Dazzler. The HR Dazzler is employed due to its superior pulse shaping capabilities, which are crucial for larger bandwidths, although it has lower throughput. A mechanical delay line is incorporated to achieve temporal overlap between the pump and probe pulses.

4.2.4 Recombination and imaging Unit

The pump and probe beams are recombined using a similar dichroic mirror initially used for their separation. The recombined beam is expanded with a telescope composed of 150 mm and 200 mm lenses, providing 1.5x magnification. The beam is

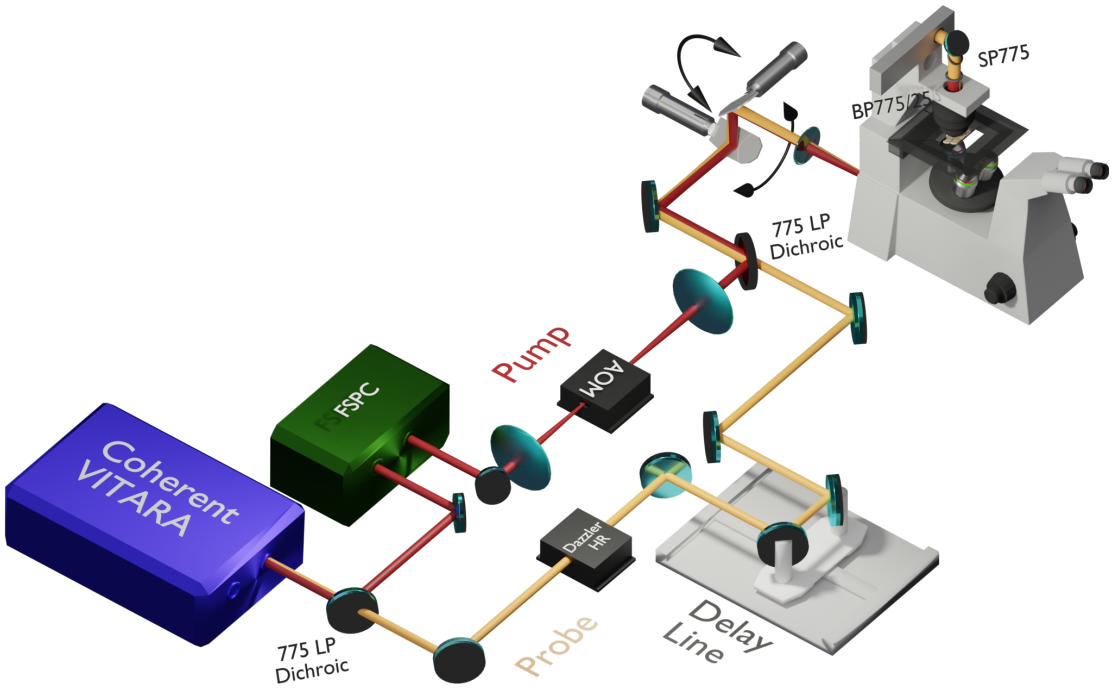

FIGURE 4.1 : Schematic of the experimental setup for ISRS. The 775 LP, SP775, and BP775/25 are the long pass, short pass, and bandpass filters used, respectively. FSPC refers to the femtosecond prism compressor from Thorlabs that is used for pulse shaping. AOM stands for the acousto-optic modulator, which is used to modulate the pump beam.

then directed into the microscope (Eclipse Ti-U, Nikon, Japan) using galvanometric scanning mirrors. The scan mirrors are conjugated to the back focal plane of the microscope via a 3x telescope. The beams are focused and collected using 20x/0.75 NA air objectives (CFI Plan Apo Lambda 20X, Nikon).

4.2.5 Detection Unit and acquisition

As in previous experiments, the pump pulse is blocked using an SP755 (Short Pass) filter, and a BP775/25 (Band pass) filter is employed to detect the spectral shift. The rest of the acquisition setup remains identical to the previous configuration. ScanImage software is utilized, with minor adjustments to accommodate the change in the Dazzler type used for ISRS spectra acquisition. The Dazzler RF generator is synchronized to trigger the acoustic wave and initiate the acquisition process.

4.3 Characterization of the pulses

As mentioned earlier, it is crucial to have well-shaped Fourier-transform-limited (FTL) pulses at the sample plane. Ensuring that the complete spectra is preserved without any truncation is critical for optimal performance. Precise measurement of the temporal and spectral widths of the pump and probe pulses is necessary to define the excitation and detection bandwidth limits of the ISRS imaging system.

4.3.1 Splitting into the pump and probe

As discussed in Chapter 1, achieving short pulse durations for both the pump and probe is crucial— the pump for impulsive excitation and the probe for accurately capturing the transient refractive index. To accomplish this, the beam is split so that both the pump and probe have nearly identical bandwidths of 45 nm that are derived from the FWHM 90 nm bandwidth pulse centered at 790 nm. The spectra of both pump and probe are shown in Fig. 4.2

4.3.2 Pulse Shaping the pump

For the pump, the FSPC is utilized to introduce negative dispersion. The group delay dispersion (GDD), which describes how different frequency components of a pulse experience varying delays as they pass through a dispersive medium, is controlled by a knob on the FSPC. This knob displaces one prism relative to the other, allowing for precise adjustment of GDD. The GDD is wavelength-dependent, with higher wavelengths allowing for less compensation. For a wavelength around 800 nm, the FSPC can provide negative dispersion compensation up to $-12,500$ fs^2, which is sufficient to counteract pulse broadening. Adjusting the prism distance beyond this point will start truncating the spectrum. Fig. 4.3 illustrates how the spectrum changes as we

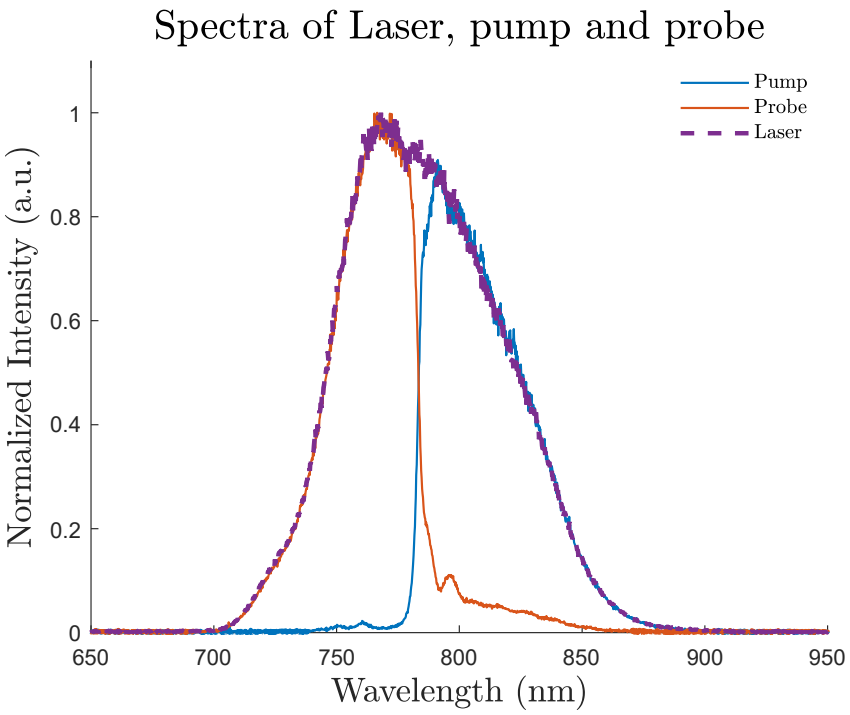

FIGURE 4.2 : The figure shows the spectra of a) the preset of the Vitara laser (Dotted purple lines) of 90 nm bandwidth centered at 790 nm. b) the pump (blue) and probe (orange) pulse spectra are shown as solid lines that have been split with the 775 dichroic beam splitter

adjust the prism distance in the FSPC beyond its maximum dispersion compensation capability.

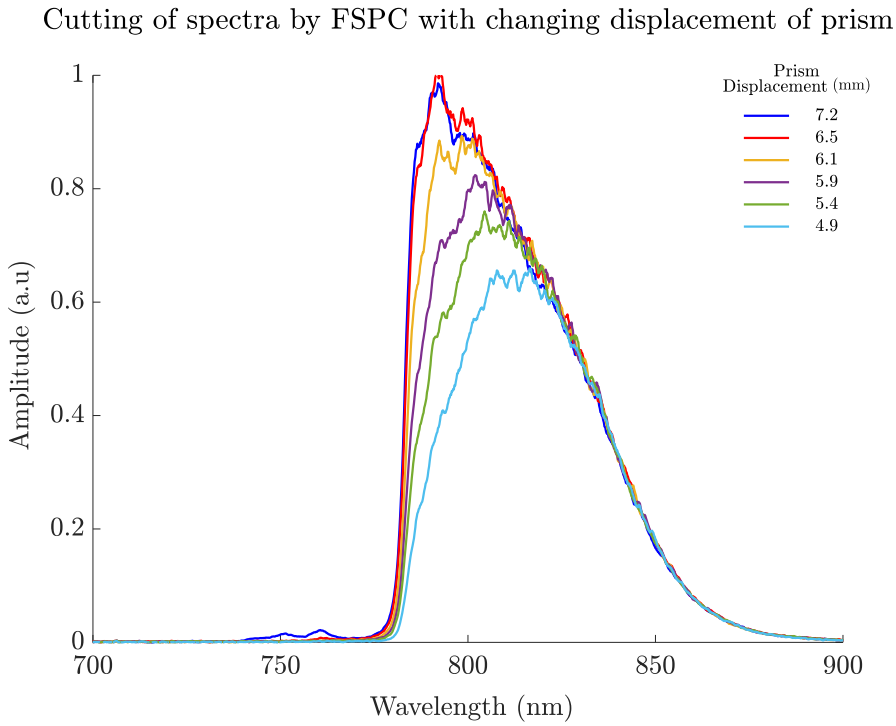

FIGURE 4.3 : The figure illustrates the output spectra of the FSPC for varying prism displacements. It demonstrates that with a large incoming bandwidth, the FSPC is unable to fully compensate for chirp, leading to spectral truncation. The bandwidth is cut from 40 nm to approximately 25 nm at the different prism displacements.

To determine the optimal prism displacement that minimizes pulse duration, the pulse width at the sample plane is measured using an autocorrelator (APE CARPE), while ensuring that the spectrum is not excessively truncated at the FSPC output. This process is relatively straightforward, as there exists a point where the FSPC may cut part of the spectrum while still providing maximum dispersion compensation for the available spectrum. The determined prism displacement is subsequently used for the experiments.

A notable limitation of prism compressors is their inability to correct for higher-order dispersion, such as third-order dispersion. This limitation becomes apparent in the pulse profile observed through the autocorrelator, where side wings appear due to third-order dispersion effects (Fig. 4.6). Although this situation is not ideal, the experiments will proceed with this setup.

4.3.3 Pulse Shaping the probe

The HR Dazzler is employed for pulse compression for the probe. This device can compensate for both second-order and higher-order dispersions that may arise as the beam travels through it. Although the HR Dazzler needs to counteract the dispersion originating from its own material, which is approximately 12,000 fs^2, it can still compensate for an additional chirp of up to 15,000 fs^2 for a bandwidth of 50 nm.

Care must be taken to avoid overfilling the Dazzler. "Overfilling" occurs when the laser input bandwidth is too high, necessitating additional frequency components in the acoustic wave to phase match and correct for each frequency within the pulse's bandwidth. This results in a long acoustic waveform that can occupy the entire length of the Dazzler scan. Consequently, the pulses at the ends of the acoustic wave may be poorly shaped due to the absence of necessary frequency components for effective phase matching.

An exaggerated example of this phenomenon is illustrated in the shape of the acoustic wave shown in the Dazzler application window (Fig. 4.4a) and b)). The black shaded area represents the Dazzler crystal, while the purple shaded section indicates the limit of the delay, which is evident on the x-axis corresponding to 8.6 ps. Beyond this point, the acoustic wave begins to diminish. Additionally, the application displays the simulated output spectra for the acoustic waveform that has been programmed (Fig. 4.4 c) and d)). If the output deviates from the ideal scenario, it is highlighted in red.

To investigate overfilling (Fig. 4.4 b) and d)), the input bandwidth is increased to 100 nm, and the negative chirp is adjusted to -25,000 fs^2. This adjustment reveals that the Dazzler also truncates a portion of the spectrum due to overfilling, resulting in poor pulse shaping. For a bandwidth close to 45 nm, the HR dazzler can very easily compensate for the chirp without overfilling the dazzler. It is interesting to note here that with the WB dazzler, it would have been difficult to manage this bandwidth as the acoustic wave would have filled the Dazzler with its smaller delay range of 4.5 ps compared to 8.6 ps of the HR.

Similar to the pump, the pulse duration for the probe beam can be optimized by adjusting the dials on the Dazzler to introduce additional chirp, with results verified using the CARPE at the sample plane. It is important to manipulate the second, third, and fourth-order dispersions to achieve the shortest possible pulse width at the sample plane. Through this optimization process, a pulse duration as short as 45 fs can be attained.

4.3.4 Summary of the important parameters of the pump and probe

The excitation limit of the setup can be estimated by measuring the pulse width at the sample plane and evaluating the bandwidth over which excitation can occur. First, the spectra at the sample plane are checked after recombining the pump and probe to determine the available bandwidth at the output, as shown in Fig. 4.5. The full width at

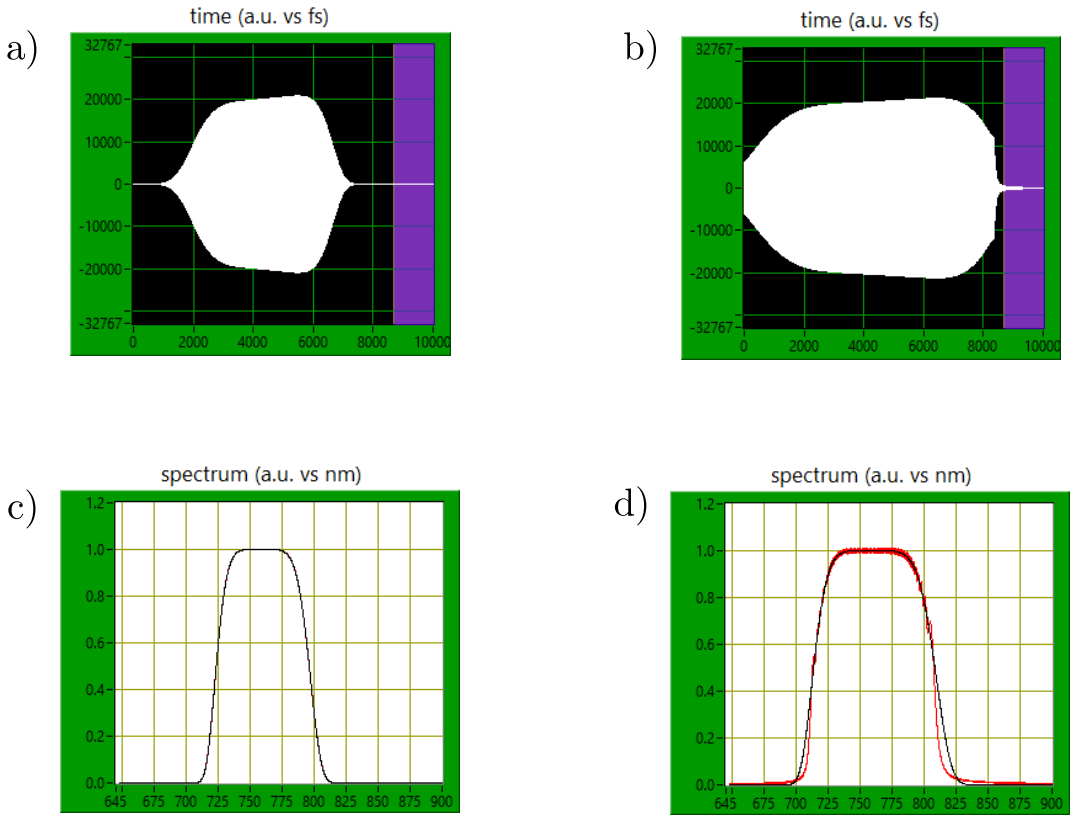

FIGURE 4.4 : These figures are derived from the Dazzler application, which visualizes the acoustic wave shape within the crystal and the corresponding simulated output. The purple shaded region denotes the end of the crystal, while the black shaded region represents the interior. Figures a) and b) depict the acoustic wave shape along the length of the crystal for two conditions : a) a probe pulse with a 50 nm bandwidth and chirp compensation of -19200 fs^2, and b) a very high bandwidth (100 nm) pulse with increased chirp compensation upto -25,000 fs^2. In the second scenario, the acoustic wave cannot be fully generated before it begins to decay. Figures c) and d) illustrate the simulated output; the first case shows that the bandwidth remains intact, while the second case illustrates, with the red curve, how the output beam is truncated due to the high bandwidth necessitating greater dispersion compensation.

half maximum (FWHM) is calculated from the graphs, yielding values of 38 nm for the pump and 34 nm for the probe at the sample plane, despite an initial split of 45 nm in each arm. Experimentally, it is observed that a few nanometers are lost at the output of the Dazzler and further losses occur through the recombination beam splitter for the probe beam. For the pump, the majority of the bandwidth is lost at the output of the FSPC. The pulse widths of the pump and probe beams at the sample plane, crucial

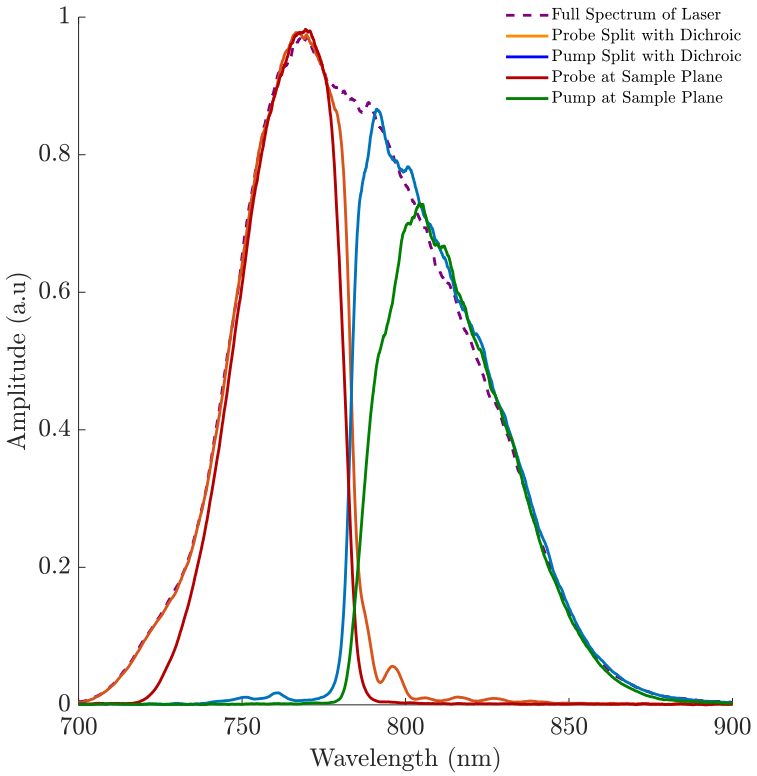

FIGURE 4.5 : The figure shows the spectra we get at the sample plane compared to the full laser bandwidth, the split pump and the split probe. We see the loss in bandwidth at the end of the sample plane

for excitation and detection, are evaluated and plotted in Fig. 4.6. The impact of poor third-order compression is evident from the presence of side lobes in the Gaussian fit of the pump pulse, highlighting the effects of uncompensated higher-order dispersion. The minimum pulse widths obtained are 45 fs for the probe and 42 fs for the pump, respectively. The FTL pulse width for a gaussian beam of 34 and 38 nm should be theoretically 28 and 25 fs. However, we do not see this. It could be that the pulses are not Fourier transform limited and these are the best compression we can do for this bandwidth. However, we will see in the result how we can detect peaks up to even 550 cm^{-1} that corresponds to an FTL limited bandwidth of $\approx$ 35 nm.

Table 4.1 summarizes the key properties of the pump and probe pulses we have been able to achieve

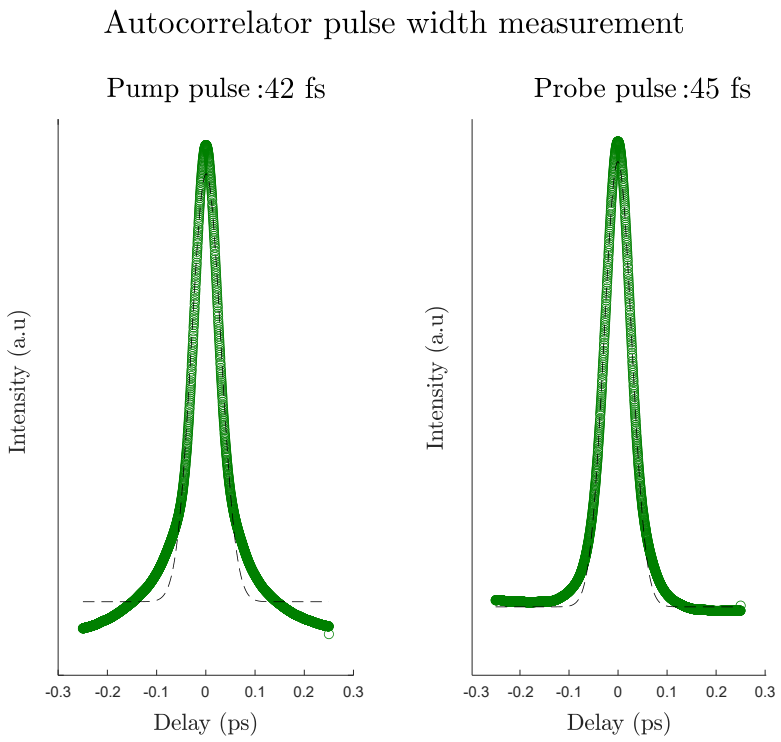

FIGURE 4.6 : The figure shows the pulse width measurement with the CARPE autocorrelator that is placed at the sample plane. As seen from the fit, for the case of the pump beam we see the sidebands that arise from poor pulse shaping due to the third order dispersions. This however is not an issue when we use a Dazzler to pulse shape the probe. In the sample plane, we get 42 fs pulses for the pump and 45 fs pulse for the probe.

Property	**Pump**	**Probe**
Power at Sample Plane	50 mW	50 mW
Pulse Width at Sample Plane	42 fs	45 fs
Bandwidth	38 nm	34 nm
Centre wavelength	809 nm	768 nm

TABLEAU 4.1 : Comparison of pump and probe properties

4.4 Imaging using the extended detection range

The following section will present the different samples used to study the detection range and capabilities of the setup built. The Scanimage software, developed in Chapter 3, will be used for this purpose. The synchronization of the different electronics remains unchanged. The primary difference lies in the use of the HR Dazzler for this scheme, which scans 8 ps in 30 μs. The number of time points acquired, N_t, is given by :

$$N_t = \frac{t_a}{\tau_c} \approx 350 \tag{4.1}$$

where t_a is the time for the acoustic wave to travel through the crystal (32 μs), and τ_c is the integration time of the LIA (100 ns). An additional number of acquisition points is added to ensure that the Dazzler does not receive the signal to start generating an acoustic wave before it has fully traveled through the crystal.

4.4.1 Calibration crystals imaging

The calibration sample used in this study is the BGO crystal, along with Potassium Titanyl Phosphate (KTP). Both BGO and KTP are transparent crystals that cannot be distinguished through a simple transmission image. In earlier setups, with a limited detection bandwidth of 160 cm^{-1}, differentiating between the two crystals based on their spectra was challenging, as both exhibit peaks around 89 cm^{-1}.

Fig. 4.7 presents results obtained with the extended detection range setup. Fig. 4.7(a) displays the time trace of 8.6 ps acquired with the HR Dazzler, showing both BGO and KTP crystals in the field of view (FOV). Notably, the time trace reveals higher frequency vibrational modes, in contrast to the single peak and single frequency oscillation seen in Fig. 3.7 and Fig. 3.12 in Chapter 3. Fig. 4.7(b) provides the spectra obtained through the Fourier transform of the integrated time trace, identifying several peaks up to 450 cm^{-1} for both BGO and KTP, which facilitates selective imaging of each crystal. Fig. 4.7(c) illustrates the transmission image, along with the corresponding hyperspectral images resolved at various Raman peaks.

The hyperspectral images show that the intensity of the peaks for each sample can be clearly distinguished. For instance, the hyperspectral image resolved at 89 cm^{-1}, which corresponds to peaks from both KTP and BGO, indicates that the BGO peak is stronger than that of KTP. However, when examining the hyperspectral image resolved around 215 cm^{-1}, greater contrast is observed for the KTP crystal, as the peak at this wavenumber exhibits a stronger intensity for the KTP sample. These observations align with previous findings in the literature [76, 77]. To compare with the reference spectra from various sources, for BGO crystals we can find peaks at 89 cm^{-1}, 201 cm^{-1} and 400 cm^{-1} comparing to the reference peaks of 86 cm^{-1}, 197 cm^{-1} and 396 cm^{-1} [78]. For KTP crystals, we find peaks at 89 cm^{-1}, 215 cm^{-1} and 266 cm^{-1} comparing to the reference peaks of 86.5 cm^{-1}, 212 cm^{-1} and 267 cm^{-1} [79].

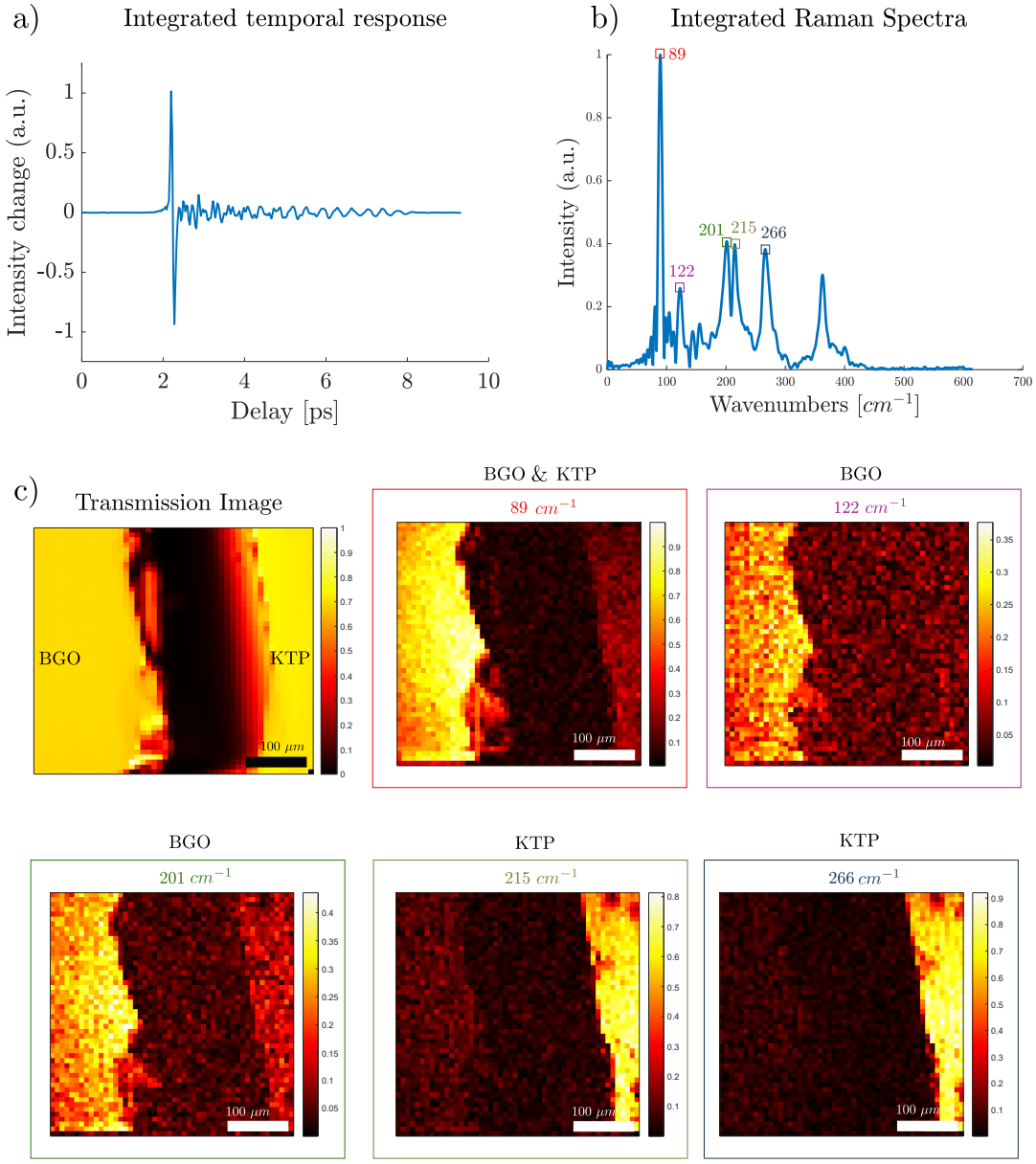

FIGURE 4.7 : The figures above show images of BGO and KTP taken with a field of view (FOV) of 400 μm at a resolution of 50 × 50 pixels. Fig. 4.7 (a) displays the integrated time trace over the image, while Fig. 4.7 (b) presents the Fourier transform revealing the integrated Raman spectra over the image. Fig. 4.7 (c) includes the transmission image, with BGO on the left and KTP on the right, both appearing identical. The adjacent hyperspectral images highlight the distinct vibrational modes of the two materials, allowing for clear identification of BGO and KTP.

4.4.2 Pharmaceutical compounds

This section demonstrates how the extended detection capabilities allow for the observation of higher vibrational frequencies in pharmaceutical compounds, such as anthracene, which were studied in the previous chapter. Fig. 4.8 presents an image of a field of view (FOV) containing both anthracene and acetaminophen.

A 50 × 50 image was captured over a 50 μm FOV, with pump and probe powers around 40 mW at the sample plane. The FOV mainly contains anthracene and some acetaminophen at the top right corner which is out of focus due to their varying thickness. Higher-order vibrational frequencies, particularly around 120 cm^{-1}, confirm the presence of anthracene. The low Raman peak at 56 cm^{-1} of acetaminophen is circled in the spectrum and is very small. From the hyperspectral images of anthracene in Fig. 4.8 c), only the peaks at 38 cm^{-1} and 120 cm^{-1} give a good contrast in the image. This is because when we get the hyperspectral image from the individual pixels, the weaker peaks are buried in noise.

4.4.3 Solvents

The extension of the detection range enabled imaging of both crystalline compounds and various solvents. Raman spectroscopy has historically been used to extract extensive information from liquids due to its rapid and non-destructive nature. In pharmaceuticals, it plays a crucial role in studying drug dissolution [80], performing biochemical analyses of blood or urine for early disease detection [81], and identifying contaminants, including heavy metal detection in water quality testing [82].

Typically, most liquid-phase compounds do not exhibit Raman spectra below 160 cm^{-1}. However, with the extended detection range, Raman peaks from several commonly used solvents were successfully identified. The obtained spectra for the studied solvents, along with their chemical structures, are shown in Fig. 4.9.

The peaks associated with the solvents were identified based on the NIST database and a literature review, which provide insights into the vibrations corresponding to each peak. For instance, in the case of chloroform, the peak at 261 cm^{-1} is attributed to degenerate C-Cl_3 bending vibrations, while the peak at 363 cm^{-1} corresponds to symmetric C-Cl_3 bending vibrations. The term "degenerate" indicates that the bending angle is the same but occurs in different directions, corresponding to the same energy level. In contrast, the "symmetric" case describes bending that happens in unison.

For acetonitrile, the observed peak corresponds to the C-CN bend at approximately 380 cm^{-1}. These data points are taken from the NIST database and are considered reliable.

For DMSO and n-heptane, the spectral data are not available in public databases. However, literature reviews provide valuable trends. The increasing order of the peaks for DMSO corresponds to the following vibrations : C-S-C bending vibrations at 302 cm^{-1}, C-S-O antisymmetric bend at 337 cm^{-1}, C-S-O symmetric bending at 384 cm^{-1} [83, 84]. The peak at 570 cannot be found in any literature. Further analysis is needed to

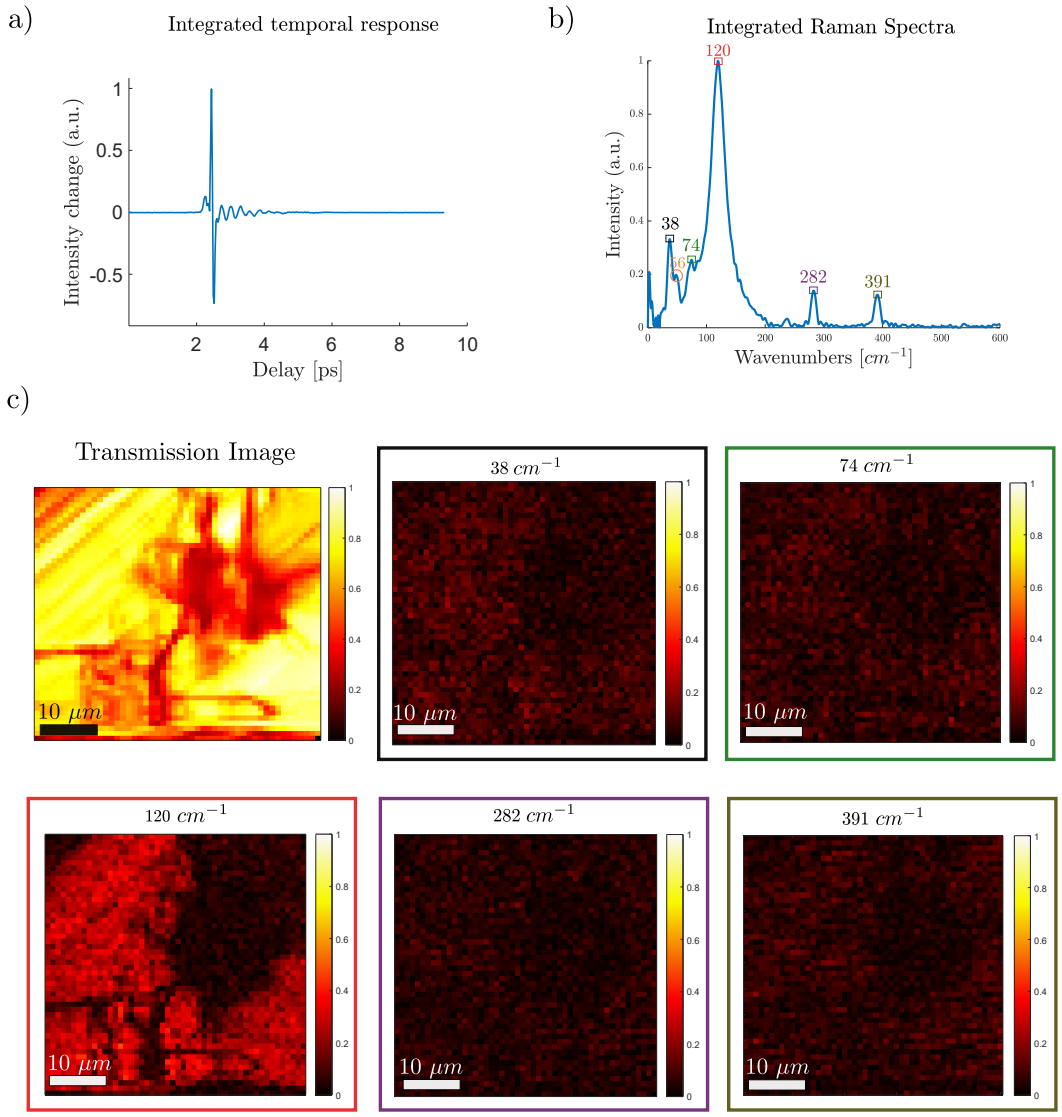

FIGURE 4.8 : The figures above show images of anthracene and acetaminophen, captured with a field of view (FOV) of 50 μm at a resolution of 50 × 50 pixels. Fig. 4.8(a) presents the averaged time trace over the image, while Fig. 4.8(b) displays the Fourier transform revealing the integrated Raman spectra over the image. The peaks marked with square are of anthracene, and the peak circled is of acetaminophen. Fig. 4.8(c) includes the transmission image. The adjacent hyperspectral images are resolved for the peaks of anthracene, highlighting the strong vibrational mode at 120 cm^{-1} followed by a noisier image at 38 cm^{-1}. All other hyperspectral images are noisy as the individual peaks are buried in noise for each pixel

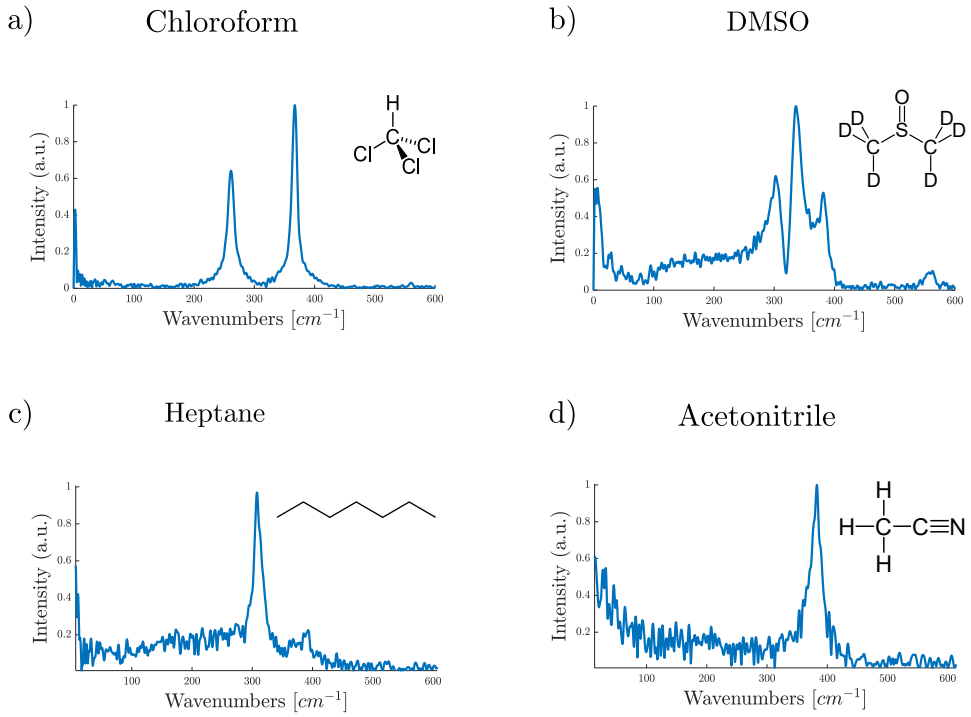

FIGURE 4.9 : The figure shows the spectra retrieved from four different solvents : Chloroform, Dimethyl sulfoxide (DMSO), Heptane and Acetonitrile respectively

justify it. Similarly, the peaks for n-heptane can be addressed, due to the C-C aliphatic chain from various Raman band correlation tables.

To demonstrate imaging in liquid environments, a mixture of two immiscible liquids, chloroform and water, was prepared. A quartz cuvette with a 1 mm path length was filled with the liquids and vigorously shaken to form water droplets suspended in chloroform. The resulting spectra clearly show strong peaks for chloroform at 261 and 363 cm^{-1}, allowing for resolution of images at these wavenumbers. The results are shown in Fig. 4.10. In this case, we have employed frequency domain filtering to mitigate periodic noise in the image by performing a 2D Fast Fourier Transform (FFT), where the periodic noise manifests as distinct high-frequency components. Circular masks were manually applied to the FFT image at specific regions to suppress these noise components. The filtered image was then reconstructed using an inverse FFT, effectively reducing the noise while preserving important image details.

4.5 Conclusion

In this chapter, the detection range of the existing ISRS setup has been significantly enhanced to encompass frequencies up to 550 cm^{-1}, achieving an approximately 3.5-fold improvement in detection bandwidth. This advancement was made possible by employing a broadband laser with a 90 nm bandwidth and effectively splitting this bandwidth between the pump and probe beams. The chapter has thoroughly addressed the spectral losses encountered during various stages of the pulse compression process, highlighting the limitations inherent in the current methodology. The critical role of utilizing an HR Dazzler capable of introducing larger delays was also emphasized, allowing for better precompensation of chirp across the broader bandwidth.

Consequently, the ISRS setup has been optimized to deliver up to 50 mW at the sample plane for both the pump and probe, resulting in pulse bandwidths of 38 nm and 34 nm, respectively. The extended detection capabilities were demonstrated through imaging various samples, initially showcasing calibration crystals where multiple peaks were observed, contrasting sharply with the single peak detected previously. Additionally, the enhanced detection range was validated with pharmaceutical samples, including anthracene and acetaminophen.

Moreover, the ability to image liquid-phase samples has been successfully demonstrated, particularly with a chloroform-water mixture, which was rendered immiscible by forming droplets. This significant extension of the detection range not only broadens the scope of Raman spectroscopy applications but also paves the way for more comprehensive analyses in various fields, including pharmaceuticals and biochemical research.

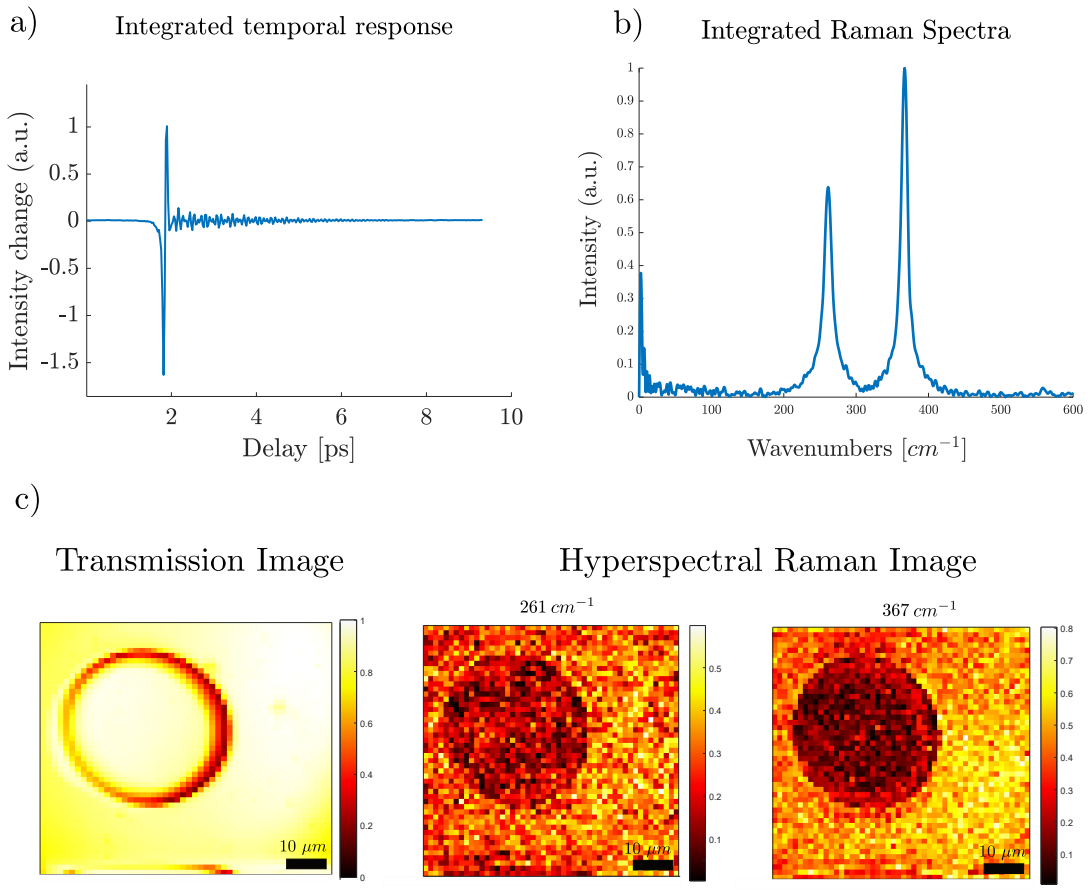

FIGURE 4.10 : The set of figures above presents images captured with a cuvette containing a mixture of chloroform and water, covering a field of view (FOV) of 400 μm with a resolution of 50 × 49 pixels. a) Displays the integrated spectrum obtained by averaging all time traces from the 50 × 49 pixels. b) Shows the Fourier transform of the time trace, resulting in the integrated Raman spectrum. c) Presents the retrieved images, with the first image depicting the transmission image. In this image, the bubble of water is surrounded by chloroform, and they appear identical. The adjacent images are hyperspectral images resolved around different Raman peaks, clearly illustrating the bubble of water in chloroform.

5 Conclusions and Future perspectives

Summary

5.1 Conclusion 101
5.2 Possible improvements 102
5.2.1 Excitation range 102
5.2.2 Detection range 104
5.2.3 Sensitivity and SNR 106
5.3 Future perspectives 107

5.1 Conclusion

This thesis has focused on the development and enhancement of Impulsive Stimulated Raman Scattering (ISRS) imaging, particularly through the integration of acousto-optic delay lines. The study began with an introduction to Raman scattering, with special emphasis on coherent Raman scattering phenomena and their applications in imaging. The classical picture of Raman scattering was explored, highlighting how nonlinear polarization generates oscillating frequencies, giving rise to coherent Raman effects. The importance of acquiring broadband spectra for faster imaging and richer data was emphasized, which led to the introduction of ISRS, especially for low Raman shifts. Impulsive excitation was shown to be crucial in this technique, as it creates a transient refractive index that can be examined by fast scanning of the probe pulse over time. The spectral shift of the probe beam was also discussed as a key method for tracking the transient refractive index. Furthermore, it was demonstrated how altering the pulse width of the probe beam enables a transition from the frequency domain view of Coherent Anti-Stokes Raman Scattering (CARS) to a time-domain approach, illustrated through simulations.

Following this, we explored the use of acousto-optics for control of pulse dispersion and delay. We have used two different types of delay lines : the Acousto-Optic Programmable Dispersive Filter (AOPDF) and the Agile Delay Line (ADL). We examined the advantages and disadvantages of each in terms of pulse shaping, speed, and delay range, providing a rationale for selecting the appropriate delay line based on the specific imaging requirements. It was concluded that, for the AOPDF, the HR variant is preferred due to its superior pulse shaping and higher delay range, despite lower transmission efficiency and a slightly slower trigger rate compared to the WB. When a

larger delay range is required, the ADL proves ideal, though it is constrained by the 10 nm input bandwidth of the laser for which it is designed.

The implementation of a low Raman detection setup with a detection range up to 160 cm^{-1} was then discussed, utilizing both the AOPDF and ADL. A detailed explanation of data acquisition using ScanImage, a MATLAB-based imaging interface, was provided, emphasizing the importance of proper synchronization for accurate data collection and processing. Images of various samples taken at video rate (7 Hz) using the Dazzler were showcased. The same setup was adapted for the ADL, enabling selective detection once the time trace of a specific compound was known, and allowing the study of long-lasting transient refractive indices in calibration samples such as BGO.

In the final part of the thesis, the detection range of the setup was extended by a factor of 3.5, reaching up to 550 cm^{-1}, through the implementation of an ISRS scheme utilizing shorter pulses and improved pulse shaping. This enhancement was achieved by employing a single laser source with a 90 nm bandwidth, which was then split into pump and probe beams. Extensive characterization of the spectrum and pulse width of the two beams was conducted at the sample plane to ensure the shortest possible pulse for efficient excitation across the entire bandwidth. This has allowed us to extend the sensitivity of our setup to liquid samples.

To conclude, this thesis has attempted to bridge the gap that exists between the high-frequency coherent Raman techniques in the frequency domain and the low-frequency approaches in the time domain through a combination of fast scanning microscopy. The integration of advanced acousto-optic delay lines and the optimization of experimental setups have enhanced the capabilities of ISRS imaging. These developments have not only improved the detection range and sensitivity of the system but have also enabled more efficient data acquisition and processing. Ultimately, the advancements presented in this work pave the way for more detailed and rapid imaging applications, enhancing the potential for ISRS in various fields, including biological imaging and material characterization.

Fig. 5.1 provides a comprehensive overview of the advancements in improving the ISRS technique throughout this thesis.

5.2 Possible improvements

Although significant improvements have been made to the setup in terms of speed, detection range, and resolution, the actual potential of the system regarding excitation and detection efficiency remains to be fully realized.

5.2.1 Excitation range

The current setup employs a laser capable of producing short pulses with a 100 nm bandwidth; however, by splitting this laser into two beams—the pump and probe—each arm achieves a maximum bandwidth of only about 35 nm. As detai-

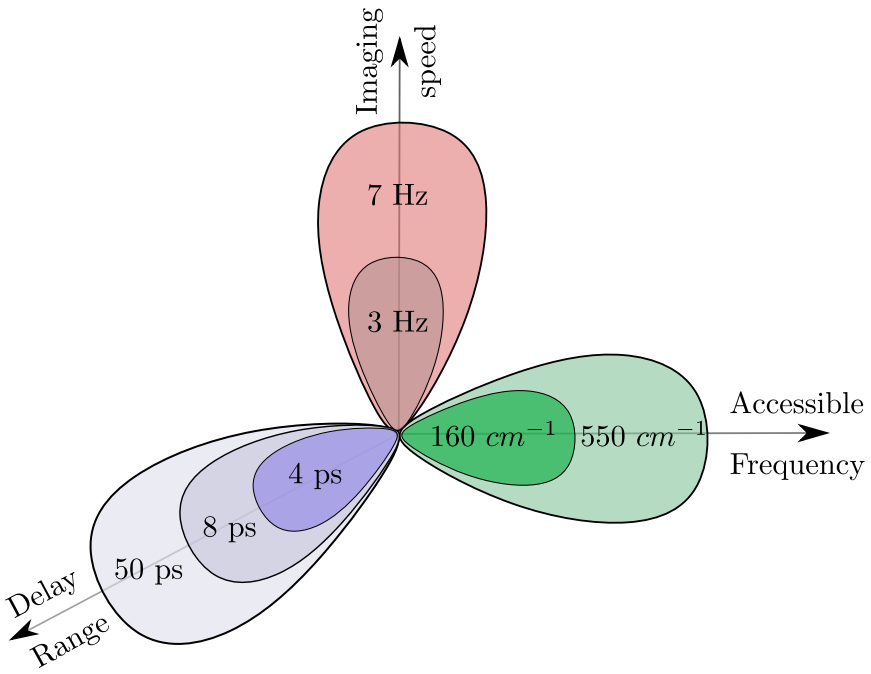

FIGURE 5.1 : This figure presents a pictorial summary of the key improvements made to the ISRS technique in three main areas : i) Imaging speed has been enhanced from 3 Hz to 7 Hz by transitioning from Labview to Scanimage; ii) The accessible frequency range has been expanded more than threefold by utilizing a higher bandwidth laser and implementing better pulse control; iii) The delay range, and consequently the achievable spectral resolution in a single scan, has been significantly extended from 4 ps to 8 ps by shifting from the WB to HR Dazzler, and further to 50 ps with the introduction of the ADL.

led in Chapter 4, this is the highest bandwidth we can manage with the existing commercial pulse shaper.

One possible improvement involves using advanced pulse shaping techniques to better manage higher-order dispersions in addition to second-order dispersion. This could be achieved through the use of grating compressors, spatial light modulators (SLMs) [85], or multilayer chirped mirrors [86]. Despite these enhancements, even with optimal compression and a broader 45 nm bandwidth for both pump and probe, the maximum excitation remains limited to approximately 600 cm^{-1}.

Another option is to use the full bandwidth of the pump and probe beams, followed by polarization rejection to filter out the pump. However, this approach has two major limitations. Firstly, it prevents the study of polarization dependence in the Raman spectra. Secondly, for highly scattering samples—unlike calibration samples or clear liquids—this method can cause pump depolarization, leading to bleed-through that could introduce significant artifacts, making it unsuitable for imaging applications.

An alternative solution was proposed by Smith et al. [87], involving a single-pulse CARS technique. This method uses low-pass filtering of the pump in conjunction with a complementary dichroic filter, which focuses on the spectral shift of the anti-Stokes scattered field and probe interferences. This could potentially offer a more effective approach to managing the limitations of the current setup for excitation.

5.2.2 Detection range

In Chapter 2, we explored how the use of fast delay lines limits detection bandwidth due to the Nyquist theorem, which imposes constraints based on the smallest time step sampled. A higher scaling factor results in a lower detection limit. The most straightforward solution is to employ a mechanical delay line, but this significantly slows down data acquisition and prevents real-time imaging. Although the Agile Delay Line (ADL) is slower, it isn't bound by these limitations. However, it was designed for a narrow excitation bandwidth of 10 nm, making it unsuitable for applications requiring higher bandwidth.

To address the scaling factor (α) issue, one approach is to integrate two Dazzlers and control the relative delay between them. By leveraging the different scaling factors of High Resolution (HR) and Wide Band (WB) Dazzlers in separate arms, we can achieve an effective scaling factor of approximately 100 fs/μs (Fig. 5.2). This extends the detection range for an integration time of LIA $\tau_c = 100\ ns$ up to :

$$\Delta f = \frac{1}{2\alpha\tau_c} = 1668 cm^{-1} \tag{5.1}$$

However, this approach comes with a trade-off : a reduced scan window of about 3 ps, which limits the spectral resolution achievable in a single scan. This would be comparable to the spectral resolution we get on the low bandwidth excitation setup in Chapter 3. Therefore, employing a mechanical delay line to explore different scan windows would further slow down the imaging process. Yet, it's noteworthy that

using a Dazzler in both arms allows us to control higher-order dispersion effects. The Dazzler's ability to generate duplicate pulses enables coherent control over both the pump and probe arms simultaneously. This capability opens up new possibilities for fine-tuning and optimizing the spectral and temporal characteristics of the excitation pulses in our setup. Coherent control of the probe pulse has been shown in Shivkumar et.al.[71]

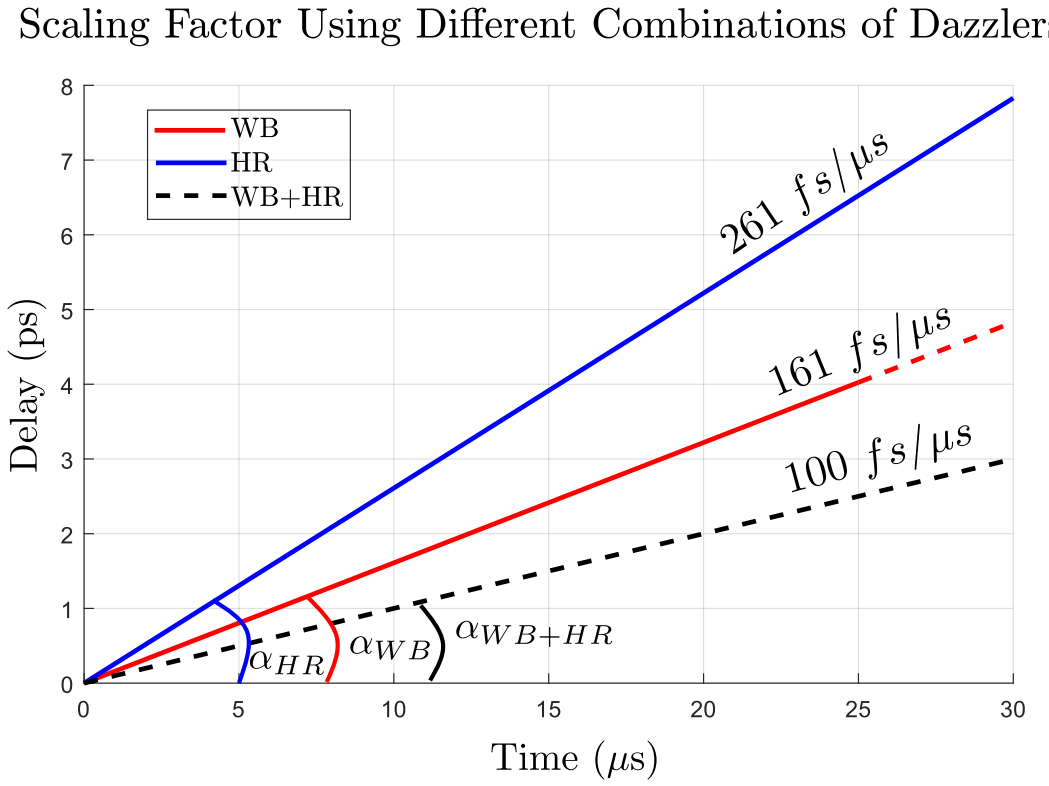

FIGURE 5.2 : The graph illustrates the scaling factor for different combinations of dazzlers : The HR, WB and a combination of both. This factor determines the delay range achievable for each dazzler's refresh rate. The blue line shows the delay scanned within 30 μs using the HR Dazzler. The dotted red lines indicate the WB dazzler reaching its maximum delay capacity within 25 μs due to the acoustic wave finishing its sweep. The dotted black line represents a scenario where the HR and WB dazzlers are used on the probe and pump beams, respectively. This configuration results in an effective scaling factor of $100\frac{fs}{\mu s}$ and introduces a maximum delay of 3 ps

We have demonstrated the possibility of doing this by adding a WB dazzler into the pump arm, while the probe arm uses the HR dazzler, giving us a scan window of 3 ps with an effective scaling factor of $100\frac{\text{fs}}{\mu\text{s}}$. Additional electronics were necessary to synchronize the two dazzlers. This synchronization was crucial to ensure that both delay lines started their acoustic waves simultaneously so that the corresponding

pump and probe pulses were delayed at the same moment. This synchronization was achieved by triggering the dazzler RF generators with a division from the laser clock. Fig. 5.3 shows the spectra of the BGO calibration crystal with this setup.

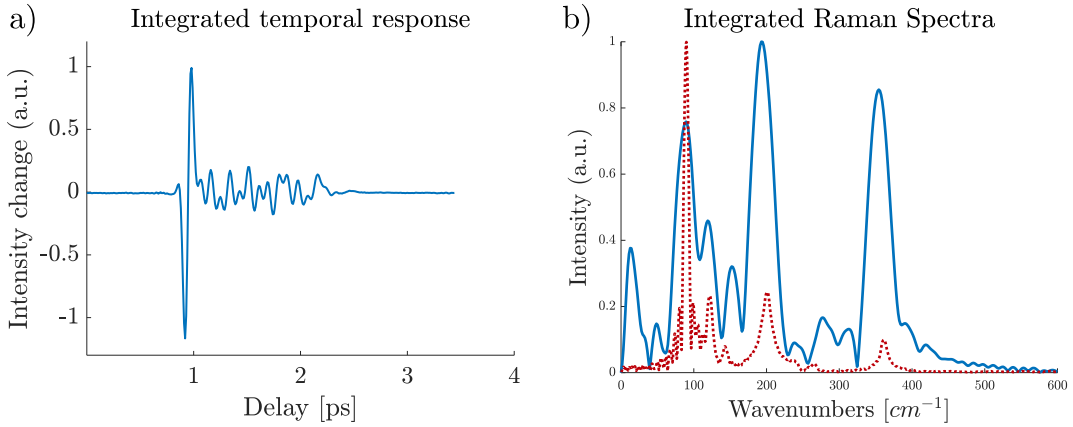

FIGURE 5.3 : a) Shows the time trace of 3 ps, which is scanned using a WB Dazzler in the pump arm and an HR Dazzler in the probe arm. b) The blue line represents the Raman spectra obtained by applying a Fourier transform to the time trace. Comparing this to the time trace acquired using only the HR dazzler in red, which can scan up to 8 ps, we observe a reduction in spectral resolution due to the shorter delay range scanned.

5.2.3 Sensitivity and SNR

The sensitivity of the setup determines its ability to detect low-intensity Raman signals and can be estimated using the Signal-to-Noise Ratio (SNR) or the fractional ratio of the signal into the lock-in amplifier. In our case, we use a lock-in amplifier with a maximum gain of 48 dB, beyond which we have post-amplification. The fractional modulation in the pump beam recorded by our LIA can be expressed using the formula from [88] :

$$\frac{\Delta I}{I} = \frac{Signal_{LIA}}{K \cdot P_{det}} \tag{5.2}$$

where ΔI is the modulation in the probe due to the signal, I is the total probe intensity, and $Signal_{LIA}$ is the output signal from the lock-in amplifier in millivolts. The constant $K = 5 \times 10^5 \, \frac{mV}{mW}$ is specific to the lock-in amplifier at maximum gain, and P_{det} represents the power incident on the detector plane. For the LIA we use, we find that the minimum fractional modulation we can detect is in the orders of 10^{-5} for an integration time of LIA 100 ns, and 10^{-6} for an integration time of 300 ns which is close to the shot noise limit.

5.3 Future perspectives

We have explored a range of samples, from calibration and pharmaceutical crystals to solvents, thanks to the extension of my detection setup, allowing for hyperspectral Raman imaging in the liquid phase. This advancement opens up exciting possibilities to investigate complex phase transitions and molecular interactions in both liquid and liquid crystal systems [89].

Another intriguing class of compounds under investigation is nanoplatelets, particularly those made from Cadmium Selenide. Nanoplatelets are ultra-thin materials, often just a few atomic layers thick, known for their unique optical and electronic properties due to their 2D structure, such as narrow emission spectra [90, 91], high absorption cross-sections, and rapid radiative decay rates.

There is significant interest in studying the structure of heterostructured nanocrystals to understand sharp interfaces and defects. Traditionally, very low-frequency acoustic phonons are characterized using Brillouin scattering. However, recent literature suggests the presence of low-frequency Raman vibrations attributed to ligands bonded with nanoplatelets [92, 93].

Recent research has also focused on introducing ligands into nanoplatelet structures and studying the resulting structural modifications, particularly in thin nanoplatelets comprising 3-4 monolayers [94]. Thiol-based ligands containing sulfur are commonly used in these studies. The structure of such a nanoplatelet is shown for the particular case of 4 monolayers (4-ML) with thiol ligands that have a carbon chain of length eight. The figure is courtesy of the ILM group in Lyon, who provided us with the samples.

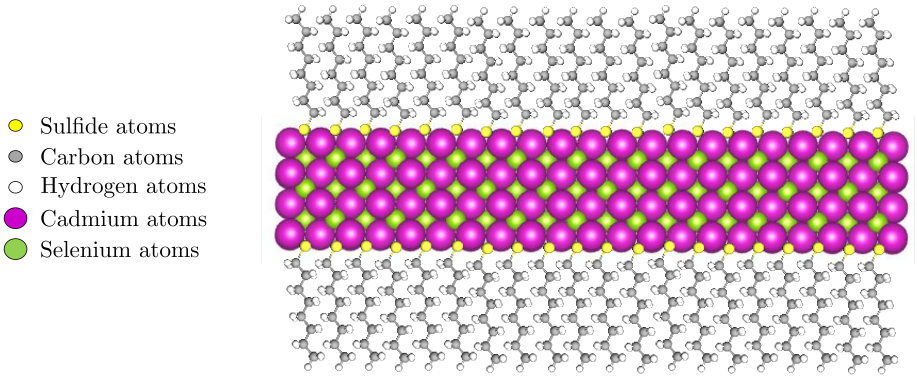

FIGURE 5.4 : The schematic above shows the structure of CdSe nanoplatelet with an eight-carbon change thiol ligand attached to it.

Using our setup, we have successfully imaged nanoplatelets functionalized with various ligands of different carbon chain lengths. An example of nanoplatelets functionalized with a 5-carbon chain is shown in Fig. 5.5. The aim is to determine whether we can distinguish between nanoplatelets with different carbon chain lengths and to

assess the limit of detection of our setup. This particular measurement was taken with 50 accumulations.

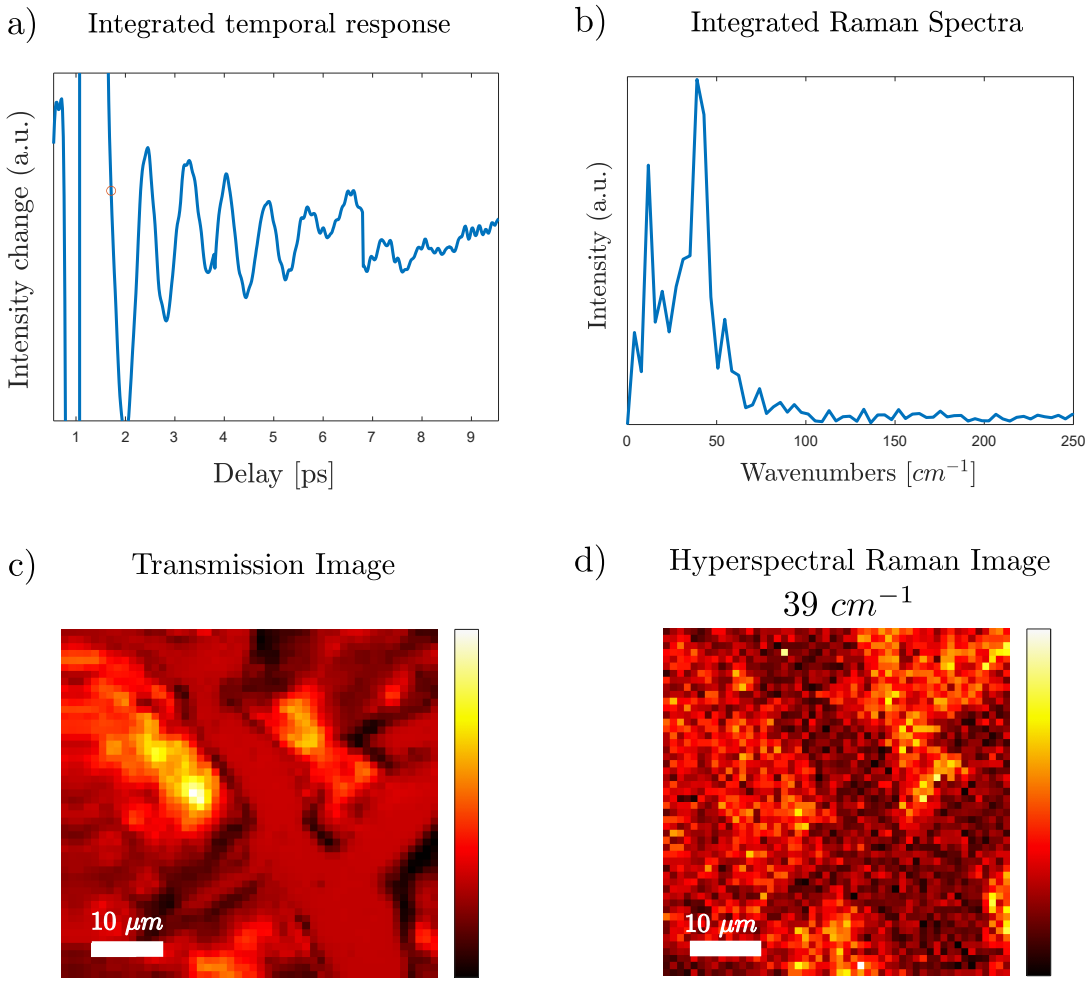

FIGURE 5.5 : The figures above show images of 3-monolayer CdSe NPLs that have a 5-carbon chain thiol ligand attached to it, captured with a field of view (FOV) of 50 μm at a resolution of 64 × 64 pixels. Fig. 5.5(a) presents the integrated spectra from the averaged time traces, while Fig. 5.5(b) displays the Fourier transform revealing the integrated Raman spectra. Fig. 5.5(c) includes the transmission image. The adjacent hyperspectral image highlights the strong vibrational mode at 39 cm^{-1} for the NPLs

This research is part of the EU-funded VIRUSONG project, where ongoing efforts aim to push the boundaries of nanoplatelet technology for advanced detection systems. The work is being continued by a PhD student, exploring the potential of these functionalized nanoplatelets, particularly for virus detection, which opens exciting new avenues in biosensing applications. This work holds promise for future breakthroughs in diagnostics, making use of the unique spectra of ligand bound nanocrystals.

Bibliographie

[1] J WANG, M SOWA, HH MANTSCH et al. « Comparison of different infrared measurement techniques in the clinical analysis of biofluids ». In : *TrAC Trends in Analytical Chemistry* 15.7 (1996), p. 286-296 (cf. p. 24).

[2] Donald C MALINS, Nayak L POLISSAR et Sandra J GUNSELMAN. « Infrared spectral models demonstrate that exposure to environmental chemicals leads to new forms of DNA ». In : *Proceedings of the National Academy of Sciences* 94.8 (1997), p. 3611-3615 (cf. p. 24).

[3] DC MALINS. « Methods for Determining Oxidative Injury to DNA Using IR Absorption Spectroscopy for Cancer Diagnosis ». In : *PCT Int. Appl* (1995) (cf. p. 24).

[4] Natalia I AFANASYEVA, Sergei F KOLYAKOV, Vjacheslav G ARTIOUSHENKO et al. « Minimally invasive and ex-vivo diagnostics of breast cancer tissues by fiber optic evanescent-wave fourier transform ir (few-ftir) spectroscopy ». In : *Optical Biopsy II*. T. 3250. SPIE. 1998, p. 140-147 (cf. p. 24).

[5] Lily M NG et Reiko SIMMONS. « Infrared spectroscopy ». In : *Analytical chemistry* 71.12 (1999), p. 343-350 (cf. p. 24).

[6] Eric Olaf POTMA et Shaul MUKAMEL. « Theory of coherent Raman scattering ». In : *Coherent Raman Scattering Microscopy* (2012), p. 3-42 (cf. p. 27).

[7] Robert W BOYD, Alexander L GAETA et Enno GIESE. « Nonlinear optics ». In : *Springer Handbook of Atomic, Molecular, and Optical Physics*. Springer, 2008, p. 1097-1110 (cf. p. 32).

[8] Yusuke OSHIMA, Hidetoshi SATO, Hiroko KAJIURA-KOBAYASHI et al. « Light sheet-excited spontaneous Raman imaging of a living fish by optical sectioning in a wide field Raman microscope ». In : *Optics Express* 20 (2012), p. 16195-16204. URL : https://api.semanticscholar.org/CorpusID:123200324 (cf. p. 33).

[9] Mitsugu OGAWA, Yoshinori HARADA, Yoshihisa YAMAOKA et al. « Label-free biochemical imaging of heart tissue with high-speed spontaneous Raman microscopy ». In : *Biochemical and biophysical research communications* 382.2 (2009), p. 370-374 (cf. p. 33).

[10] Theodore H MAIMAN et al. « Stimulated optical radiation in ruby ». In : (1960) (cf. p. 33).

[11] PD MAKER et RW TERHUNE. « Study of optical effects due to an induced polarization third order in the electric field strength ». In : *Physical Review* 137.3A (1965), A801 (cf. p. 33).

[12] Mamoru HASHIMOTO, Tsutomu ARAKI et Satoshi KAWATA. « Molecular vibration imaging in the fingerprint region by use of coherent anti-Stokes Raman scattering microscopy with a collinear configuration ». In : *Optics Letters* 25.24 (2000), p. 1768-1770 (cf. p. 33).

[13] MD DUNCAN, J REINTJES et TJ MANUCCIA. « Scanning coherent anti-Stokes Raman microscope ». In : *SPIE milestone series* 175 (2003), p. 89-91 (cf. p. 33).

[14] Andreas ZUMBUSCH, Gary R HOLTOM et X Sunney XIE. « Three-dimensional vibrational imaging by coherent anti-Stokes Raman scattering ». In : *Physical review letters* 82.20 (1999), p. 4142 (cf. p. 33).

[15] Dario POLLI, Vikas KUMAR, Carlo M VALENSISE et al. « Broadband coherent Raman scattering microscopy ». In : *Laser & Photonics Reviews* 12.9 (2018), p. 1800020 (cf. p. 33).

[16] Thomas HELLERER, Annika MK ENEJDER et Andreas ZUMBUSCH. « Spectral focusing : High spectral resolution spectroscopy with broad-bandwidth laser pulses ». In : *Applied Physics Letters* 85.1 (2004), p. 25-27 (cf. p. 33).

[17] Israel ROCHA-MENDOZA, Wolfgang LANGBEIN et Paola BORRI. « Coherent anti-Stokes Raman microspectroscopy using spectral focusing with glass dispersion ». In : *Applied Physics Letters* 93.20 (2008) (cf. p. 33).

[18] Adrian F PEGORARO, Andrew RIDSDALE, Douglas J MOFFATT et al. « Optimally chirped multimodal CARS microscopy based on a single Ti : sapphire oscillator ». In : *Optics express* 17.4 (2009), p. 2984-2996 (cf. p. 33).

[19] Michiel MÜLLER et Juleon M SCHINS. « Imaging the thermodynamic state of lipid membranes with multiplex CARS microscopy ». In : *The Journal of Physical Chemistry B* 106.14 (2002), p. 3715-3723 (cf. p. 33).

[20] Ji-xin CHENG, Andreas VOLKMER, Lewis D BOOK et al. « Multiplex coherent anti-Stokes Raman scattering microspectroscopy and study of lipid vesicles ». In : *The Journal of Physical Chemistry B* 106.34 (2002), p. 8493-8498 (cf. p. 33).

[21] Tak W KEE et Marcus T CICERONE. « Simple approach to one-laser, broadband coherent anti-Stokes Raman scattering microscopy ». In : *Optics letters* 29.23 (2004), p. 2701-2703 (cf. p. 33).

[22] Nirit DUDOVICH, Dan ORON et Yaron SILBERBERG. « Single-pulse coherently controlled nonlinear Raman spectroscopy and microscopy ». In : *Nature* 418.6897 (2002), p. 512-514 (cf. p. 33).

[23] Sukesh ROY, Paul WRZESINSKI, Dmitry PESTOV et al. « Single-beam coherent anti-Stokes Raman scattering spectroscopy of N 2 using a shaped 7 fs laser pulse ». In : *Applied Physics Letters* 95.7 (2009) (cf. p. 33).

[24] Andreas VOLKMER, Lewis D BOOK et X Sunney XIE. « Time-resolved coherent anti-Stokes Raman scattering microscopy : Imaging based on Raman free induction decay ». In : *Applied Physics Letters* 80.9 (2002), p. 1505-1507 (cf. p. 33).

[25] Romedi SELM, Martin WINTERHALDER, Andreas ZUMBUSCH et al. « Ultrabroadband background-free coherent anti-Stokes Raman scattering microscopy based on a compact Er : fiber laser system ». In : *Optics letters* 35.19 (2010), p. 3282-3284 (cf. p. 33).

[26] Denís PAREDES-ROIBÁS et Raúl Z MARTÍNEZ. « High-resolution stimulated Raman spectroscopy of low-frequency rotational transitions : Obtention of collisional broadening coefficients in the rotational S branch of CO perturbed by H2 ». In : *Journal of Raman Spectroscopy* 54.10 (2023), p. 1099-1113 (cf. p. 34).

[27] Francois M KAMGA et Mark G SCEATS. « Pulse-sequenced coherent anti-Stokes Raman scattering spectroscopy : a method for suppression of the nonresonant background ». In : *Optics Letters* 5.3 (1980), p. 126-128 (cf. p. 34).

[28] Keith A NELSON et Leah R WILLIAMS. « Femtosecond time-resolved observation of coherent molecular vibrational motion ». In : *Physical review letters* 58.7 (1987), p. 745 (cf. p. 34).

[29] Keith A NELSON, RJ Dwayne MILLER, DR LUTZ et al. « Optical generation of tunable ultrasonic waves ». In : *Journal of Applied Physics* 53.2 (1982), p. 1144-1149 (cf. p. 35).

[30] Margaret M ROBINSON, Yong-Xin YAN, Edward B GAMBLE JR et al. « Picosecond impulsive stimulated brillouin scattering : Optical excitation of coherent transverse acoustic waves and application to time-domain investigations of structural phase transitions ». In : *Chemical physics letters* 112.6 (1984), p. 491-496 (cf. p. 35).

[31] Richard C PRINCE, Renee R FRONTIERA et Eric O POTMA. « Stimulated Raman scattering : from bulk to nano ». In : *Chemical reviews* 117.7 (2017), p. 5070-5094 (cf. p. 35).

[32] Andrew M WEINER, DE LEAIRD, Gary P WIEDERRECHT et al. « Femtosecond multiple-pulse impulsive stimulated Raman scattering spectroscopy ». In : *JOSA B* 8.6 (1991), p. 1264-1275 (cf. p. 35).

[33] Jennifer P OGILVIE, Emmanuel BEAUREPAIRE, Antigoni ALEXANDROU et al. « Fourier-transform coherent anti-Stokes Raman scattering microscopy ». In : *Optics letters* 31.4 (2006), p. 480-482 (cf. p. 35).

[34] Kazuki HASHIMOTO, Megumi TAKAHASHI, Takuro IDEGUCHI et al. « Broadband coherent Raman spectroscopy running at 24,000 spectra per second ». In : *Scientific reports* 6.1 (2016), p. 21036 (cf. p. 36).

[35] Miu TAMAMITSU, Yusuke SAKAKI, Tasuku NAKAMURA et al. « Ultrafast broadband Fourier-transform CARS spectroscopy at 50,000 spectra/s enabled by a scanning Fourier-domain delay line ». In : *Vibrational Spectroscopy* 91 (2017), p. 163-169 (cf. p. 36).

[36] Fritz KEILMANN, Christoph GOHLE et Ronald HOLZWARTH. « Time-domain mid-infrared frequency-comb spectrometer ». In : *Optics letters* 29.13 (2004), p. 1542-1544 (cf. p. 36).

[37] Steven T CUNDIFF et Jun YE. « Colloquium : Femtosecond optical frequency combs ». In : *Reviews of Modern Physics* 75.1 (2003), p. 325 (cf. p. 36).

[38] Takuro IDEGUCHI, Simon HOLZNER, Birgitta BERNHARDT et al. « Coherent Raman spectro-imaging with laser frequency combs ». In : *Nature* 502.7471 (2013), p. 355-358 (cf. p. 36).

[39] Meng CUI, Manuel JOFFRE, Joshua SKODACK et al. « Interferometric Fourier transform coherent anti-Stokes Raman scattering ». In : *Optics Express* 14.18 (2006), p. 8448-8458 (cf. p. 36).

[40] AS DUARTE, C SCHNEDERMANN et P KUKURA. *Sci. Rep.* 2016 (cf. p. 36).

[41] S RUHMAN, AG JOLY, B KOHLER et al. « Intramolecular and intermolecular dynamics in molecular liquids through femtosecond time-resolved impulsive stimulated scattering ». In : *Revue de physique appliquée* 22.12 (1987), p. 1717-1734 (cf. p. 36).

[42] Sandro DE SILVESTRI, JG FUJIMOTO, EP IPPEN et al. « Femtosecond time-resolved measurements of optic phonon dephasing by impulsive stimulated raman scattering in α-perylene crystal from 20 to 300 K ». In : *Chemical physics letters* 116.2-3 (1985), p. 146-152 (cf. p. 36).

[43] Yong-Xin YAN, Edward B GAMBLE JR et Keith A NELSON. « Impulsive stimulated scattering : General importance in femtosecond laser pulse interactions with matter, and spectroscopic applications ». In : *The Journal of chemical physics* 83.11 (1985), p. 5391-5399 (cf. p. 36).

[44] Dekel RAANAN, Julian LÜTTIG, Yaron SILBERBERG et al. « Vibrational spectroscopy via stimulated Raman induced Kerr lensing ». In : *APL photonics* 3.9 (2018) (cf. p. 36).

[45] E GERSHGOREN, RA BARTELS, JT FOURKAS et al. « Simplified setup for high-resolution spectroscopy that uses ultrashort pulses ». In : *Optics letters* 28.5 (2003), p. 361-363 (cf. p. 36).

[46] Neil A SMITH et Stephen R MEECH. « Optically-heterodyne-detected optical Kerr effect (OHD-OKE) : applications in condensed phase dynamics ». In : *International Reviews in Physical Chemistry* 21.1 (2002), p. 75-100 (cf. p. 36).

[47] Jesse W WILSON, Philip SCHLUP et Randy A BARTELS. « Synthetic temporal aperture coherent molecular phase spectroscopy ». In : *Chemical Physics Letters* 463.4-6 (2008), p. 300-304 (cf. p. 36).

[48] Jesse W WILSON, Philip SCHLUP et Randy BARTELS. « Phase measurement of coherent Raman vibrational spectroscopy with chirped spectral holography ». In : *Optics letters* 33.18 (2008), p. 2116-2118 (cf. p. 36).

[49] Jared K WAHLSTRAND, Roberto MERLIN, Xiaoqin LI et al. « Impulsive stimulated Raman scattering : comparison between phase-sensitive and spectrally filtered techniques ». In : *Optics letters* 30.8 (2005), p. 926-928 (cf. p. 36).

[50] SR DOMINGUE, DG WINTERS et RA BARTELS. « Time-resolved coherent Raman spectroscopy by high-speed pump-probe delay scanning ». In : *Optics letters* 39.14 (2014), p. 4124-4127 (cf. p. 36).

[51] Yahel SOFFER, Dekel RAANAN et Dan ORON. « Low Frequency Collinear Pre-Resonant Impulsive Stimulated Raman Microspectroscopy ». In : *ACS Photonics* 7.12 (2020), p. 3481-3488 (cf. p. 36).

[52] Randy A BARTELS, Dan ORON et Hervé RIGNEAULT. « Low frequency coherent Raman spectroscopy ». In : *Journal of Physics : Photonics* 3.4 (2021), p. 042004 (cf. p. 38).

[53] John C POLANYI et Ahmed H ZEWAIL. « Direct observation of the transition state ». In : *Accounts of Chemical Research* 28.3 (1995), p. 119-132 (cf. p. 47).

[54] Ahmed H ZEWAIL. « Femtochemistry : Atomic-scale dynamics of the chemical bond ». In : *The Journal of Physical Chemistry A* 104.24 (2000), p. 5660-5694 (cf. p. 47).

[55] David A. SUMBERG. « Variable photonic delay line using electro-optic beam deflection ». In : *Defense, Security, and Sensing*. 1994. URL : https://api.semanticscholar.org/CorpusID:108637169 (cf. p. 47).

[56] Sarah SAINT-JALM, Esben Ravn ANDRESEN, Abdelkrim BENDAHMANE et al. « Nonlinear femtosecond pump-probe spectroscopy using a power-encoded soliton delay line. » In : *Optics letters* 41 1 (2016), p. 115-8. URL : https://api.semanticscholar.org/CorpusID:1412649 (cf. p. 47).

[57] Michael CHINI, Hiroki MASHIKO, He WANG et al. « Delay control in attosecond pump-probe experiments. » In : *Optics express* 17 24 (2009), p. 21459-64. URL : https://api.semanticscholar.org/CorpusID:8751452 (cf. p. 47).

[58] CD CRUZ, John C STEPHENSON, Sebastian ENGMANN et al. « Pump-probe phase spectroscopy with submilliradian sensitivity and nanosecond time delay using Michelson interferometers ». In : *Optics Express* 31.9 (2023), p. 14299-14307 (cf. p. 47).

[59] Marc M. WEFERS et Keith A. NELSON. « Programmable phase and amplitude femtosecond pulse shaping. » In : *Optics letters* 18 23 (1993), p. 2032. URL : https://api.semanticscholar.org/CorpusID:9915617 (cf. p. 47).

[60] Eugene FRUMKER et Yaron R. SILBERBERG. « Femtosecond pulse shaping using a two-dimensional liquid-crystal spatial light modulator. » In : *Optics letters* 32 11 (2007), p. 1384-6. URL : https://api.semanticscholar.org/CorpusID:36737580 (cf. p. 47).

[61] Bangshan SUN, Patrick S. SALTER et Martin J. BOOTH. « Pulse front adaptive optics : a new method for control of ultrashort laser pulses. » In : *Optics express* 23 15 (2015), p. 19348-57. URL : https://api.semanticscholar.org/CorpusID:18279126 (cf. p. 47).

[62] Stefano BONORA, Daniele BRIDA, Paolo VILLORESI et al. « Ultrabroadband pulse shaping with a push-pull deformable mirror. » In : *Optics express* 18 22 (2010), p. 23147-52. URL : https://api.semanticscholar.org/CorpusID:207316708 (cf. p. 47).

[63] Andrea CARTELLA, Stefano BONORA, M. FÖRST et al. « Pulse shaping in the mid-infrared by a deformable mirror. » In : *Optics letters* 39 6 (2014), p. 1485-8. URL : https://api.semanticscholar.org/CorpusID:37529263 (cf. p. 47).

[64] Andrew Marc WEINER. « Femtosecond optical pulse shaping and processing ». In : *Progress in Quantum Electronics* 19.3 (1995), p. 161-237 (cf. p. 47).

[65] Pierre TOURNOIS. « Acousto-optic programmable dispersive filter for adaptive compensation of group delay time dispersion in laser systems ». In : *Optics communications* 140.4-6 (1997), p. 245-249 (cf. p. 48).

[66] Frederic VERLUISE, Vincent LAUDE, Z CHENG et al. « Amplitude and phase control of ultrashort pulses by use of an acousto-optic programmable dispersive filter : pulse compression and shaping ». In : *Optics letters* 25.8 (2000), p. 575-577 (cf. p. 48).

[67] József SERES, Alexander MÜLLER, Enikö SERES et al. « Sub-10-fs, terawatt-scale Ti : sapphire laser system ». In : *Optics letters* 28.19 (2003), p. 1832-1834 (cf. p. 48).

[68] Amnon YARIV et Pochi YEH. « Optical waves in crystal propagation and control of laser radiation ». In : (1983) (cf. p. 49).

[69] Weiguo YANG, Dorine KEUSTERS, Debabrata GOSWAMI et al. « Rapid ultrafine-tunable optical delay line at the 1.55-μm wavelength ». In : *Optics letters* 23.23 (1998), p. 1843-1845 (cf. p. 55, 57, 60).

[70] Cl FROEHLY, B COLOMBEAU et M VAMPOUILLE. « II shaping and analysis of picosecond light pulses ». In : *Progress in optics*. T. 20. Elsevier, 1983, p. 63-153 (cf. p. 56).

[71] Siddarth SHIVKUMAR, Dekel RANANN, Samuel METAIS et al. « Selective detection in impulsive low-frequency Raman imaging using shaped probe pulses ». In : *Physical Review Applied* 19.5 (2023), p. 054075 (cf. p. 63, 105).

[72] *ScanImage®*. en-US. https://www.mbfbioscience.com/products/scanimage/. accessed : 2024-02-01. URL : https://www.mbfbioscience.com/products/scanimage/ (visité le 01/02/2024) (cf. p. 65).

[73] Muzaffer MOHAMMED, Maleeha F SYED, Mona J BHATT et al. « Rapid and selective crystallization of acetaminophen using metal-assisted and microwave-accelerated evaporative crystallization ». In : *Nano biomedicine and engineering* 4.1 (2012), p. 35 (cf. p. 73).

[74] Richard G. BARANIUK. « Compressive Sensing [Lecture Notes] ». In : *IEEE Signal Processing Magazine* 24.4 (2007), p. 118-121. DOI : 10.1109/MSP.2007.4286571 (cf. p. 83).

[75] Luca BOLZONELLO, Niek F. van HULST et Andreas JAKOBSSON. « Fisher information for smart sampling in time-domain spectroscopy ». In : *The Journal of Chemical Physics* 160.21 (juin 2024), p. 214110. ISSN : 0021-9606. DOI : 10.1063/5.0206838. eprint : https://pubs.aip.org/aip/jcp/article-pdf/doi/10.1063/5.0206838/19972190/214110_1_5.0206838.pdf. URL : https://doi.org/10.1063/5.0206838 (cf. p. 83).

[76] T Toney FERNANDEZ, Karen PRIVAT, Michael J WITHFORD et al. « Record-high positive refractive index change in bismuth germanate crystals through ultrafast laser enhanced polarizability ». In : *Scientific Reports* 10.1 (2020), p. 15142 (cf. p. 94).

[77] Ningning DONG, Daniel JAQUE, Feng CHEN et al. « Second harmonic and Raman imaging of He+ implanted KTiOPO 4 waveguides ». In : *Optics Express* 19.15 (2011), p. 13934-13939 (cf. p. 94).

[78] Zhang XIA, Yin SHAO-TANG, Wan SONG-MING et al. « Raman Spectrum Analysis on the Solid–Liquid Boundary Layer ofBGO Crystal Growth ». In : *Chinese Physics Letters* 24.7 (2007), p. 1898 (cf. p. 94).

[79] Chi-Shun TU, AR GUO, Ruiwu TAO et al. « Temperature dependent Raman scattering in KTiOPO4 and KTiOAsO4 single crystals ». In : *Journal of applied physics* 79.6 (1996), p. 3235-3240 (cf. p. 94).

[80] M SAVOLAINEN, Karin KOGERMANN, A HEINZ et al. « Better understanding of dissolution behaviour of amorphous drugs by in situ solid-state analysis using Raman spectroscopy ». In : *European journal of pharmaceutics and biopharmaceutics* 71.1 (2009), p. 71-79 (cf. p. 96).

[81] Leonardo M MOREIRA, Landulfo SILVEIRA JR, Fábio V SANTOS et al. « Raman spectroscopy : A powerful technique for biochemical analysis and diagnosis ». In : *Spectroscopy* 22.1 (2008), p. 1-19 (cf. p. 96).

[82] Salvatore ALMAVIVA, Florinda ARTUSO, Isabella GIARDINA et al. « Fast detection of different water contaminants by Raman spectroscopy and surface-enhanced Raman spectroscopy ». In : *Sensors* 22.21 (2022), p. 8338 (cf. p. 96).

[83] Guannan QU, Rasheed BILAL, Minsi XIN et al. « Phase transition-induced changes in the Raman properties of DMSO/benzene binary systems ». In : *Physical Chemistry Chemical Physics* 23.15 (2021), p. 9211-9217 (cf. p. 96).

[84] A SELVARAJAN. « Raman spectrum of dimethyl sulfoxide (DMSO) and the influence of solvents ». In : *Proceedings of the Indian Academy of Sciences-Section A*. T. 64. 1. Springer. 1966, p. 44-50 (cf. p. 96).

[85] Jeffrey J FIELD, Thomas A PLANCHON, Wafa AMIR et al. « Characterization of a high efficiency, ultrashort pulse shaper incorporating a reflective 4096-element spatial light modulator ». In : *Optics communications* 278.2 (2007), p. 368-376 (cf. p. 104).

[86] Daniel HAHNER, Philipp STEINLEITNER, Yu CHEN et al. « Second and third-order dispersion compensating mirror pairs for the spectral range from 1.2-3.2 μm ». In : *Optics Express* 30.21 (2022), p. 38709-38716 (cf. p. 104).

[87] David R SMITH, Siddarth SHIVKUMAR, Jeff FIELD et al. « Nearly degenerate two-color impulsive coherent Raman hyperspectral imaging ». In : *Optics Letters* 47.22 (2022), p. 5841-5844 (cf. p. 104).

[88] Alberto LOMBARDINI, Esben Ravn ANDRESEN, Alexandre KUDLINSKI et al. « Origin and suppression of parasitic signals in Kagomé lattice hollow core fibers used for SRS microscopy and endoscopy ». In : *Optics Letters* 42.9 (2017), p. 1824-1827 (cf. p. 106).

[89] WJ BORER, SS MITRA et CW BROWN. « Crystal to liquid-crystal transition studied by Raman scattering ». In : *Physical Review Letters* 27.7 (1971), p. 379 (cf. p. 107).

[90] Zhuoying CHEN, Brice NADAL, Benoit MAHLER et al. « Quasi-2D colloidal semiconductor nanoplatelets for narrow electroluminescence ». In : *Advanced Functional Materials* 24.3 (2014), p. 295-302 (cf. p. 107).

[91] Fengjia FAN, Pongsakorn KANJANABOOS, Mayuran SARAVANAPAVANANTHAM et al. « Colloidal CdSe1–x S x Nanoplatelets with Narrow and Continuously-Tunable Electroluminescence ». In : *Nano letters* 15.7 (2015), p. 4611-4615 (cf. p. 107).

[92] A Jolene MORK, Elizabeth MY LEE, Nabeel S DAHOD et al. « Modulation of low-frequency acoustic vibrations in semiconductor nanocrystals through choice of surface ligand ». In : *The journal of physical chemistry letters* 7.20 (2016), p. 4213-4216 (cf. p. 107).

[93] Adrien GIRARD, Lucien SAVIOT, Silvia PEDETTI et al. « The mass load effect on the resonant acoustic frequencies of colloidal semiconductor nanoplatelets ». In : *Nanoscale* 8.27 (2016), p. 13251-13256 (cf. p. 107).

[94] Quentin MARTINET, Justine BARONNIER, Adrien GIRARD et al. « Ligand-dependent nano-mechanical properties of CdSe nanoplatelets : calibrating nanobalances for ligand affinity monitoring ». In : *Nanoscale* 13.18 (2021), p. 8639-8647 (cf. p. 107).